Universidad de Concepción
Dirección de Postgrado
Facultad de Ciencias Físicas y Matemáticas
Programa de Magíster en Ciencias con mención en Físicas

ESTUDIO DEL CICLO LARGO EN LAS VARIABLES DE DOBLE PERIODO

(LONG CYCLE STUDY OF THE DOUBLE PERIODIC VARIABLES)

Tesis para optar al grado académico de Magíster en Ciencias con mención en Física

Juan Isaías Garcés Letelier
Concepción - Chile
Septiembre 2019

Profesor Guía: Dr. Ronald Mennickent
Departamento de Astronomía
Facultad de Ciencias Físicas y Matemáticas
Universidad de Concepción

Agradecimientos

Quisiera agradecer a los miembro del grupo stellar variability group (SVG) por ayudar a mejor las primeras versiones de este trabajo. Este grupo es liderado por el Dr. Ronald Mennickent, quien además es profesor guía de esta tesis. A él quisiera agradecer su ayuda, motivación, confianza y total apoyo para llevar a cabo este trabajo. Agradezco también a quienes fueron parte importante en los resultados de esta tesis. Al Dr. Djuraševic, por realizar los modelos aplicados a las curvas de luz y los integrantes del grupo OGLE, Dr. Poleski y Dr. Soszyński, por facilitarnos gentilmente parte de los datos fotométricos usados en este estudio. De igual forma, reconocer el apoyo brindado por los miembros de la comisión de esta tesis Dr. Nicola Atudillo-Defru, Dr. Domik Schelicher, Dr. Sandro Villanova.

También, quisiera agradecer a mi familia, en especial a mi madre y padre, por su constante apoyo en todo ámbito de la vida. Por último, agradecer a todas aquellas personas con la que he compartido durante este proceso.

Parte de este estudio se realizó con el financiamiento de los proyectos VRID-Enlace 216.016.002-1.0 y BASAL Centro de astrofísica y tecnologías Afines (CATA) PFB-06/2007. Algunos de los resultados de esta tesis fueron presentados en congreso “Observing techniques, instrumentation and science for metre-class telescopes II ”gracias al financiamiento de Dirección de postgrado de la Universidad de Concepción.

Resumen

Las variables de doble periodo (DPV) son sistemas binarios interactuantes que muestran un ciclo largo cuya duración es ~ 33 veces el periodo orbital P_o. Se componen de una estrella gigante que ha llenado su lóbulo de roche (donante) y que se encuentra transfiriendo masa a una estrella caliente de tipo espectral B (ganadora) rodeada de un disco de acreción óptica y geométricamente grueso. Si bien, a la fecha se desconoce el origen del ciclo largo, la posible actividad magnética de la estrella donante pareciera ser la explicación más probable Schleicher & Mennickent (2017).

Comenzamos este estudio mostrando un análisis fotométrico de dos DPVs que muestran cambios evidentes de morfología durante de las etapas ascendente, máxima, descendente y mínima del ciclo largo. Los modelos teóricos aplicados a las diferentes curvas de luz indican que se deben principalmente a cambios físicos del disco de acreción y las zonas activas en él. Con un modelo similar, logramos incluso explicar los cambios de profundidad observados en la curva de luz orbital de la binaria OGLE-BLG-ECL-253799. También, analizamos 142 DPVs en la nube grande y chica de magallanes. Encontramos 11 objetos, con claros cambios de profundidad en los mínimos primarios y secundarios relacionados con el ciclo largo. La mayoría de ellos muestra un patrón evidente: el mínimo secundario es más profundo durante el máximo del ciclo largo. Examinamos los residuales de la curva de luz de estos objetos y encontramos combinaciones de frecuencias en 10 casos. Además encontramos 25 objetos con variaciones de periodo largo. Esto nos permitió construir curvas de luz de ciclo largo con menor dispersión, además de eliminar frecuencias adicionales encontradas en estudios previos. Por último, cuantificamos la dispersión del ciclo largo y notamos que los sistemas DPVs con una menor inclinación del plano (elipsoidales) muestran una dispersión mucho menor que los sistemas con mayor inclinación (eclipsantes).

Nuestros resultados aportan conocimientos valiosos respecto al fenómeno DPVs. Un resultado importante es el cambio drástico en la estructura del disco de acreción de los objetos que presentamos, ya que se podrían deber a tasas de transferencia de masas cíclicas, lo que iría en acuerdo con las predicciones del dínamo magnético en DPVs (Schleicher & Mennickent, 2017).

Abstract

The double periodic variables (DPV) are interacting binary systems that show a long cycle with a duration of ~ 33 times the orbital period P_o. They consist of a giant star that has filled its roche lobe (donor) which transfers mass to a hot B spectral type star (gainer) surrounded by an optical and geometrically thick accretion disc. Although to date the origin of the long cycle is unknown, the possible magnetic activity of the donor star seems to be the most probable explanation Schleicher & Mennickent (2017).

We begin this study showing a photometric analysis of two DPVs that exhibit clear morphology changes during the ascending, maximum, descending and minimum stages of the long cycle. The theoretical models applied to the different light curves indicate that they are due to physical changes of the accretion disc and active areas in it. With a similar model, we even managed to explain the depth changes observed in the light curve of the OGLE-BLG-ECL-253799 binary. We also analyzed 142 DPVs in the large and small Magellanic Clouds. We found 11 objects with clear depth changes in the primary and secondary minima related to the long cycle. Most of them show an evident pattern: the secondary minimum is deeper during the maximum of the long cycle. We examined the residuals of the light curve of these objects and found combinations of frequencies in 10 cases. We also found 25 objects with long cycle variations. This allowed us to build long cycle light curves with less dispersion as well as eliminate additional frequencies found in previous studies. Lastly, we quantified the dispersion of the long cycle and noticed that DPVs systems with a lower inclination of the plane (ellipsoidals) exhibit a much less dispersion compared to systems with higher inclination (eclipsing).

Our results provide valuable knowledge to the DPVs phenomenon. An important result is the drastic change in the structure of the accretion disc of the objects we presented, since they could be due to cyclical mass transfer rates, which would be in accordance to the prediction of the magnetic dynamo in DPVs Schleicher & Mennickent (2017).

Contents

List of Tables

List of Figures

1

Introduction to Binary Systems

The vast majority of the stars we observe from Earth are gravitationally linked to others in binary (or multiple) systems. This concept was first introduced by astronomer Herschel (during the year 1802), indicating that in a binary system the stars would move in opposite directions and parallel to each other, as long as no external force acts. Because of this, binary systems have become a truly unique tool in understanding the universe, as well as in estimating distances within it. Specifically, by analyzing the light curve and radial velocities, we can accurately estimate fundamental parameters such as mass, radius, temperature and luminosity of its components. This has been fundamental to restrict evolutionary theoretical models for stars with different mass in the main sequence since virtually all empirical determinations of stellar masses have been made by studying nearby binary stars (Andersen, 1991). In addition, if the temperature of the components are accurately obtained, their absolute luminosities and therefore their distances can be estimated directly. In this sense, the brightness-color relation can also be used to estimate angular diameters of stars in late-type binary systems, and thus calculate distances with great precision, even at nearby galaxies (Pietrzyński et al., 2013).

In recent decades, a variety of variable star surveys have been made. In the Magellanic Clouds several binary systems have been detected through the MACHO project (e.g. Alcock et al., 1997; Derekas et al., 2007) and the EROS project (e. g. Muraveva et al., 2014; Kim et al., 2014). One of the most complete surveys has been the one developed by the OGLE project, which has detected 48.605 binary systems, of which 40.204 belong to the Large Magellanic Cloud (LMC), while 8.401 to the Small Magellanic Cloud (SMC) (Pawlak et al., 2016). In addition, considering only

the observations of the OGLE database in our galaxy, 450.000 were identified by Soszyński et al. (2016), increasing by two order of magnitudes the systems discovered to date in the galactic bulge.

It is estimated that about 70% of massive stars are exchanging mass (Sana et al., 2012) and about 30% of stars in the main sequence are the product of binary interaction (de Mink et al., 2014). For this reason, understanding the different evolutionary paths of stars in binary systems means to understand much of the observable universe. Below we describe some basic concepts in the study of close binary systems.

1.1 Close binary systems

The components of a binary system are classified as primary and secondary stars. Generally, the primary star is the most massive (and hottest) and the secondary is the less massive (and coldest). Considering this classification the mass ratio of the system $q = M_2/M_1$ will range from 0 to 1. If we assume a circular orbit, we can use Kepler's third law to relate the distance between the components a, orbital period P_o and mass of both stars by the following equation (Hilditch, 2001):

$$G(M_1 + M_2) = 4\pi^2 a^3 / P_o^2 \tag{1.1}$$

Where G is the universal gravitation constant. This equation is really useful considering that parameters such as the orbital period and a can be determined observationally.

Regarding the binary system orbit, the main elements that define its size, shape and orientation in a three-dimensional space are the following. Semi major axis a and eccentricity of the orbit e. Ascending node, which corresponds to the intersection of the projection of the orbital plane with the tangent of the sky plane. Inclination of the orbital plane i, which will be measured with respect to the plane of projection of the sky, so that a value of $i = 90°$ indicates that the line of sight of the observer coincides with the orbital plane. Longitude of periastron ω, which corresponds to the orientation of the orbit on its same plane. Angle of the ascending node Ω, which indicates the orientation of the node line. And finally, the time of passage at the periastron T (see Fig. 1.1).

Observing and analyzing a binary system will depend on the elements of the orbit, as well as the physical characteristics of the components. In this sense, in general, we can classify binary systems according to the observational characteristics, between resolved (or visual), spectroscopic

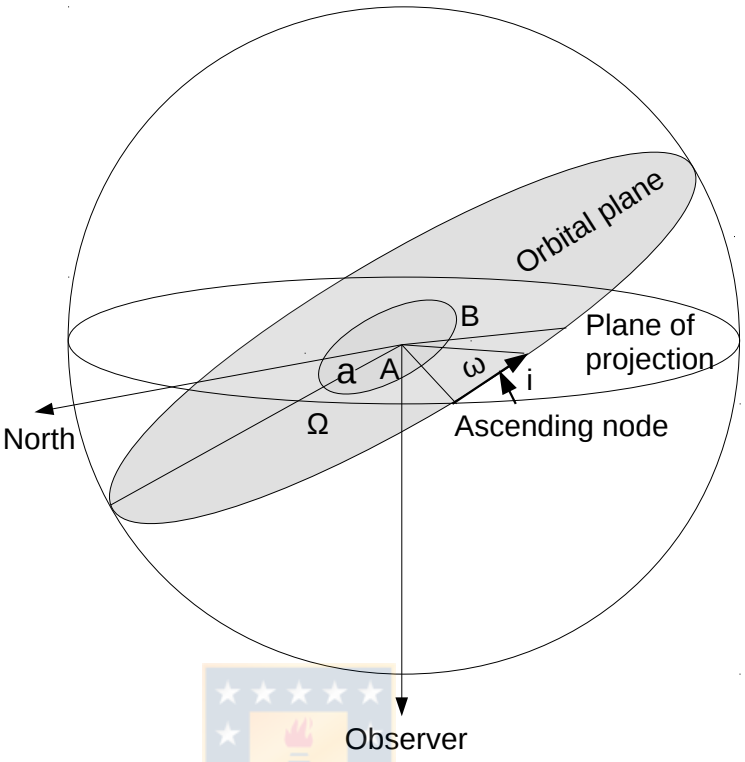

Figure 1.1 Illustrative view of the most important elements of orbits (a, e, i, ω, Ω), described in the text. A and B correspond to the orbital and projection plane, respectively.

and photometric binaries.

Visual binaries: correspond to those systems in which the components can be solved directly and their apparent movement around the center of mass can be estimated. They were the first binary systems that could be observed with small telescopes. By observing the relative orbit of these objects, parameters such as the orbital period can be calculated. In addition, if the distance to the system and the angular separation are known, the distance of semi major axis can easily be estimated.

Spectroscopic binaries: some binary systems become evident when observing their spectra at different times of observation. Due to the orbital movement of the components, we will observe a shift in the spectral lines due to the Doppler effect, given by the following equation (Hilditch,

2001).

$$v_{rad} = c\left(\frac{\lambda - \lambda_o}{\lambda_o}\right) \tag{1.2}$$

Where λ is the wavelength where an emission/absorption occurs at rest, λ_o is the wavelength at which it is observed and c is the speed of light in vacuum. We will observe a blueshift in the lines of the electromagnetic spectrum, coming from a source moving towards the observer. While we will observe a redshift of the component that moves away. The spectra can have lines of both components (SB2) or only of the brightest one (SB1). By means of spectroscopy, the projected radial velocity of the stars in a binary system (SB2) can be obtained reliably and thus the semi amplitude of the radial velocity, which is useful when estimating the spectroscopic mass ratio of the system.

Photometric binaries: correspond to stars that show changes in brightness due to extrinsic factors, such as the total or partial eclipse produced by one of the components. This will depend mainly on the size of the stars, in addition to the inclination of the orbital plane. We will observe that periodic changes in brightness occur (if the orbital period is constant), producing a primary minimum when the brightest component is eclipsed by the less brightest. In the opposite case, a secondary minimum will occur. Due to the large amount of photometric data available in time for many of the objects classified as eclipsing binaries, their orbital period has been determined (See Chapter 2), which has allowed the construction of their light curves. According to their morphology, different classifications have been adopted. We can distinguish three types clearly:

EA: variable Algol type. They have similar light curves to the Algol system, with well defined primary and secondary eclipses. Outside the eclipses there are practically no variations of light.
EB: variable type β-Lyr. Systems with curves similar to the β-Lyr system. They also have well defined primary and secondary minima, but there are variations of light outside the eclipses due to the non spherical morphology of their components.
EW: variable type W UMa. Systems with curves similar to the W UMa system. The brightness changes constantly and there is no major difference between the depth of both minimums.

This classification is only restricted to the morphology of the light curve, so a system classified

as EA does not imply that it has the same evolutionary characteristics as the Algol system. The same goes for a system cataloged as EB and EW (for more details see Hilditch, 2001).

1.2 The Roche Lobe model

Stars in close binary systems tend to circularize and synchronize their orbits due to tidal lockage, which causes two stellar hemispheres to face each other, and two are permanently avoided. As a consequence of the synchronization, the orbital period will be equal to the stellar rotation periods of both components. To better understand the morphology of stars in close binary systems, it is important to analyze the total gravitational potential of the system. This is how we arrive at the Roche model, in honor of the French mathematician Edouard Roche, who studied the mathematics of the restricted three-body problem, considering two point masses that move in circular orbits over their center of mass in common. For this reason, we can apply the Roche model to stars that have circularized and synchronized their orbits, and thus estimate the equipotential surfaces around the system components.

We assume that the origin of the system $(0, 0, 0)$ is at the center of mass of the primary star M_1 (more massive), which rotates with a constant angular velocity ω, and that the center of mass of the secondary star $(1, 0, 0)$ is at a distance $a = 1$ of the system origin (See Fig. 1.2). We can describe the total potential (Ψ) that the masses exert on a point $P(x, y, z)$, as the sum of the gravitational potentials for both masses and a rotational potential (Hilditch, 2001):

$$\Psi = -\frac{GM_1}{r_1} - \frac{GM_2}{r_2} - \frac{\omega^2}{2}\left[\left(x - \frac{M_2}{(M_1 + M_2)}\right)^2 + y^2\right] \tag{1.3}$$

where $r_1 = (x^2 + y^2 + z^2)^{1/2}$, and $r_2 = [(x - 1)^2 + y^2 + z^2]^{1/2}$.

As we assume synchronization and circularization of the orbit, in addition to a normalized distance between components ($a = 1$), we can write the Eq. 1.1 as follows (Hilditch, 2001): $\omega^2 = (2\pi/P_o)^2 = G(m_1 + m_2)/a^3 = G(m_1 + m_2)$. We can get the normalized version of the potential by defining $\Psi_n = -2\Psi/G(M_1 + M_2)$ and the mass ratio $q = M_2/M_1$ $(0 < q \leq 1)$, we have (Hilditch, 2001):

$$\Psi_n = \frac{2}{(1 + q)r_1} + \frac{2q}{(1 + q)r_2} + \left(x - \frac{q}{(1 + q)}\right)^2 + y^2 \tag{1.4}$$

Fig. 1.2 shows a representation of the dimensionless potential for a q = 0.65. The equipotential

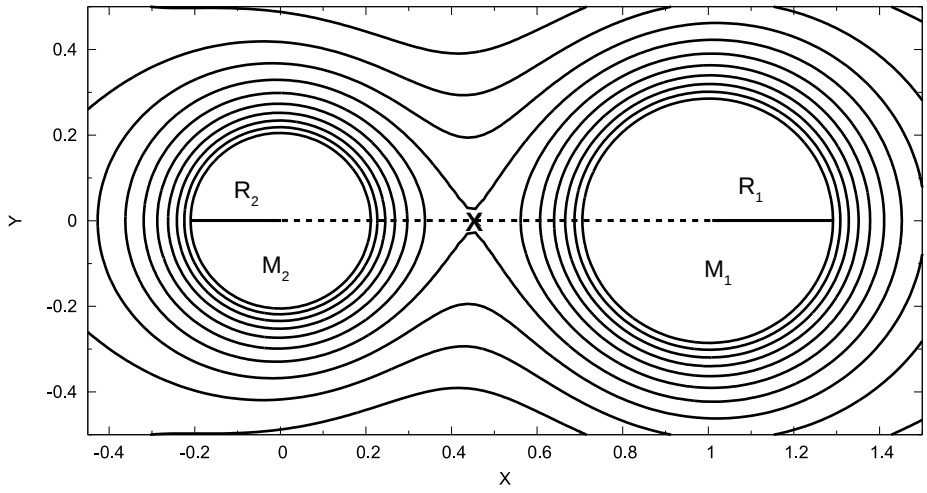

Figure 1.2 Representation of the equipotential surfaces of the dimensionless potential of Roche in the $x - y$ plane. The less massive star M_2 of radius R_2, was located at position $(0, 0, 0)$, while the most massive star M_1 of radius R_1 at $(1, 0, 0)$. The X represents the location of the internal Lagrangian point L_1.

surface that encompasses the two stars is called Roche lobe, and defines the maximum volumes that the stars of the binary system can occupy. If in a binary system a particle leaves the gravitational potential of the primary star through the internal lagrangian point L_1, it will fall towards the secondary star. Similarly, if a particle leaves the gravitational potential of the secondary star through point L_2, it will leave the gravitational field of the binary system with the proper escape velocity. This is how an important amount, with respect to the evolution of binary systems, is the effective radius of the Roche Lobe r_L. This radius is given by (Eggleton, 1983):

$$r_L = \frac{0.49q^{2/3}}{0.69q^{2/3} + ln(1 + q^{1/3})} \tag{1.5}$$

With an accurate to about $\pm 1\%$ for all values of q. Using Eq. 1.5 we can obtain the effective radius of the Roche lobe for the most massive ($r_{L,1}$) and less massive ($r_{L,2}$) component, using $q = M_1/M_2$ ($q \geq 1$) or $q = M_2/M_1$ ($q \leq 1$) respectively. A more complete description of the Roche model is described in Hilditch (2001).

Considering the Roche model, we can catalog the binary systems by their physical configuration, which will depend on the volume occupied by the stars in their lobe. In this sense, three

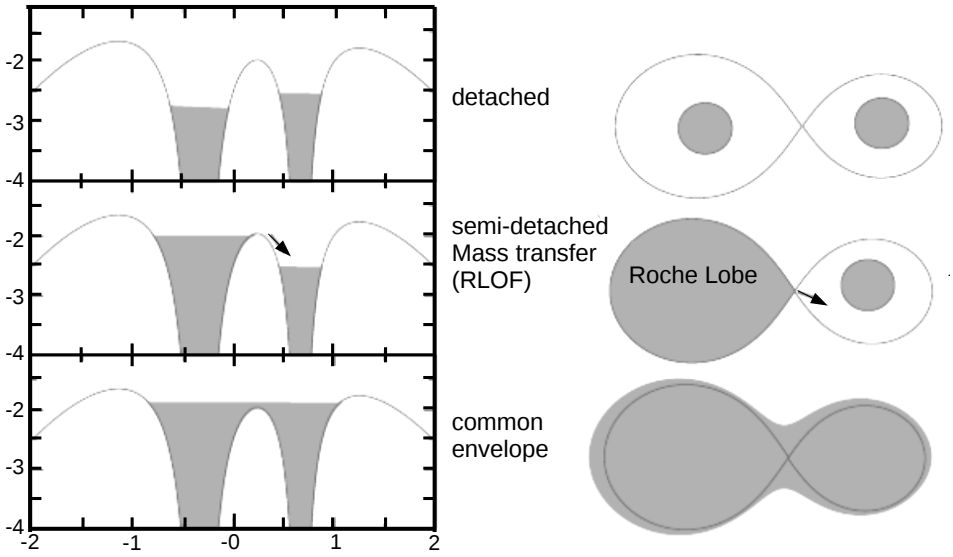

Figure 1.3 Different configurations of binary, detached, semi-detached with RLOF and common envelope are shown. In gray, a representation of the filling volume of the Roche Lobe seen from a cross section to the orbital plane (left) and seen from the orbital plane (right). Figure taken from (Habing & Olofsson, 2004).

types are also distinguished (See Fig. 1.3):

Detached systems: the stars are inside its lobe, without approaching the limit of this. Both components are separated from each other.

Semidetached systems: one of the stars has completely filled his lobe, while his companion is still confined to him.

Contact systems: both stars have filled their lobes, even in excess in some cases.

1.2.1 Roche Lobe Overflow

One of the mechanisms for mass transfer that occur in a binary system is the Roche lobe overflow (RLOF) of one of the components. The donor star will continue its overflow due to its own evolution, which will also depend on the effects that have on the distance between the components and the orbital period. By the end of the process, the donor's mass will have been reduced. For this it is necessary to understand the reaction time to those changes. There are three fundamental time

scales that dominate mass transfer in stellar evolution. These are the dynamical, thermal and nuclear time, which vary in duration and rates of mass loss. The **dynamical time scale** corresponds to what the star takes to react to deviations from the hydrostatic equilibrium. The mass transfer will be on a dynamical time scale, when the star can not readjust its hydrostatic equilibrium fast enough to counteract changes in the Roche lobe. Generally in these processes the mass loss rates range from 10^{-5} to 10^{-4} $M_{\odot}$ per year, in rapid events that can last from 10^{4} to 10^{5} years, which is a very short time compared to the stellar evolution scale. The **thermal time scale** measures the reaction to deviations from thermal equilibrium. Once the star has filled its Roche lobe, following a rapid adiabatic expansion, the mass transfer will occur on a thermal time scale, because the donor star will continue to expand beyond its Roche lobe to reach thermal equilibrium. For this process the mass transfer rates are from the order of 10^{-7} to 10^{-8} $M_{\odot}$ per year. At the **nuclear time scale** the loss of mass will only be by processes of stellar evolution. In this case the mass transfer will be due to the evolutionary expansion due to internal nuclear fusion processes of the donor star. It corresponds to the slowest time of mass transfer, with very low rates of the order of 10^{-11} to 10^{-8} $M_{\odot}$ per year (For more information see Hilditch, 2001).

On the other hand, donor stars may be in different evolutionary stages during the mass transfer process. For this there is a classification proposed by Kippenhahn & Weigert (1967) in the first instance. These general cases are the following:

Case A: The mass transfer occurs during the core burning-hydrogen stage, while the donor star still remains in the main sequence. This transfer will occur at a nuclear time scale, in a very long process that allows the donor star to adapt to the Roche lobe radio changes, without deviating from the thermal equilibrium.

Case B: Mass transfer occurs when the donor star is in the burning phase of the Hydrogen-shell. In this case, the transfer is on a shorter time scale than the previous one and will end when the donor's hydrogen envelope is exhausted.

Case C: In this case the mass transfer occurs after the exhaustion of He in the stellar core. For the donor star to reach this advanced evolutionary stage in a binary system, the initial orbital period must be greater than a hundred days.

During the different evolutionary paths that the components of a binary system can follow, two cases can occur with respect to the conservation of the initial mass of the system. The ideal case, and simpler, is when the initial mass is conserved, and the opposite case when there is loss of mass by different mechanisms. We will then theoretically cover both situations.

1.2.2 Conservative mass exchange

If the mass that loses one of the components is received completely by the other, we will say that the exchange of mass is conservative. If this is the case, the total angular momentum of the system will also be conserved. This is defined as the sum of the orbital angular momentum of the masses and the rotational angular momentum of the components. If we ignored the latter and assume a circular orbit (e = 0), we can write the angular momentum of the system as follows (Hilditch, 2001):

$$J_{orb} = \left[\frac{GM_1^2M_2^2}{M_{tot}}a\right]^{1/2} \tag{1.6}$$

Now, we can also write the period variation, considering $\dot{m}_1$ = -$\dot{m}_2$ for a conservative system (Hilditch, 2001). So:

$$\frac{\dot{P}}{P} = \frac{3\dot{M}_1(M_1 - M_2)}{M_1M_2} \tag{1.7}$$

Where P is the period after the mass exchange. We observe that $\dot{P}$ will depend directly on the variation of mass $\dot{M}_1$. If the more massive star M_1, transfers mass to the less massive star M_2, then $\dot{M}_1 < 0$ and the period will decrease ($\dot{P} < 0$), along with the size of the orbit a. On the other hand, if the star of mass M_1 continues to lose mass so that $M_1 < M_2$, then $\dot{P} > 0$, and both P and a will increase.

1.2.3 Non conservative mass exchange

We know that in reality there are different mechanisms that make mass transfer not conservative in an interactive binary system. The reasons may be several, such as the loss of mass by stellar wind, rapid Roche lobe overflows (RLOF) or violent mass loss as they occur in supernova events.

Now, if we consider that the donor star is losing mass $\dot{M}_1$, the gainer star is gaining mass at a

rate $\dot{M}_2$, so, the rest given by $\dot{M} = \dot{M}_1 + \dot{M}_2$ will be what the system is losing. Due to this loss of mass $\dot{M}$ is that the total angular momentum of the system will be lost, which corresponds to the sum of the orbital angular momentum lost by the donor and the one contributed by any other mechanism (K), described by the following equation (Hilditch, 2001):

$$\frac{\dot{J}}{J} = \frac{M_2}{M_1}\frac{\dot{M}}{(M_1 + M_2)} + K \tag{1.8}$$

Finally, the variation of the orbital period can be written as a function of the rate of transfer and loss of mass, as indicated by the following equation (Hilditch, 2001):

$$\frac{\dot{P}}{P} = -\frac{2\dot{M}}{(M_1 + M_2)} - \frac{3\dot{M}_2(M_1 - M_2)}{M_1 M_2} + 3K \tag{1.9}$$

This equation considers the additional angular momentum loss (K) for the loss of masses through stellar wind and RLOF studied by Tout & Hall (1991).

1.3 Accretion disc in semi-detached binaries

Mass transfer in binary systems can occur in various configurations and evolutionary stages of its components. The case that interests us to deepen are the semi-detached binaries, where the least massive component is in the stage of filling its Roche lobe (donor) and the massive component is the one that receives the donated material (gainer). So, if we consider a RLOF in the donor star, there will be a flow of gas through the internal lagrangean point L_1 to the primary gainer star. The gas stream will reach supersonic speeds, accelerated by the gravitational attraction of the gainer, and will follow a ballistic trajectory determined by the geometry of Roche's potential. It is expected that most of the gas will slowly rotate in a spiral towards the gainer star, in a series of approximately circular orbits in the orbital binary plane, thus generating an accretion disc. For this to happen, the gas flow must lose angular momentum. This can only happen by angular momentum transfer out of the disc by internal torques. For this reason, the external parts of the disc will gain angular momentum and will spiral outward (for more details consult Frank et al., 1995).

Now, in semi-separated binary systems, mass transfer does not always result in the formation of an accretion disc, as this will depend on the radius of the gainer star, as indicated by a theoretical

study of the dynamics of gas conducted by Lubow & Shu (1975). A critical radius (r_c) is established that the gainer must have in order for a disc to form. The critical radius of Lubow & Shu (1975) can be approximated by Hessman & Hopp (1990) as indicated by the following equation:

$$\frac{r_c}{a} = 0.0859q^{-0.426} \qquad \text{for} \qquad 0.05 < \text{q} < 1 \tag{1.10}$$

where a is the binary sepration and q is the mass ratio and which is accurate to 1%. If the star has a smaller radius, the disc will be prominent. On the other hand, if the star exceeds this critical radius, the impact of the gas flow will be direct on its photosphere. There is a possibility that the gainer has a radius similar to the critical one, in this case an unstable accretion disc will be formed (Lubow & Shu, 1975).

On the other hand, mass transfer will give rise to complex active areas in the accretion disc. At first it was thought that the gas stream generated a hot-spot on the outer surface of the disc, product of the interaction between the gas flow from the donor and the accretion disc (Smak, 1970). Later, using 3-D numerical simulations, it was shown that the dynamics of the gas that gives rise to this active zone is much more complex. The trajectory of the gas entering through L_1 would be diverted by the presence of circumstellar material, which would produce an "extended shock wave"at the edge of the gas stream (Bisikalo et al., 1998, 2000). This result was verified in the β Lyr system using fundamental stellar parameters that were obtained by spectroscopy. The 3-D calculations of gas dynamics indicate that the entrant material is redistributed into two parts, one that is part of an elliptical accretion disc around the donor, while the other part forms the circumstellar structure around the primary. The latter would have a fundamental role in the components observed in this system (Bisikalo et al., 2000).

In semi-detached binary systems of low and intermediate masses, the optical and infrared spectral regions can be used to study the emissions that come from the material that forms the accretion disc or circumestellar material. In that spectral range, emission lines can be observed, which in some cases are double peaked. The most effective way to analyze these lines is through the Doppler tomography technique, which was introduced by Marsh & Horne (1998) and is widely used in the study of emission lines in binary systems type Algol (e.g. Peters (2001); Richards (2004). This tool allows quantitative study of these emissions in a velocity space, delivering a two-dimensional view of three-dimensional mass flows in a binary system (e.g. Mennickent et al.,

2012a,b, 2016). A Doppler tomography analysis performed on the Algol-type binary AU Mon shows an elliptical accretion disc visible in all quadrants, in addition to material that moves at sub-Keplerian speeds associated with material that escapes the mass transfer stream (Atwood-Stone et al., 2012; Richards et al., 2014). Similarly, the Tomography applied to the hot Algol V393 Sco system reveals a emitting structure visible in the first and fourth quadrants (Mennickent et al., 2012a,b). Something similar shows the Doppler maps in the binary system type algol HD 170582, which reveal emission mostly visible in the first and fourth quadrants too (Mennickent et al., 2016b). These are only some cases that have been analyzed observationally and that account complex structures in the accretion disc and circumstellar material, which would be in accordance with hydrodynamic of the gas studies in semi-detached binary systems, mentioned above.

In a conservative case, the entire mass that leaves the donor component of the system would be housed in the gravitational potential of the gainer, either accumulated on it or on an accretion disc. However, this does not always happen. The transferred mass stream interacts with the external part of the accretion disc as indicated by the simulations of Bisikalo et al. (1998, 2000), which could lead to mass loss due to radiation pressure, which would cause bipolar wind (van Rensbergen et al., 2008). This type of wind has been detected in the Beta Lyr system (Harmanec et al., 1996; Hoffman et al., 1998). In the 3-D hydrodynamic simulation performed on that system, it is further demonstrated that the highest rate of energy release occurs in the zone of interaction between the accretion disc and the gas stream from the donor (”extended shock wave”) (Bisikalo et al., 2000). Also, observational evidence of bipolar wind has been found in other systems, such as V 393 Sco (Mennickent et al., 2012a,b), and it is possible that it explains the increase in emission in the first quadrant of the HD 170582 system (Mennickent et al., 2016b).

As we have seen, mass transfer in binary systems has been broadly studied in a theoretical and observational manner, showing that it produces phenomena of a complex nature. Studying them in depth has allowed us to understand the presence of hot and bright spots on the accretion disc, which should be considered in theoretical models applied to the light curves of these systems (as we will see later). Understanding the nature of accretion discs and how they are produced will allow us to go further in understanding such interesting phenomena, such as the Algol-type binary systems that show long photometric cycles and that we will cover more in depth in the next section.

1.4 Double Periodic Variables

In 2003, the photometric analysis of a group of blue stars candidate to *Be* stars in the Large Magellanic Cloud (LMC) using OGLE-II photometry was deepened. In this study, double periodic variable stars (DPVs) were reported for the first time, whose main characteristic was that they had two well defined photometric periods simultaneously (Mennickent et al., 2003). At the same study, a short period P_o of 4 to 16 days and photometric variation amplitude $\Delta I \sim 0.05$ mag, and a long period P_l of 150 to 1000 days and sinusoidal photometric variation of amplitude of $\Delta I \sim 0.2$ mag, were reported for thirty DPVs. Both were directly related by $P_l = 35.2 \pm 0.8 \times P_o$. Subsequent spectroscopic studies confirm that the short period corresponds to the orbital cycle of eclipsing binary stars (Mennickent et al., 2005). Later, once the first catalog of DPVs in the Milky Way was made, confirmed that the DPVs are Algol type binaries (Mennickent et al., 2012a).

To date, catalogs of DPVs have been published in three galaxies. 21 have been reported in Milky Way (Mennickent et al., 2016), 137 in the LMC (Poleski et al., 2010) and 55 in Small Magellanic Cloud (SMC) (Mennickent et al., 2003, 2005; Pawlak et al., 2013). There is still a number to be determined in the catalog of eclipsing binaries towards the galactic bulge generated by Soszyński et al. (2016) (At the moment 34 discovered without publishing by Gonzalo Rojas). In the cases studied, the relationship between the orbital period and the long period is:

$$P_l = \alpha \times P_o \tag{1.11}$$

On average, α is 33, but it varies in cases between 27 and 39 for some particular cases (Mennickent et al., 2016). DPVs have been reported with long variable periods, decreasing in all cases, where the morphology of the long cycle light curve remains relatively constant. In most cases the long cycle light curve has a sinusoidal morphology, but in others this morphology is double-hump (Mennickent et al., 2008; Poleski et al., 2010; Mennickent et al., 2019). Although, the long cycle still remains with an uncertain origin since its discovery to date, different hypothesis have been proposed to explain its origin.

In the majority of the DPVs studied, a theoretical model of binaries with accretion discs developed by Djurašević (1992a,b) has been applied. This code solves the inverse problem, fiting a theoretical light curve to the observed one to find and restrict fundamental stellar parameters and the accretion disc. Once the orbital period is obtained, the radii, masses, temperatures and

luminosity of the components are compared directly with grids theoretical models of stellar evolution, and by optimizing χ^2 the evolutionary state is determined, as described in Mennickent et al. (2012a). Through these analysis the DPVs have been characterized as systems where the gainer has masses between 7-10 $M_\odot$ and the donor between 1-2 $M_\odot$. The latter would be a giant of type *A*-*F* that would be in a case-B mass transfer, forming an optically thick accretion disc around the gainer with characteristics of Be stars (Mennickent et al., 2016). In general, the DPVs would be similar to the semi-detached Algol systems, only that their components would be hotter and more massive.

It was proposed that the eclipsing star OGLE-05155332-6925581 (then OGLE-LMC-DPV-056 in the LMC DPVs catalogue of Poleski et al. (2010)) is a clue to understand the DPVs phenomenon (Mennickent et al., 2008). The long cycle of the system shows a loop in the magnitude color diagram, being more red during the maximum of the cycle and more blue during the descending phase, which could be the product of loss of mass modulated by some mechanism. This hypothesis was supported in an analysis of the speed of discrete absorption components (DACs) as a function of the orbital cycle, which suggested a loss of mass through the Langrangean points L_2 and L_3 that would feed the circumbinary disc. Then, a study of the galactic DPV AU Mon, using high resolution photometry (CORoT) and echelle spectroscopy, shows that the orbital light curve remains unchanged throughout the long cycle (Desmet et al., 2010), and suggest that the long cycle must come from circumbinary material that attenuates the light of the system, supporting the hypothesis proposed for OGLE-05155332-6925581 by Mennickent et al. (2008).

Another galactic DPV that has been studied extensively is V393 Sco (Mennickent et al., 2012a,b, 2018). An analysis of residual spectra showed that the donor has emission lines *Mg II* 4481 and *C I* 6588, homogeneously distributed around the secondary. In addition, it is observed that the lines of Balmer and *He I*, are not eclipsed and that during the maximum of the long cycle they are single-peacked in the orbital phase where the disc is best observed ($\Phi_o \sim 0.5$), which could be produced by high altitude bipolar wind. As observed in AU Mon, there are no changes in its orbital light curve during the long cycle, but it shows a different spectroscopic behavior, since broad emission lines are not compatible with those of circumbinary discs. Thus, for this system, an origin of the long cycle in bipolar Jets is proposed, product of mass transfer. Then, in Mennickent et al. (2015), the HD 170582 system is strategically studied, since its low orbital inclination ($\sim$ 67°) would allow better observing the phenomenon evidenced in V393 Sco. In

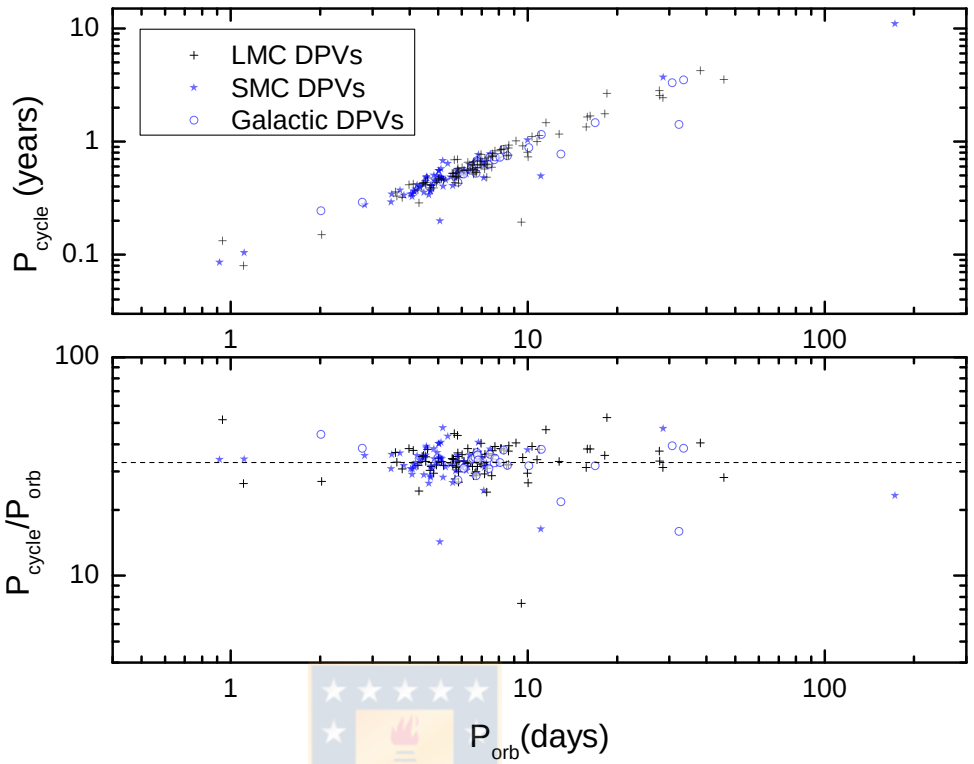

Figure 1.4 Above: Long vs. orbital period for DPVs published in Poleski et al. (2010), Pawlak et al. (2013), Mennickent et al. (2016), and 55 unpublished SMC DPVs discovered by Mennickent and Kolaczkowski. Below: We note that the DPVs discovered in three galaxies show a relationship between $P_{cycle}/P_{orb} = 33$. Image taken from Mennickent (2017).

the study, the fundamental stellar parameters of the HD 170582 system and its accretion disc are obtained by means of a theoretical model applied to the light curves.

For the best model, a disc is fitted with two hot spots that correspond to the hot/bright spot, with temperatures higher by 85% and 56% higher than the disc, respectively. In this sense, a spectroscopic behavior observed in the double absorption line of *He I* 5875 is relevant. One of its components has radial velocity similar to the donor and moves in antiphase during the orbital cycle, which follows that they are formed by wind of the hot/spot, product of the interaction of the material transferred with the accretion disc (Mennickent et al., 2015). A more detailed study of this system, showed by Doppler tomography that the H_α and H_β emission lines changed during the long cycle and that the hot-spot was brighter during the minimum of that cycle (Mennickent et al., 2016b). All this evidence would indicate that the long cycle is modulated by the mass transfer of

the system, which must be modulated in turn by some mechanism. As a solution a theory of a magnetic dynamo for DPVs was proposed by Schleicher & Mennickent (2017) (For more details above DPVs systems see Mennickent (2017)).

1.4.1 Magnetic Dynamo for DPVs

Recently, a theoretical model of magnetic dynamo for DPVs has been proposed by Schleicher & Mennickent (2017). Considering the rapid rotation of the donor star, added to the high speeds in the convective zone, the donor would have the ideal conditions for a potential magnetic dynamo. This would imply changes in the donor's star radius, which in turn would modulate the mass transfer rate (Applegate, 1992).

In order to study the possible magnetic dynamo in DPVs Schleicher & Mennickent (2017) used the relationship between dynamo cycle period P_{cycle} and the rotation period P_{rot} as follows (Soon et al. 1993; Baliunas et al. 1996):

$$P_{cycle} = D^{\alpha} \times P_{rot} \tag{1.12}$$

Where D is the Dynamo number and α an index of the power law, with typical values between 1/3 to 5/6. Different alpha values have been proposed, but this has been controversial, depending on the astrophysical objects considered. In Schleicher & Mennickent (2017) the dependence of D with stellar parameters is analized and for this purpose the relationship between D and the Rosby number $D = R_o^{-2}$ is used. From this analysis an α value is obtained, considering the sample of available objects. If a synchronized orbit is assumed, the donor's rotation period will be equal to the rotational period. In this way, the final relationship they propose is as follows:

$$P_{cycle} = P_{rot}\left[11.5\left(\frac{2\sqrt{2}}{15}\right)^{1/3}\frac{R\odot}{yr}\right]^{-2\alpha} \times \left[\frac{L_2^{2/3}R_2^{2/3}}{M_2^{2/3}}\left(\frac{l_m}{H_p}\right)^{-4/3}\left(\frac{P_{kep}}{\epsilon_H R_2}\right)^2\right]^{-\alpha} \tag{1.13}$$

Where L_2, R_2 and M_2 are the luminosity, radius and mass of the donor star. l_m is the mixing length, H_p the pressure scale height, P_{Kep} the Keplerian orbital period of a test particle on the surface of the donor star and ϵ_H as a fraction of H_p.

Using a set of DPV whose stellar parameters have been previously determined, and using a value of $\alpha = 0.31$, $\epsilon_H = 1$ and $l_m/H_P = 1$, the theoretical P_{cycle} is directly compared with those

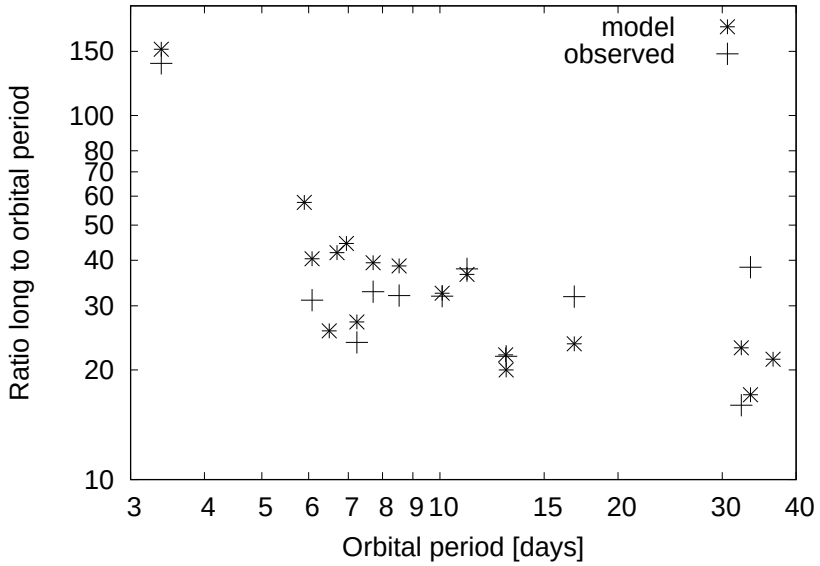

Figure 1.5 Ratio between observed long period and theoretical (using Eq. 1.13) vs observed orbital period. 17 systems were used, noting a good agreement between the long cycle period obtained by the model and those observed. Image obtained from Schleicher & Mennickent (2017)

observed, achieving a good similarity. This is why they conclude that the magnetic dynamo in the donor star could be the origin of the long cycle present in the DPV (Schleicher & Mennickent, 2017; Mennickent et al., 2018).

1.5 This thesis

The main objective of this thesis is the photometric analysis of light curves of DPVs in the Large and Small Magellanic Clouds. For that we used photometry available in the OGLE database that covers up to 18 years of observation with about 2000 observations per object. This has allowed us to study unique behaviors in these systems.

In Chapter 3 we show the analysis of the OGLE-LCM-DPV-097 system. It presents the most drastic morphology changes in the orbital light curve through the different stages of the long cycle. For the first time we applied theoretical models to the different light curves in the ascending, maximum, descending and minimum stages of the long cycle. Our models explained the observed changes by cyclic transformation of the physical characteristics of the accretion disc.

In Chapter 4 we examined the light curves of the OGLE-BLG-ECL-157529 system. In this object we also found drastic changes in the morphology of its orbital light curves, which we explain by changes in the accretion disc. We investigate the possibility that this is due to variable rates of mass transfer.

In Chapter 5 we show the case of the binary OGLE-BLG-ECL-253799. In its orbital light curve an inversion of the of the primary and secondary minimum is observed. We investigated its DPV nature but we did not find a long cycle. It seems that the variations in the characteristics of the accretion disc is due to a transitory mass transfer process.

In Chapter 6 we show a photometric study of 142 LMC and SMC DPVs. We analyzed the dispersion of the long cycle in DPVs with eclipsing and ellipsoidal orbital light curves, finding a lower photometric dispersion in the the latter. In addition, we show 11 systems with changes in their orbital light curves. We examined their residuals and found combinations of frequencies in most cases. Additional frequencies found in previous studies were eliminated considering long-term variations.

2

Photometric data analysis

2.1 Photometric data

Our study was carried out with OGLE (The Optical Gravitational Lensing Experiment) photometry of the OGLE-II-III-IV database. The different campaigns have been carried out with the 1.3 m Warsow telescope, from the Cerro Las Campanas Observatory, Chile, operated by the Carnegie Institution of Washington.

The instrumentation used has varied over the years, increasing the tracking capacity more and more. During the OGLE-II campaign (1997-2000, Udalski et al., 1997), the telescope has operated using a single SITe ccd detector with 2048×2048 pixel and a pixel size of 24 μm, giving a scale of 0.417 arcsec/pixel and a field of view of 14×14 arcmins. Afterwards, during the OGLE-III campaign (2001-2009,, Udalski, 2003), the telescope was equipped with eight CCD detectors SITe ST-002A with 2048×4096 pixels and a pixel size of 14 μm, each one with a scale of 0.26 arcsec/pixel and with a field of view of 35×35 arcmins. Still, these only covered 20% of the total field of view available in the focal plane of the telescope, so in 2009 the telescope was equipped with 32 CCDs detectors of 2048×4102 pixel, with a pixel size of 15 μm, which allows filling the focal plane properly (~ 300 mm of diameter) (OGLE-IV, see Udalski et al., 2015).

For the photometric reduction, different OGLE pipelines described in Udalski et al. (1997) (OGLE-II) and Udalski (2003) (OGLE-III-IV) are used. In all campaigns, photometry is obtained using the Difference Image Analysis (DIA) method (Alard & Lupton, 1998; Alard, 2000; Wozniak, 2000), which implements an image subtraction algorithm and is very efficient in dense star fields.

For more details on the different steps of reduction, photometry acquisition and calibration to the standard VI system see Udalski et al. (1997); Udalski (2003); Udalski et al. (2015) for the OGLE-II, III and IV campaigns, respectively.

The photometry obtained in OGLE has always used filters close to the standard VI bands. This has allowed a simple transformation and calibration of the OGLE photometry to the standard system in its different campaigns. The OGLE I-band (centered in 8000 Å) is close to the standard Kron-Cousins I-band filter, while the OGLE V-band (centered in 5500 Å) is somewhat different from the standard Johnson V-band (Udalski et al., 2015).

The OGLE database is considered one of the most accurate photometric campaigns carried out from the ground. Although it grants photometry of different variable objects of scientific interest, our study is focused on DPVs systems (See Section 1.3). These were first detected in a study conducted by Mennickent et al. (2003), in which 27 LMC and 3 SMC objects were reported using OGLE photometry. Then, Poleski et al. (2010), published 125 new objects in LMC, making the first OGLE-DPVs catalog and including the objects found by Mennickent et al. (2003). In Pawlak et al. (2013), OGLE photometry is tracked in search of DPVs in SMC, reporting 21 DPVs. To date, the vast majority of cataloged DPVs have been observed in the new OGLE campaign, adding up to 2000 observations in I-band for LMC and SMC DPVs (average of 1160 measurements) and approximately 17.2 years of observations. This will allow us to study the DPV phenomenon in depth, analyzing long period variations, photometric changes in the orbital light curves, among others, for which a stable photometry is required over the years.

In a complementary way, only in some cases we show Massive Compact Halo Object (MACHO) project photometry available for some objects of interest (Allsman et al., 2001). The MACHO light curves have photometry in two bands. The filter red (centered in 7000 Å) and blue (centered in 5200 Å). Both with equal and similar amount of measurements that in some cases are simultaneous. For more details of the instrumentation and the methods of data acquisition see Allsman et al. (2001).

2.2 PDM and GLS periodogram

For the analysis of time series we use periodograms widely used in the search and analysis of frequencies. Particularly, our goal is to verify already published periods of the objects that we

analyzed in this study, because we have increased the time range of observations for many of them. For this we use the phase dispersion minimization (PDM) method developed in IRAF [1], which also allows us to quickly visualize the orbital and long cycle curves of the DPVs studied. Also, we want to analyze the additional frequencies in the residuals of the disentangled of the light curves. For this, we find it quite useful to use the generalised Lomb-Scargle (GLS) periodogram, since the peak of additional frequencies and frequency combinations, previously published for some objects (see Chapter 6), are easily visualized in their frequency spectrum. Next we will briefly describe the operation of both periodograms.

2.2.1 Phase dispersion minimization method

The PDM method is quite useful when analyzing signals with non-sinusoidal time variation, in addition to small and randomly spaced samples. Proposed by Stellingwerf (1978), it works with the following principle. If we consider a data set with N observations of the form (x_i, t_i), with $i = 1, 2, \ldots, N$, where t_i is the observation time and x_i is the magnitude of the object at that time, the variance of the magnitude x for the entire sample will be given by the following equation (Stellingwerf, 1978):

$$\sigma^2 = \frac{\sum (x - \bar{x})^2}{N - 1} \tag{2.1}$$

where $\bar{x}$ is the mean of the measured magnitudes $\bar{x} = \sum x_i / N$. Now, if we divide the data set into M different samples, each interval will have a variance s_j^2 and n_j (with $j = 1, M$) number of observations. The total variance S^2 for the entire sample will be (Stellingwerf, 1978):

$$S^2 = \frac{\sum (n_j - 1) s_j^2}{\sum n_j - M} \tag{2.2}$$

Now, we wish to minimize the variance of the data with respect to the mean value of the light curve. For this, each sample N is given a trial period, which will assign a phase between 0 and 1, to each observation epoch. The variance of each sample will give us a measure of the scatter around the average light curve. Then, we can relate both quantities using $\Theta = S^2/\sigma^2$, whose value will range between 0 and 1. If we consider a representative period of the data set, the ratio of both will be small and close to zero. On the other hand, if we consider a false period, the relationship

[1] IRAF is distributed by the National Optical Astronomy Observatories, which are operated by the Association of Universities for Research inAstronomy, Inc., under cooperative agreement with the National ScienceFoundation.

of both will tend to unity. For this reason, in the periogram the lower value of Θ represents the frequency implicit in the observational data (See Stellingwerf (1978)).

2.2.2 Generalised Lomb-Scargle periodogram

The Lomb-Scargle periogram has been widely used in the search and analysis of frequencies in time series. Equivalent to fit of least squares of sine waves, the equation for the periodogram was developed by Barning (1963), Lomb (1976) and Scargle (1982). However, the classic Lomb-Scargle periodgram has two main deficiencies, since it does not take into account the error associated to the measurements and also subtracts the mean of the data.

In Zechmeister & Kürster (2009) a generalised Lomb-Scargle (GLS) periodgram is proposed, that including an offset c to the sinusoidal adjustment function ($y = a\cos\omega t + a\sin\omega t + c$), in addition to considering errors. The new GLS periogram, provide more precise frequencies, better determines the spectral intensity, in addition to being not susceptible to aliases (Zechmeister & Kürster, 2009). The equation that determines the power of a frequency in the periogram is given by the following equation (Zechmeister & Kürster, 2009):

$$p(\omega) = \frac{1}{\sum_i w_i (y-\bar{y})^2}\left[\frac{\left[\sum_i w_i (y-\bar{y})\cos\omega(t_i-\tau)\right]^2}{\sum_i w_i^2\cos^2\omega(t_i-\tau)} + \frac{\left[\sum_i w_i (y-\bar{y})\sin\omega(t_i-\tau)\right]^2}{\sum_i w_i^2\sin^2\omega(t_i-\tau)}\right] \tag{2.3}$$

where the parameter τ is calculated via:

$$\tan 2\omega\tau = \frac{\sum w_i \sin 2\omega t_i - 2\sum w_i\cos\omega t_i \sum w_i \sin\omega t_i}{\sum w_i\cos 2\omega t_i - \left[(\sum w_i\cos\omega t_i)^2 - (\sum w_i \sin\omega t_i)^2\right]} \tag{2.4}$$

We observe that Eq. 2.3 and 2.4 are similar to described in the classic Lomb-Scargle periodogram (see Scargle, 1982), only now that the weight of errors w_i are considered. For more information on obtaining the above equations see Zechmeister & Kürster (2009).

2.3 Light curve disentangling

As we have seen, DPVs present two photometric cycles. For a better analysis of the orbital curves and long cycle, it is fundamental to perform a disentangling of both of them. For that we use a specially designed algorithm to disentangle multiperiodic light curves through the analysis of their

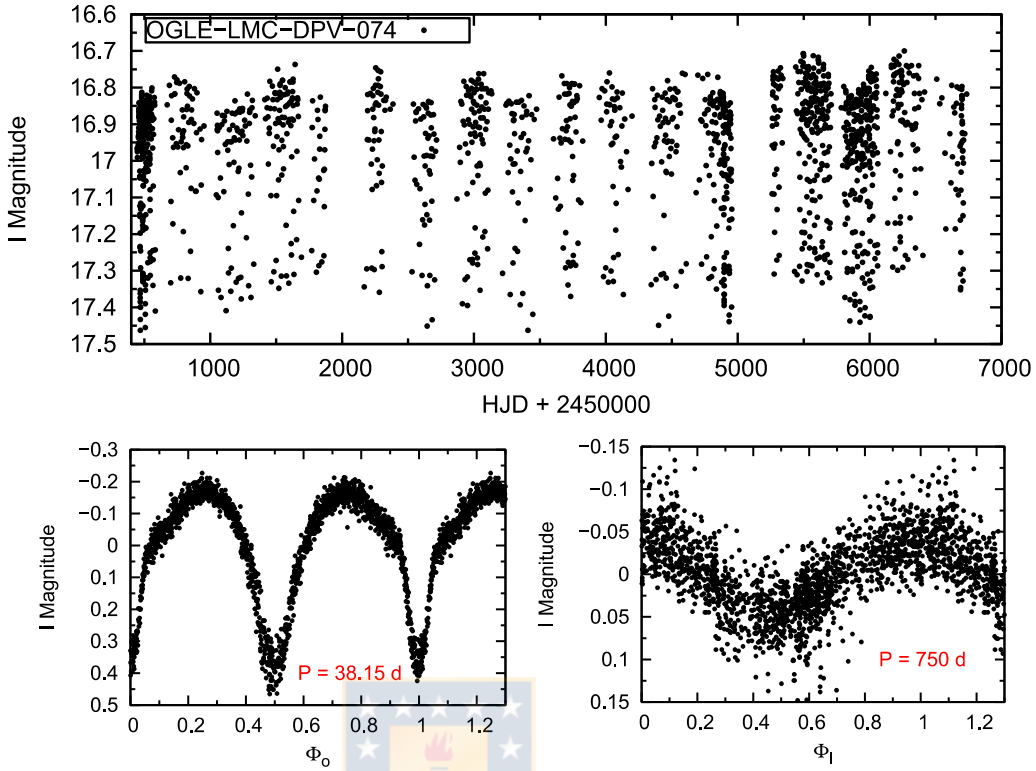

Figure 2.1 Above: Photometry without pre-whitening available in the OGLE II-III-IV campaigns for the OGLE-LMC-DPV-074 system (Poleski et al., 2010). Below: Orbital (left) and long cycle (right) curves after the disentangle.

Fourier component amplitudes. The first thing is to find the principal frequency f_1 involved in the photometric data, which usually corresponds to the orbital cycle. For this purpose, period search algorithms are used, such as phase dispersion minimization (PDM). The light curve undergoes a process of least square fitting by sinusoidal fitting functions with phases and amplitudes that varies, which describes the principal frequency with its harmonics. After the first fit, the residuals are examined in order to search for a new periodicity f_2, which usually corresponds to the long cycle in DPVs . This is afterwards included in the following fit. In this manner, we obtain the best representation of the light curve. The residual data regarding the first and second theoretical light curves will provide us the photometric series of the long and orbital cycle, respectively (Mennickent et al., 2012a). In some cases, the long cycle has a variable period. For a better disentangle we divide the photometric series into different sections, in order to assume a representative constant period for each section. The same procedure mentioned in the previous paragraph is applied to

each interval.

2.4 The light curves analysis methodology

2.4.1 Orbital and Long period inspection

In this study we will analyze DPVs in LMC Poleski et al. (2010) and SMC Pawlak et al. (2013) that are in the OGLE I-band database. All of them have long and orbital periods, and their respective errors. In these catalogs, DPVs have not been reported with period changes in the orbital cycle, but there are cases in that the long period varies considerably, decreasing in all cases (Mennickent et al., 2008; Poleski et al., 2010; Mennickent et al., 2016, 2019). To perform the disentangle of the light curve, we use initially, the frequencies already published for these objects. Then, through the PDM task in IRAF, we made a visual inspection of both light curves, in order to corroborate if they are representative. In the case of a constant long period, we will observe a well defined light curve, sinusoidal in most cases. If the long period varies, we will notice a fairly noisy light curve and without a defined morphology. In this last case, we will divide our data in different sets. These will have a certain amount of long cycle, for which we will assume a constant long period. We will apply the disentangled light curves to each established set.

2.4.2 Light curves ephemerides/phases and long cycle stages

We will use the following ephemeris for the orbital orbital light curves $HJD_{min} = T_{min} + P_o \times E$, where T_{min} is the epoch where a primary minimum of the orbital light curve is produced and P_o the orbital period. For the long cycle we will use $HJD_{max} = T_{max} + P_l \times E$, where T_{max} represents an epoch where the long cycle reaches its maximum and P_l its long period. In the case of a variable period, an ephemeris must be obtained for each set of data. To establish the orbital phases and the long cycle we use the following:

$$\Phi_{o,l} = \frac{T - T_{min,max}}{P_{o,l}} - \text{int}\left[\frac{T - T_{min,max}}{P_{o,l}}\right] \tag{2.5}$$

Using this equation we will make sure that in $\Phi_o = 0$ the minimum of the orbital light curve actually occurs and that in $\Phi_l = 0$ the maximum of the long cycle occurs.

We have observed that DPVs with variable long period remain with a long cycle curve mor-

phology constant. We will define an ephemeris and a long cycle phase for each set of data and we will be able to join the curves of each set in a single long cycle phase. This process will be fundamental for the subsequent analysis.

On the other hand, we know that some LMC DPVs present evident changes of the primary and secondary minimum of the orbital light curve directly related to the long cycle Poleski et al. (2010). Taking advantage of the good photometric coverage of OGLE to the DPVs in LMC and SMC, we want to investigate variations in the morphology of the light curve that are directly related to the long cycle. We will do it in the following way: for DPVs with sinusoidal long cycle light curves, we will divide one phase of the complete long cycle into fourth stages, Ascending ($0.6 \leq \Phi_l < 0.9$), Maximum ($0.9 \leq \Phi_l < 1.1$), Descending ($0.1 \leq \Phi_l < 0.35$) and Minimum ($0.35 \leq \Phi_l < 0.6$) of the long cycle. Although these ranges are defined rather arbitrarly, it is expected that they can provide a clear description of the changes observed in the orbital light curve through different stages of the long-cycle. Slight changes in the boundaries of the aforementioned ranges should not affect the results significantly. In any case, we will analyze these ranges case by case, since they could change slightly in some DPVs. We will use the observations epochs of the orbital cycle, but this time considering the ephemeride of the long cycle to obtain Φ_l. In this way, we will can divide the orbital light curves in the stages Asc, Max, Des, Min of the long cycle.

2.4.3 Searching orbital light curve changes related with the long cycle

The orbital light curves are periodic, so we can use series of cosines and sines to make mathematical fits:

$$m(t) = A_0 + \sum_{i=1}^{N} a_i \cos(2\pi\Phi_o(t)) + \sum_{i=1}^{N} b_i \sin(2\pi\Phi_o(t)) \tag{2.6}$$

where m(t) is the observed magnitude at time t, A_0 is the mean magnitude and a_i, b_i are the amplitude components of $(i-1)^{th}$ harmonic. The value of Φ_o is from 0 to 1, corresponding to a full orbital cycle.

We have decided to use, arbitrarily, the orbital curve in the maximum phase of the long cycle as the basis of our analysis. We will make fits using Fourier series and then directly compare this mathematical fit with the orbital light curves in the other stages of the long cycle. In the residuals we can observe the following cases: i) If there are no changes in the orbital light curves, through the different stages of the long cycle, we will observe values around 0 distributed homogeneously

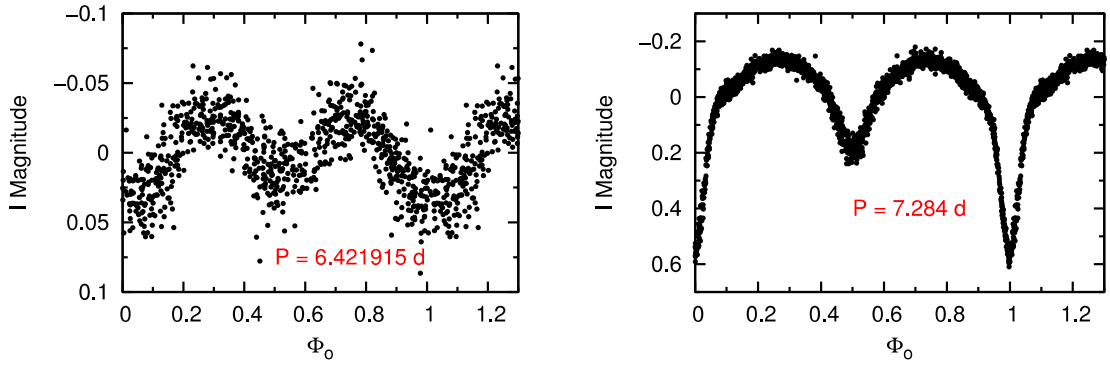

Figure 2.2 Examples of ellipsoidal and eclipsing light curves in DPVs. Left: OGLE-LMC-DPV-056 orbtial light curve. Right: OGLE-LMC-DPV-074 orbital light curve (Poleski et al., 2010)

in the residuals. ii) If there were changes in the orbital light curves, through the different stages of the long cycle, we will observe the opposite to the previous case. In the latter case, we will notice an increase in the dispersion of the residuals in specific phases of the orbital cycle and it will be these that are changing their morphology in relation to the orbital light curve in the high phase. In this way we can quickly identify which DPVs present changes in their morphology of orbital light curves in relation to the long cycle, in addition to knowing in which orbital phases are produced.

2.4.4 ELL and ECL classification

We divided into two groups the orbital light curves of our objects, ellipsoidal (ELL) and eclipsing (ECL). ELL variability is a phenomenon observed in close binary systems and is caused mainly by the rotation of the component that has filled its Roche lobe, which is distorted by tidal effects (See Section 1.2). They typically have a sinusoidal type morphology, with two maximums in the 0.25 and 0.75 orbital phases, which occur when the largest surface area of the Roche lobe is projected. They also show two minimums, which are not equal generally, but differ slightly in depth (Soszynski et al., 2004). The ECL variability also has two maxima in the 0.25 and 0.75 orbital phases, which occur when both components are visible. The primary minimum is easily recognizable and is usually considerably deeper than the secondary minimum (see Figure 2.2). The main difference between the binaries that produce both variabilities, is the inclination of the orbital plane with which we observe them, presenting the ECL inclinations close to $i = 90°$, while the ELL inclinations lower to that value.

2.5 Theoretical light curve model

We analysed the orbital light curves with a program developed by Djurašević (1992a), which implements a sophisticated and versatile binary star model based on Roche geometry. This program has been used and tested for more than two decades on a wide range of binary configurations (e.g. Djurašević et al., 2008; Djurašević et al., 2010; Djurašević et al., 2012; Mennickent et al., 2012a, 2016b; Garcés L. et al., 2018). The system parameters that best fit the observed light curve are estimated using the Marquart-Levenberg algorithm with modifications described in Djurašević (1992b) to minimize the sum of squared residuals between the observed (O) and calculated (C) light curves. As we have mentioned, studies prior to DPV systems consider accretion discs around the gainer. For our theoretical models to be representative we also add it to our model.

2.5.1 Accretion disc model

The code considers the system of a secondary star and a primary surrounded by an accretion disc, that is both optically as geometrically thick. The disc edge is approximated by a cylindrical surface. The thickness of the disc can change linearly with radial distance, allowing the disc to take a conical shape (but it can be, convex, concave, or plane-parallel) as a generalization to the simple concave disc model suggested by Zola (1991) and Zoła & Ogłoza (2001). The geometrical properties of the disc are determined by its radius ($\mathcal{R}_d$), its thickness at the edge (d_e), and the thickness at the centre (d_c). The cylindrical edge of the disc is characterized by its temperature (T_d), and the conical surface of the disc by a radial temperature profile that follows a modified version of the temperature distribution proposed by Zola (1991):

$$T(r) = T_d + (T_h + T_d)\left[1 - \left(\frac{r - \mathcal{R}_h}{\mathcal{R}_d - \mathcal{R}_h}\right)\right]^{a_T} \tag{2.7}$$

We assume that the disc is in physical and thermal contact with the gainer, so the inner radius and temperature of the disc are equal to the temperature (T_h) and radius ($\mathcal{R}_h$) of the star. The temperature of the disc at the edge (T_d) and the temperature exponent (a_T), as well as the radii of the star ($\mathcal{R}_h$) and of the disc ($\mathcal{R}_d$) are free parameters, determined by solving the inverse problem (Djurašević et al., 2008).

On the other hand, as we have reviewed in previous sections, theoretical studies of gas hy-

drodynamics show certain active areas in the accretion disc that should be included in our model (Bisikalo et al., 1998, 2000). One of them is the commonly called hot-spot. Originally it was attributed to the direct interaction between the mass stream and the accretion disc (Smak, 1970), but 3-D hydrodynamic simulations indicate its origin is due to the interaction of the gas stream and the circumstellar material, forming a "wave of intensive shock" (Bisikalo et al., 1998, 2000). In our model we will understand this wave as a **Hot Spot**. This could produce a local concentration of radiation and diverting its uniform azimuthal distribution. In the code this effect is considered by an angle ($\theta_{\rm rad}$) between the line perpendicular to the surface of the edge of the disc and the direction of the maximum radiation of the hot spot. Depending on this angle ($\theta_{\rm rad}$), the maximum radiation flow can be shifted slightly in the accretion disc, producing asymmetries around the secondary maximum and primary minimum of the light curve (Djurašević et al., 2008).

It is also considered another active zone called **Bright Spot**. Hydrodynamic models also predict spiral structures in the accretion disc. The tidal force exerted by the donor star produces one or two spiral arms that extend outward from the disc, forming a hump in the outer area (Heemskerk, 1994). The bright spot is generally in the outer zone opposite the hot spot in the accretion disc and can have an additional interpretation considering the complex dynamics of the gas in hydrodynamic simulations performed by Bisikalo et al. (1998, 2000); Harmanec et al. (2002); Nazarenko & Glazunova (2003, 2006a,b), as mentioned in Djurašević et al. (2008).

Both active zones are modeled considering temperature, angular size and lengths. The angular size considers the dimensions of the zones that will depend in turn on the external dimensions of the disc. The length is measured in a clockwise direction with respect to the line joining the centers of both stars in the orbital plane, seen from the orthogonal axis +Z. This goes from $0° - 360°$ (Djurašević et al., 2008).

This active zones in the accretion disc modify the azimuthal distribution of radiation from the accretion disc, producing asymmetry in light curves. In some cases, including only one hot spot in the models, it was not enough for a good theoretical fit to the light curves (Mennickent & Djurašević, 2013). For this reason, although there is no well-defined origin of the area we call brigth spot, its inclusion undoubtedly significantly improves the fit to light curves (Djurašević et al., 2008; Djurašević et al., 2010; Djurašević et al., 2012; Mennickent et al., 2012a, 2016b; Garcés L. et al., 2018).

3

Structural changes in the hot Algol OGLE-LMC-DPV-097 and its disc related to its long cycle

This study led to the publication of the letter Garcés L. et al. (2018)

3.1 Abstract

Double Periodic Variables (DPVs) are hot Algols showing a long photometric cycle of uncertain origin. We report the discovery of changes in the orbital light curve of OGLE-LMC-DPV-097 which depend on the phase of its long photometric cycle. During the ascending branch of the long cycle the brightness at the first quadrature is larger than during the second quadrature, during the maximum of the long cycle the brightness is basically the same at both quadratures, during the descending branch the brightness at the second quadrature is larger than during the first quadrature, and during the minimum of the long cycle the secondary minimum disappears. We model the light curve at different phases of the long cycle and find that the data are consistent with changes in the properties of the accretion disc and two disc spots. The discs size and temperature change with the long-cycle period. We find a smaller and hotter disc at minimum, and larger and cooler disc at maximum. The spot temperatures, locations, and angular sizes also show variability during the long cycle.

3.2 Introduction

In the close interacting binaries Double Periodic Variables (DPVs) a giant fills its Roche lobe and transfers mass on to a B-type dwarf feeding an optically thick accretion disc. About 250 DPVs have been found in the Galaxy and the Magellanic Clouds (Poleski et al., 2010; Pawlak et al., 2013; Mennickent, 2017). Typical orbital periods are few days and long cycles last hundreds of days. The long cycle lasts in average about 33 times the orbital period, but single period ratios run typically between 27 and 39. DPVs have been recently reviewed by Mennickent et al. (2016); Mennickent (2017).

The more enigmatic fingerprint of a DPVs is its long cycle. It has been attributed to recurrent mass loss Mennickent et al. (2008, 2012b). The triggering mechanism might be the magnetic dynamo of the rapidly rotating donor that should modulate the mass transfer through the inner Lagrangian point Schleicher & Mennickent (2017). A careful inspection of these hypotheses is needed in a number of systems before to validate them.

In this chapter, we present our analysis of the light curve of OGLE-LMC-DPV-097 (α_{2000} = 05:34:18.06, δ_{2000} = -70:38:08.7; MACHO 11.8746.65, 2MASS J05341808-7038087). This object is classified with orbital period 7.751749±0.000202 d and long cycle 302.622 ± 0.109 d by Poleski et al. (2010). OGLE-LMC-DPV-097 has one of the largest amplitude long cycles among DPVs viz.0.717 mag in the I-band. In this study, we extend the data analysed by Poleski et al. (2010) including OGLE-IV photometry and present new and interesting results potentially useful to explain the DPV phenomenon.

3.3 Photometric Data

The photometric time series analysed in this study are taken from the OGLE-III/IV project data bases. The OGLE-IV project is described by Udalski et al. (2015). The whole data set, summarized in Table 3.1, spans a time interval of 4569 d, i.e. 12.5 yr.

3.4 Light curve disentangling

We disentangled the light curve into an orbital and long-cycle part with the aid of a Fourier decomposition algorithm described by Mennickent et al. (2012a) and the ephemerides for the orbital

Table 3.1 Summary of photometric observations. The number of measurements, starting and ending times, and average magnitude are given. HJD zero-point is 2450000. Single point uncertainties are between 4 and 6 mmag

Data Base	N	HJD_{star}	HJD_{end}	Mag	Band
OGLE-III	443	2167.89750	4954.538 50	16.086	I
OGLE-IV	580	5260.63876	6736.620 11	16.140	I

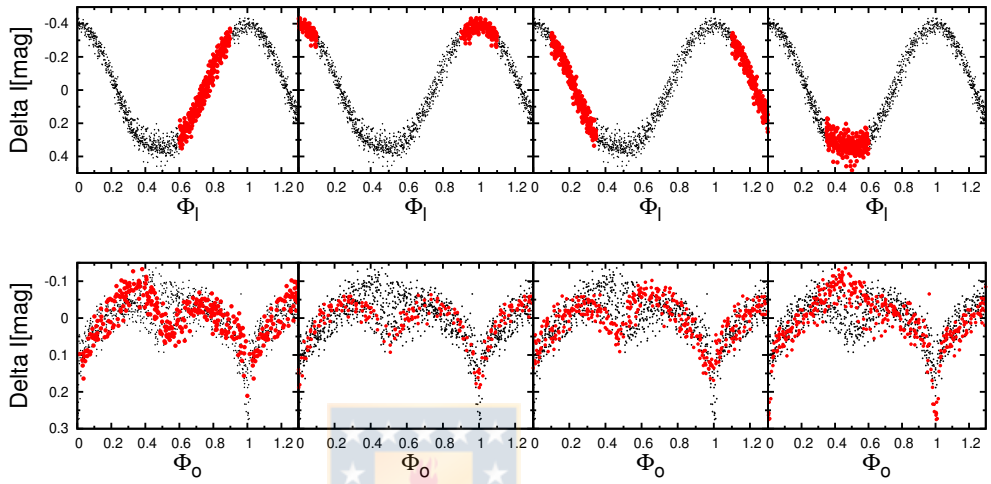

Figure 3.1 Disentangled long cycle (up) and orbital (down) light curves phased with the respective periods. Black dots show the complete data set, red dots show segments of the data of the long cycle. It is evident the change in orbital light curve shape at different long cycle phases (Garcés L. et al., 2018).

and long periods given by Poleski et al. (2010).

The orbital and long cycle light curves phased with the respective periods show an interesting behaviour that can be summarized as (Fig. 3.1): (a) during the ascending branch of the long cycle the brightness at the first quadrature (Φ_o = 0.25) is larger than during the second quadrature (Φ_o = 0.75), (b) during the maximum of the long cycle the brightness is basically the same at both quadratures, (c) during the descending branch the brightness at the second quadrature (Φ_o = 0.75) is larger than during the first quadrature (Φ_o= 0.25), and (d) during the minimum of the longcycle the secondary minimum disappears. Furthermore, we have found that the variability is larger around the eclipses and it occurs smoothly during the long cycle (Fig. 3.2). The above behaviour suggests that there are structural changes in the binary (stars, gas stream, disc, circumstellar matter) related to the long cycle. This is a strong constraint for any competent model intending to explain the long cycle in this DPV.

3.5 Results: Light curve model

In order to qualitatively understand the orbital light changes we separately analysed the orbital light curves on the ascending, top, descending, and minimum branches with a program developed by Djurašević (1992a) which implements a sophisticated and versatile binary star model based on Roche geometry. This program has been used and tested for more than two decades on a wide range of binary configurations (e.g Djurašević et al., 2010; Mennickent et al., 2015). The system parameters that best fit the observed light curve are estimated using the MarquartLevenberg algorithm with modifications described in Djurašević (1992b) to minimize the sum of squared residuals between the observed (O) and calculated (C) light curves.

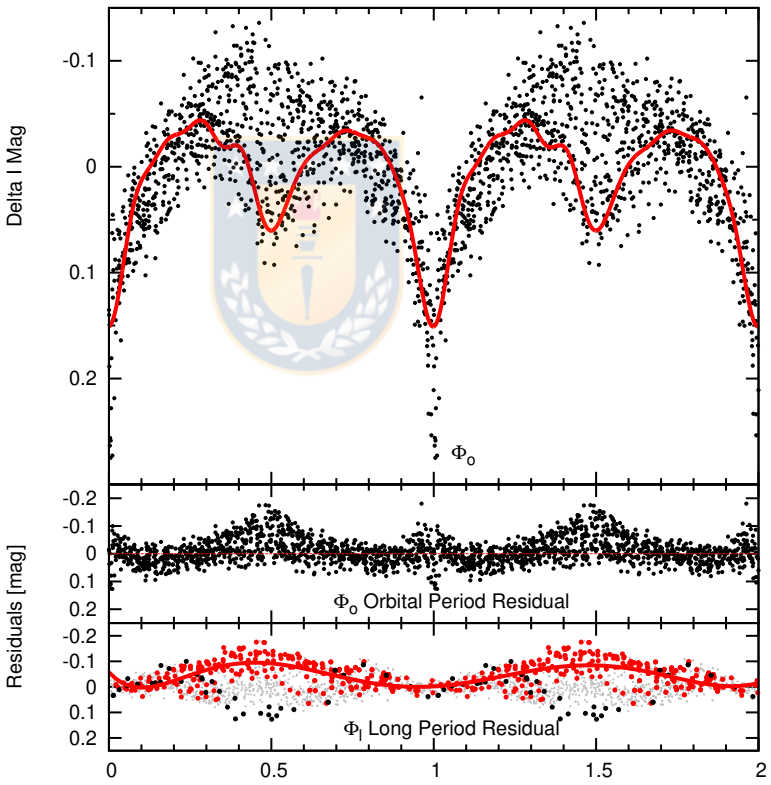

Figure 3.2 The upper panel shows the orbital light curve and a fit to the data obtained on maximum (red line). The middle panel shows the residuals of the fit, indicating that the larger variability occurs on times of eclipses. The bottom panel shows the same residuals that above, but in the x-axis the long-cycle phase is shown. Red points are data taken around the secondary eclipse ($0.45 \leq \Phi_o \leq 0.55$) and black points around the main eclipse ($0.98 \leq \Phi_o \leq 1.02$); the changes in the eclipses depth occur smoothly during the long cycle (Garcés L. et al., 2018).

In absence of spectroscopic data we use educated approximations to model the system. OGLE-LMC-DPV-097 has MACHO catalogue colour V-R = -0.046, so we use T_1 = 14 K for the gainer. In addition, we assume synchronous rotation for the stellar components and q = 0.2. Based on the studied systems these figures can be considered representative for a DPV (Mennickent et al., 2016). With this approximation, we do not intend to get accurate system parameters for our system, at least not in this study, but to get a qualitative description of the differential changes occurring in the system during the long cycle. For this reason we do not focus on the absolute stellar properties in this chapter. A trial using q = 0.15 gives similar qualitative results to reported in this chapter and suggests typical errors of 20 per cent for the disc radius, temperature, and spots temperature ratio.

Following earlier work with DPVs, our model assumes an optically and geometrically thick disc. The disc edge is approximated by a cylindrical surface.The thickness of the disc can change linearly with radial distance, allowing the disc to take a conical shape (convex, concave, or plane-parallel). The geometrical properties of the disc are determined by its radius ($\mathcal{R}_d$), its thickness at the edge (d_e), and the thickness at the centre (d_c). The cylindrical edge of the disc is characterized by its temperature, (T_d) , and the conical surface of the disc by a radial temperature profile that follows the temperature distribution proposed by Zola (1991) (Eq. 2.7).

We assume that the disc is in physical and thermal contact with the gainer, so the inner radius and temperature of the disc are equal to the temperature and radius of the star. The temperature of the disc at the edge (T_d) and the temperature exponent (a_T), as well as the radii of the star ($\mathcal{R}_h$) and of the disc ($\mathcal{R}_d$) are free parameters, determined by solving the inverse problem. We refined the model of the system by introducing hot active regions on the edge of the disc. Our model includes two such active regions: a hotspot (hs) and a bright-spot (bs). These regions are characterized by their temperatures, angular dimensions, and longitudes. These parameters are also determined by solving the inverse problem and are given in Table 3.2. The models are compared with the observations in Fig. 3.3

3.6 Discussion

We find that changes in orbital light-curve shape can be explained as changes in system parameters, especially those related to the disc and hotspot/bright-spot. The disc is smaller and hotter at

long-cycle minimum while it is larger and cooler at long-cycle maximum. The amplitude of the temperature variation is 2840 K, being the minimum reached during the ascending branch. The hot spot has maximum temperature relative to the disc at minimum of the long-cycle while the bright spot does it during the ascending branch. While the hot spot position shows a small variation during the long-cycle with λ_{hs}=341°.5 - 349°.2, the bright spot moves along the disc outer rim during the long-cycle with λ_{bs}=114°.6 - 255°.2. We notice that the hot spot in seven DPVs is found at λ_{hs}(average)=327°.7 ± 5°.6 (std) while the bright spot in the same systems is found in the range λ_{bs}=107° - 162° (Mennickent, 2017). This suggests that bright spots tends to occupy broader disc regions than hot spots. In LMC-DPV-97, when the bright spot is opposite to the donor, the secondary eclipse disappears, this happens at long-cycle minimum coinciding with the smaller disc size.

Moving bright spots have been reproduced by 3D simulations of gas dynamics in the cataclysmic variable V455 And, and interpreted in terms of interactions of a density wave (DW) with shockregions; in this model the DW is in retrograde precession with angular velocity few percent lower than the orbital velocity of the system. As a result, the times when the density wave interacts withthe shocks will be increasing delayed in orbital phase with eachsuccessive rotation (Kononov et al., 2015). Future studies couldindicate if this model can be successful for explaining the movingbright spots found in LMC-DPV-97.

We notice that the increase in hotspot angle λ_{hs} is in principle consistent with the increase in disc size, if the hotspot is the site where a free-fall stream hits the disc (Flannery, 1975). Even if the stream interacts with a gas envelope forming a hot line in the outer disc border as suggested by Bisikalo et al. (1997), the spread of this region along with the low mass ratio might help to keep small the variability of the λ_{hs} parameter.

3.7 Conclusion

We find changes in the orbital light curve of DPV-097 linked to the phase of the long-cycle. A preliminary analysis of the light curve indicates that changes in disc size/temperature and spot temperature/position can explain the different observed light curves during the long-cycle. Especially interesting is the result that at minimum of the long-cycle the disc is smaller and hotter and the spots are also hotter, while at maximum the disc is larger and cooler. A more detailed study of

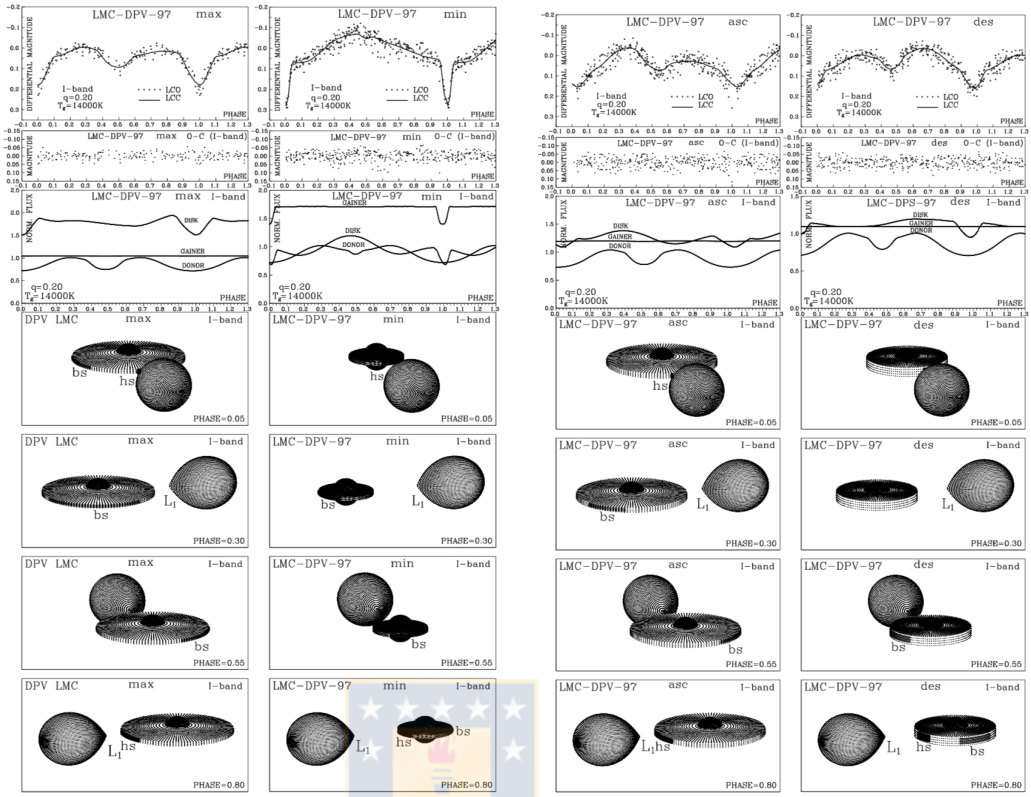

Figure 3.3 The model compared with observations and residuals on the ascending and descending branches of the long cycle. Relative flux contributions are in the third panel and representative views of the system at different phases are also given (Garcés L. et al., 2018).

this object is in preparation.

Table 3.2 Results of the analysis of the orbital light curves obtained by solving the inverse problem for the Roche model with an accretion disc around the more-massive (hotter) component.

Quantity	Asc	Max	Des	Min	Quantity	Asc	Max	Des	Min
n	370	200	380	387	$A_{bs1} = T_{bs}/T_d$	1.78	1.17	1.16	1.76
$\Sigma(O-C)^2$	0.3310	0.0772	0.2439	0.2754	$\theta_{bs}[^\circ]$	23.3	54.4	26.2	49.0
σ_{rms}	0.0299	0.0197	0.0254	0.0267	$\lambda_{bs}[^\circ]$	137.2	114.6	255.2	169.6
$i[^\circ]$	74.3	75.1	74.4	74.4	Ω_h	8.682	8.699	8.681	8.681
F_d	0.93	0.94	0.68	0.46	Ω_c	2.233	2.233	2.233	2.233
T_d[K]	4030	5580	5210	6870	$\mathcal{M}_h[\mathcal{M}_\odot]$	5.51	5.51	5.51	5.51
$d_e[a_{orb}]$	0.044	0.034	0.082	0.031	$\mathcal{M}_c[\mathcal{M}_\odot]$	1.10	1.10	1.10	1.10
$d_c[a_{orb}]$	0.100	0.110	0.102	0.084	$\mathcal{R}_h[R_\odot]$	3.65	3.64	3.65	3.65
a_T	4.3	6.5	5.9	5.1	$\mathcal{R}_c[R_\odot]$	7.75	7.75	7.75	7.75
F_h	0.242	0.242	0.242	0.242	$\log g_h$	4.06	4.06	4.06	4.06
T_h[K]	14000	14000	14000	14000	$\log g_c$	2.70	2.70	2.70	2.70
T_c[K]	4930	4980	4910	4950	M^h_{bol}	−1.87	−1.86	−1.87	−1.87
$A_{hs} = T_{hs}/T_d$	1.63	1.70	1.14	1.71	M^c_{bol}	1.03	0.99	1.04	1.01
$\theta_{hs}[^\circ]$	19.4	19.1	14.8	23.0	$a_{orb}[R_\odot]$	30.91	30.91	30.91	30.91
$\lambda_{hs}[^\circ]$	348.6	349.2	340.5	341.6	$\mathcal{R}_d[R_\odot]$	15.28	15.40	11.20	7.49
$\theta_{rad}[^\circ]$	−1.0	−3.6	8.3	2.4	$d_e[R_\odot]$	1.36	1.06	2.53	0.95

FIXED PARAMETERS: $q = \mathcal{M}_c/\mathcal{M}_h = 0.20$ - mass ratio of the components, $T_c = 14000$K - temperature of the less-massive (cooler) donor, $F_c = 1.0$ - filling factor for the critical Roche lobe of the donor, $f_h = 1.0; f_c = 1.00$ - non-synchronous rotation coefficients of the gainer and donor respectively, $\beta_h = 0.25; \beta_c = 0.08$ - gravity-darkening coefficients of the gainer and donor, $A_h = 1.0; A_c = 0.5; A_d = 1.0$ - albedo coefficients of the gainer, donor and disc. Quantities: n - number of observations, $\Sigma(O-C)^2$ - final sum of squares of residuals between observed (LCO) and synthetic (LCC) light-curves, σ_{rms} - root-mean-square of the residuals, i - orbit inclination (in arc degrees), $F_d = R_d/R_{yc}$ - disc dimension factor (ratio of the disc radius to the critical Roche lobe radius along y-axis), T_d - disc-edge temperature, d_e, d_c, - disc thicknesses (at the edge and at the center of the disc, respectively) in the units of the distance between the components, a_T - disc temperature distribution coefficient, $F_h = R_h/R_{zc}$ - filling factor for the critical Roche lobe of the hotter, more-massive gainer (ratio of the stellar polar radius to the critical Roche lobe radius along z-axis), T_h - temperature of the more-massive (hotter) gainer, $A_{hs,bs} = T_{hs,bs}/T_d$ - hot and bright spots' temperature coefficients, $\theta_{hs,bs}$ and $\lambda_{hs,bs}$ - spots' angular dimensions and longitudes (in arc degrees), θ_{rad} - angle between the line perpendicular to the local disc edge surface and the direction of the hot-spot maximum radiation, $\Omega_{h,c}$ - dimensionless surface potentials of the hotter gainer and cooler donor, $\mathcal{M}_{h,c}[\mathcal{M}_\odot]$, $\mathcal{R}_{h,c}[R_\odot]$ - stellar masses and mean radii of stars in solar units, $\log g_{h,c}$ - logarithm (base 10) of the system component, effective gravity, $M^{h,c}_{bol}$ - absolute stellar bolometric magnitudes, a_{orb} $[R_\odot]$, $\mathcal{R}_d[R_\odot]$, $d_e[R_\odot]$, $d_c[R_\odot]$ - orbital semi-major axis, disc radius and disc thicknesses at its edge and center, respectively, given in the solar radius units.

4

Evidence for cyclic mass transfer in the β-Lyrae-type binary OGLE-BLG-ECL-157529

This chapter is in preparation (in prep.) to be published by Mennickent, Garcés, Djurašević et al.

4.1 Abstract

The subtype of hot Algol binaries dubbed Double Periodic Variables (DPVs) are characterized by a photometric cycle longer than the orbital one, whose nature has been related to a magnetic dynamo operating in the mass-transferring component of the semidetached binary. Based on a photometric analysis of 18.5 years of OGLE data, we show that OGLE-BLG-ECL-157529 is a new eclipsing Galactic DPV of orbital period 24.8 days, and that its long-cycle length decreases from 918 to 709 days. In addition, we notice important changes in the morphology of the light curve linked to the phase of the long-cycle. Remarkably, the primary and secondary eclipses reverse its relative depth at some epochs. We show that the shape of the orbital light curves can be reproduced considering an accretion disc of variable thickness, temperature and radius, surrounding the hotter stellar component. We model the light curves at different epochs and phases of the long-cycle and find that the accretion disc always becomes thicker and colder at the minimum of the long-cycle, while at maximum it always becomes thinner and hotter. We also find evidence for two active regions, one of them near the place where the stream hits the disc. We discuss the evolutionary stage of the system finding the best match with one of the evolutionary models of Van Rensbergen et al. According to this model, the system is found in the phase of rapid mass transfer with

$\dot{M} \sim 10^{-6}$ $M_\odot$/yr, a figure that is confirmed when comparing the system with β Lyrae. The absence of orbital period change might be explained by non-conservative mass transfer. The data are consistent with cyclic changes of mass transfer rate following the long-cycle luminosity, in agreement with predictions of the dynamo model for the long cycle proposed by Schleicher & Mennickent (2017).

4.2 Introduction

Double Periodic variables (DPVs) are a subset of Algol-type binary systems.They consist of a red giant that has filled its Roche lobe and transfers material through an optically thick accretion disc onto a B-type dwarf. Its main characteristic is that they have two photometric cycles. A short period P_o, whose light curve shape is typical of the orbital modulation in eclipsing or ellipsoidal binaries and a long-cycle of cycle length P_l, whose origin is still unknown. On average, both periodicities are related through the relationship $P_l = 33 \times P_o$, but this relationship may vary for particular cases (Mennickent et al., 2003, 2016; Poleski et al., 2010; Pawlak et al., 2013; Mennickent et al., 2016; Mennickent, 2017). In some systems, a decrease in the long period has been reported, as in the case of OGLE-LMC-DPV-065 (Poleski et al., 2010; Mennickent et al., 2019) and OGLE-LMC-DPV-056 (Mennickent et al., 2008).

A magnetic origin has been proposed for the origin of the long-cycle (Schleicher & Mennickent, 2017). The rapid rotation of a synchronized donor star, added to the convective motions would cause it to have a magnetic dynamo, which would change the equatorial stellar radius as indicated by the Applegate's mechanism (Applegate, 1992) which should modulate the mass transfer through the inner Lagrangian point that could be observed as cyclic changes in luminosity evidenced in the long-cycle. His model, proposed by Schleicher & Mennickent (2017), predicts the correlation between the orbital and long period and also the value of the long-cycle length for particular systems with relatively good accuracy; for the seven studied binaries with orbital periods between five and 13 days, the maximum deviation between predicted and observed ratio is 30%, with the average deviation of order 12%. Actually, it has been shown that rapid rotation favor the operation of the Applegate's mechanism (Navarrete et al., 2018). If the long-cycle reflects changes in the mass transfer rate, we might expect changes in disc properties too, since the disc interacts with the gas stream. Recently, emission lines that are signatures of chromospherically active stars

were detected in V 393 Scorpii, supporting the existence of magnetically active donors in DPVs (Mennickent et al., 2018).

In this context, it is relevant that recently, significant changes have been detected in the morphology of the light curve of OGLE-LMC-DPV-097 that are directly related to the long-cycle (Garcés L. et al., 2018). These authors show that these changes would be due to possible physical changes of an accretion disc, which would change its diameter and thickness cyclically according to the phase of the long-cycle in which it is found.

In this study we show the photometric analysis of a Galactic DPV binary system that presents a variable long-cycle, viz. OGLE-BLG-ECL-157529 (α_{2000}=17:53:08.33, δ_{2000}=-32:46:27.0, I = 13.035, V = 14.829, Soszyński et al. (2016)). It is the first DPV reported in the direction of the Galactic Bulge. The GAIA identification is 4043437999622564608 and its parallax is 0.33065 ± 0.04436 mas, implying a distance of 3024 ± 406 pc (Gaia Collaboration et al., 2016, 2018). This indicate that the systems is not properly a member of the Galactic Bulge, but a projected disc member.

The good temporary coverage available for this target in the OGLE database, has allowed us to analyze it in a unique way. We find important changes in the morphology of the light curve that, similarly to OGLE-LMC-DPV-097, are related to the long-cycle.

Our motivation is to investigate the physical phenomena that give rise to its peculiar photometry, in order to understand its behavior. This object, together with other DPVs that show an unusual behavior, could be fundamental to understand the DPV phenomenon and test the hypothesis of magnetic cycles.

Table 4.1 Summary of photometric observations. The number of measurements, starting and ending times, and average magnitude are given. HJD zero-point is 2450000. Single point uncertainties are between 4 and 6 mmag

Data Base	N	HJD_{start}	HJD_{end}	Mag	Band
OGLE-II	346	551.77073	1858.52147	13.213	I
OGLE-III	795	2117.76494	4955.73490	13.221	I
OGLE-IV	1465	5261.84891	7332.50545	13.213	I

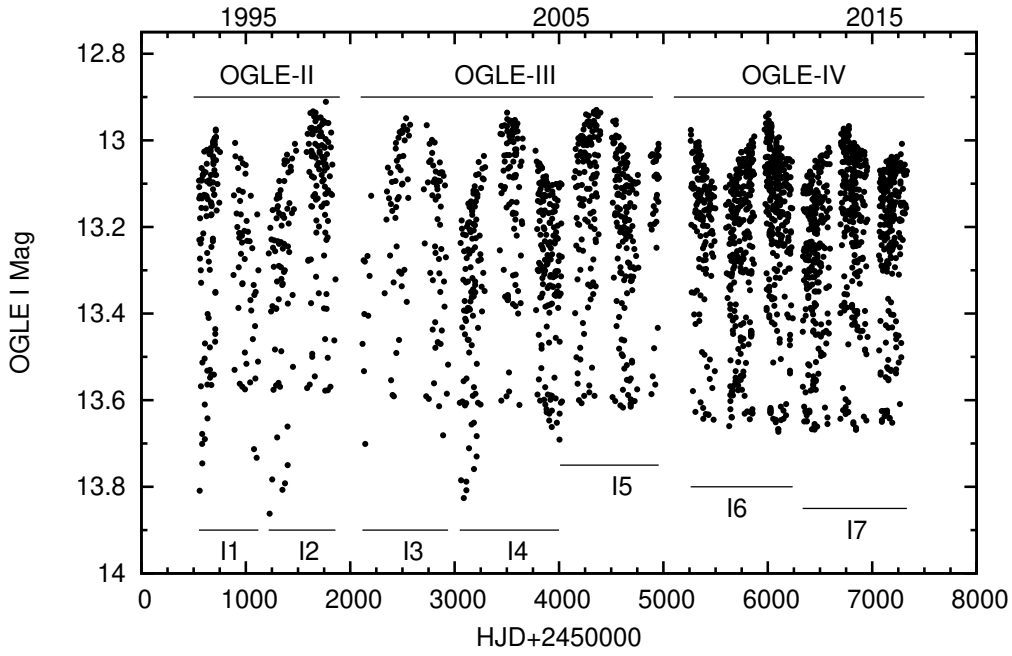

Figure 4.1 Photometry without pre-whitening available in the OGLE II-III-IV campaigns for the OGLE-BLG-ECL-157529 system. The intervals show the sections into which we divide the total sample (Table 4.2).

4.3 Photometric Data

This object is part of the catalogue of eclipsing binaries in the Galactic Bulge presented by Soszyński et al. (2016). The photometric time series analyzed in this study consists of 2606 *I*-band magnitudes taken from the following data bases (Fig. 4.1): OGLE-II (Szymanski, 2005)[1] and OGLE-III/IV[2]. The OGLE-IV project is described by Udalski et al. (2015). The whole data set, summarized in Table 4.1, spans a time interval of 6781 d, i.e. 18.5 yr.

4.4 Light curve disentangling

Analyzing the photometry of the different OGLE campaigns we note the following. The maximum magnitude in band I varies from 13 to 12.9 mag. The minimum magnitude presents a greater variation, 13.9 to 13.6 approximately (Fig. 4.1). We notice that these changes occurs through all years of observations. We will show that these variations in the maximum and minimum

[1] http://ogledb.astrouw.edu.pl/~ogle/photdb/
[2] OGLE-III/IV data kindly provided by the OGLE team.

Table 4.2 Time intervals and long-cycle lengths. The last column gives the epoch calculated using the trial period 910 days.

Interval	Long Period [d]	Epoch max. P_l [d]	Cycle	E
I1	871.16 ± 15.24	793.74 ± 27.08	0	793.74
I2	871.16 ± 15.23	1695.65 ± 30.09	1	1664.91
I3	859.99 ± 5.35	2681.64 ± 36.09	2	2536.07
I4	859.99 ± 5.35	3538.77 ± 22.60	3	3407.24
I5	859.99 ± 5.35	4396.57 ± 20.05	4	4278.41
I6	766.91 ± 4.36	5961.93 ± 23.37	6	6020.74
I7	766.91 ± 4.36	6737.98 ± 21.56	7	6891.91

magnitudes are due to the presence of the long-cycle. Actually, a careful inspection of the light curve reveals eclipses every few days simultaneously occurring with a high-amplitude long-cycle of cycle length of the order of hundreds of days.

To obtain both orbital and long-cycle light curves separately, we used the Fourier-based disentangling code described by Mennickent et al. (2012a). Before that, and previewing a variable long-cycle, we separated our data by OGLE campaigns to carry out a better analysis.

We used the generalized Lomb-Scargle (GLS) periodogram to obtain the main frequencies in our data. It was introduced by Zechmeister & Kürster (2009), and uses the principle of the Lomb (1976) and Scargle (1982) periodogram with some modifications, such as adding a displacement in the adjustment of the wave function and considering measurement errors. Compared with the classical periodogram, this gives us more accurate frequencies and a better determination of the intensity, being also not susceptible to aliases. We obtained the following ephemeris for the long-cycle at the different campaigns OGLE-II-III-IV, respectively:

$$\mathrm{HJD} = (793^{\mathrm{d}}.74 \pm 27^{\mathrm{d}}.08) + (871^{\mathrm{d}}.17 \pm 15^{\mathrm{d}}.24) \times \mathrm{E} \quad (4.1)$$

$$\mathrm{HJD} = (2681^{\mathrm{d}}.64 \pm 36^{\mathrm{d}}.09) + (859^{\mathrm{d}}.99 \pm 5^{\mathrm{d}}.35) \times \mathrm{E} \quad (4.2)$$

$$\mathrm{HJD} = (5961^{\mathrm{d}}.93 \pm 23^{\mathrm{d}}.37) + (766^{\mathrm{d}}.91 \pm 4^{\mathrm{d}}.36) \times \mathrm{E} \quad (4.3)$$

These data already show that the long-cycle decreases during the observing epoch. In order to quantify better this phenomenon, we measured the times of maximum at the intervals described in Table 4.2 and compared then with a trial period of 918^{d}. The observed minus calculated times are shown in Fig. 4.2, showing much clearly that after about 2700 days of constancy at about 918

days, the cycle length decreased to a new value of around 709 days.

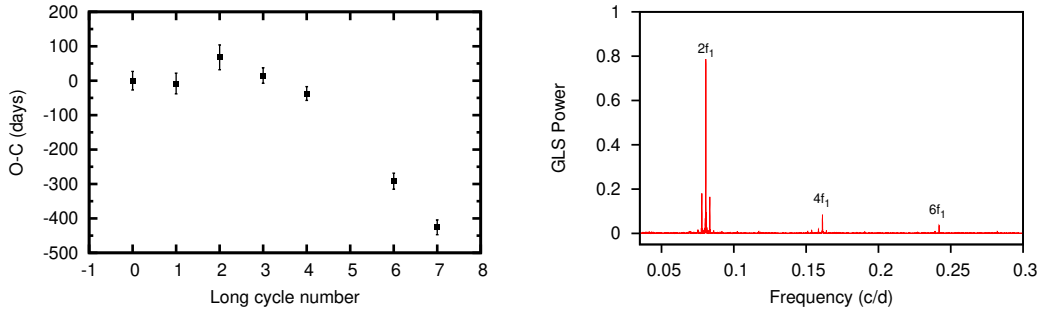

Figure 4.2 Left: Up: Observed (O) minus calculated (C) times of long-cycle maximum vs integer cycle number from Eq. 4.1 Right: Periodogram of the light curve after removing the long-cycle. The main peak is at $f = 0.040323953$ d^{-1} ($24^d.7991558$).

After removing the long cycle in every data interval, we examined the remaining orbital light curve. We find that the light curve can be described with the following ephemeris (Fig. 4.4):

$$\text{HJD} = (6695^{\text{d}}.756 \pm 0^{\text{d}}.058) + (24^{\text{d}}.799156 \pm 0^{\text{d}}.002368)\text{E} \quad (4.4)$$

The disentangling reveals an orbital light curve of β-Lyr type, i.e. with rounded shoulders between eclipses, a proximity effect typical in close binaries, where at least one of the components is tidally distorted and far from a spherical shape. Examples of orbital light curves are given later in this work. We notice that during the 18.5 years of observations the system maintains its orbital period constant. In spite of this, in the photometry an unusual behavior is observed. For a better analysis it was necessary to divide our data in relation to the phase of the long cycle in which they are, ascending (Asc $0.65 \leq \Phi_l \leq 0.9$), maximum (Max $0.9 \leq \Phi_l \leq 1.1$), descending (Des $0.1 \leq \Phi_l \leq 0.45$), minimum (Min $0.45 \leq \Phi_l \leq 0.65$). This is how we notice considerable changes in the depths of the primary and secondary minimum of the orbital light curve. These changes are more significant in the first data set (OGLE-II), during the 2450750-2543000 HJD epochs, and as the long period decreases they tend to be of smaller amplitude (Fig. 4.3).

Remarkably, both the primary and secondary minimum variations vary according to the long-cycle and with totally opposite behavior. Around the orbital phase corresponding to the primary eclipse ($\Phi_o = 0.0$) we notice that the greatest depth occurs when the system is at the maximum

of the long-cycle and the lowest depth when the system is during the minimum. On the other hand, around the orbital phase corresponding to the secondary eclipse (Φ_o = 0.5), we observe an opposite behavior, the larger depths are reached during the minimum phase of the long-cycle, while the smaller ones during the maximum phase. All these changes are more evident in Fig. 4.4, showing the changes of the orbital light curve with the long-cycle.

It is necessary to emphasize that during the observational period HJD 2450750−2543000 the primary and secondary minima have reversed as the long-cycle advances. During the minimum phase the primary minimum occurs at Φ_o = 0.5, while during the maximum phase the primary minimum occurs at Φ_o = 0 or Φ_o = 1. Despite this, during all years of observations and in all OGLE campaigns, it is observed that in the maximum phase of the long-cycle the primary minimum reaches its greatest depth and the secondary minimum the lowest depth. In addition, the morphology of the orbital curve remains unchanged in this phase of the long-cycle. We also observe a slight difference between the maxima of the first (Φ_o = 0.25) and second quadrature (Φ_o= 0.75). This is more significant in the first observations (OGLE-II) and when the system is in the maximum phase of the long-cycle (Fig. 4.4).

Another interesting feature is the double slope observed in the entrance and departure of the main eclipse, which we attribute to the presence of the accretion disc around the primary.

4.5 Light curve model

In order to model the observed light curves, we use a theoretical code developed by Djurašević (1992a,b) that considers a system consistent of a secondary star and a primary star surrounded by an accretion disc, that is both optically as geometrically thick. The disc edge is approximated by a cylindrical surface. The thickness of the disc can change linearly with radial distance, allowing the disc to take a conical shape (convex, concave, or plane-parallel). The geometrical properties of the disc are determined by its radius ($\mathcal{R}_d$), its thickness at the edge (d_e), and the thickness at the centre (d_c). The cylindrical edge of the disc is characterized by its temperature (T_d), and the conical surface of the disc by a radial temperature profile that follows a modified version of the temperature distribution proposed by Zola (1991) (Eq. 2.7).

We assume that the disc is in physical and thermal contact with the gainer, so the inner radius and temperature of the disc at this position are equal to the temperature (T_h) and radius ($\mathcal{R}_h$) of the

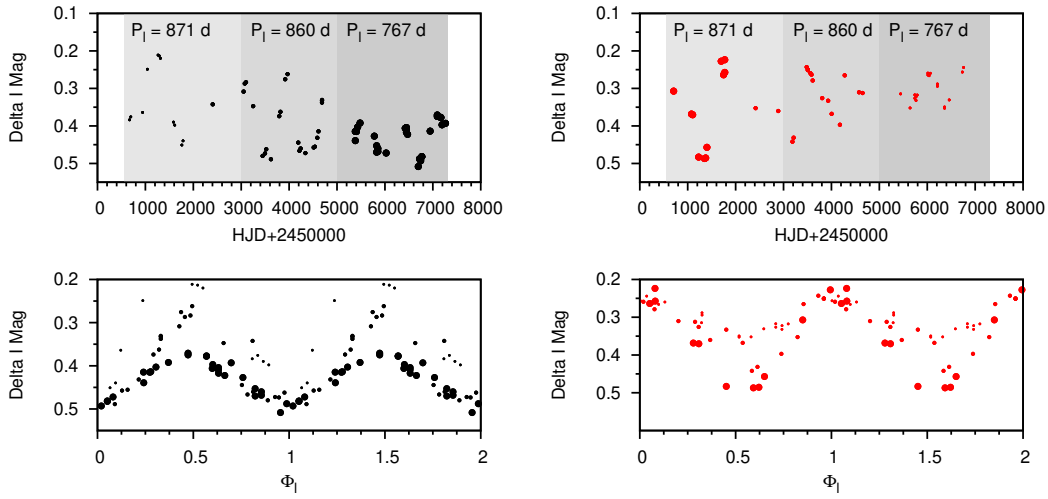

Figure 4.3 Diagrams showing the depth's variability of the primary and secondary eclipses in the disentangled orbital light curve. Red, green and blue dots refers to OGLE II, III and IV databases. Up: primary (left) and secondary (right) minima at different OGLE campaigns. Bottom: magnitude of primary (left) and secondary (right) minima versus long phase.

star. The temperature of the disc at the edge (T_d) and the temperature exponent (a_T), as well as the radii of the star ($\mathcal{R}_h$) and of the disc ($\mathcal{R}_d$) are free parameters, determined by solving the inverse problem.

Following previous research on DPVs (Mennickent et al., 2016), our model includes active regions on the edge of the disc. These active regions have been detected in Doppler maps of accretion discs in some Algol-type binaries (Richards, 2004). These regions are locally hotter than the disc, and produce a non-uniform distribution of radiation. We consider two active regions: a hot-spot (h_s) and a bright-spot (b_s), characterized by their temperatures $T_{hs,bs}$, angular dimensions (radius) $\theta_{hs,bs}$ and longitudes $\lambda_{hs,bs}$. The angular measurement λ is measured in the orbital plane, from the line joining the gainer and donor centers in the direction opposite to the orbital motion. These active-region parameters are also found by solving the inverse problem. We consider a possible departure of symmetry of light emerging from the hot-spot due, for instance, to the impact of the gas stream in the disc. This deviation is measured by the angle θ_{rad} between the line perpendicular to the local disc edge surface and the direction of the hot spot maximum radiation in the orbital plane. The second spot in the model (here named bright-spot), mimics the spiral structure of the accretion disc, observed in hydrodynamical calculations (Heemskerk, 1994). Tidal

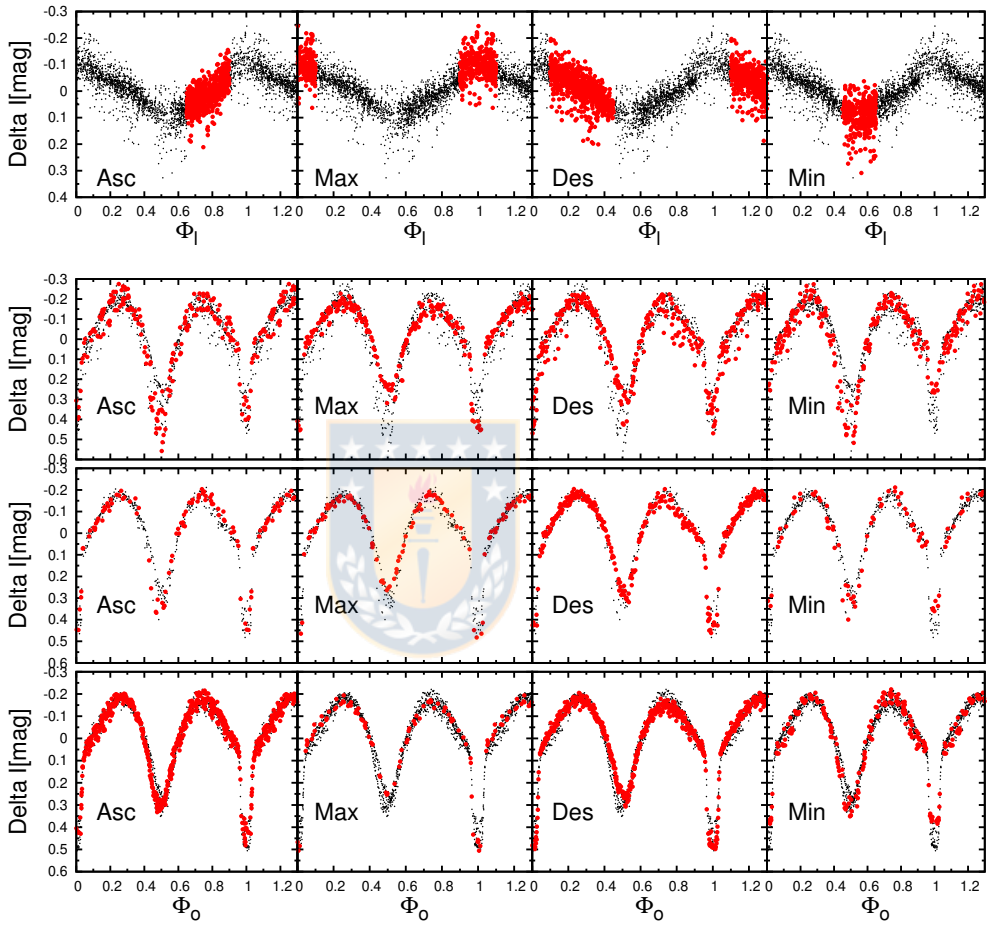

Figure 4.4 Up: Consolidated long-cycle light curves obtained with Eq. 4.1, 4.2 and 4.3, showing ascending, maximum, descending and minimum branches. Down: Orbital light curves in different stages of the long-cycle (Asc, Max, Des, Min) for the OGLE-II-III-IV campaigns, up, middle, bottom, respectively.

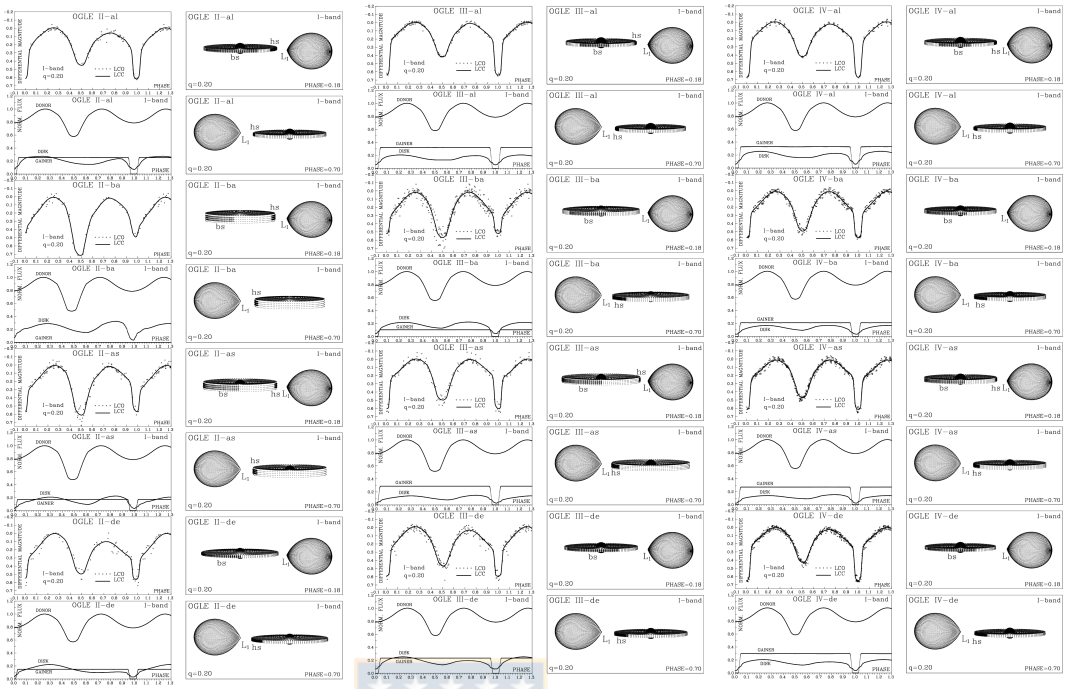

Figure 4.5 Left: Orbital light curve models for OGLE II data at the high stage (al), low stage (ba), ascending branch (as) and descending branch (de) of the long-cycle. Right: Orbital light curve models for OGLE III data at the high stage (al), low stage (ba), ascending branch (as) and descending branch (de) of the long-cycle.

forces exerted by the cool star produce a spiral shock, revealed in one or two extended spiral arms in the external border of the disc. This bright spot might also be interpreted as a disc region significantly deviating from a circular shape.

We should keep in mind two potential limitations of the code: the donor irradiation by the hot-spot is not included, neither a possible, not eclipsed, additional third light (considering that the long-cycle light was already removed with the light curve disentangling). However, the good light-curve fits (based on χ^2 minimization) suggests that these additional light sources, if present, are much fainter than the stars and the disc/spots. In addition, while hot-spot irradiation on the donor is not included, the much larger effect of the gainer irradiation on the donor is implemented in our code.

Because we do not have spectroscopic data for our object we do some approximations adequate for the theoretical model. Using the OGLE IV photometry and the disentangled orbital

light curve, we obtain a V − I = 0.65 color index in the primary minimum. For this reason we assume that the donor star has a spectral type F 5 and effective temperature of T_d = 6650 K (Cox, 2000b). We do not use the color index of the secondary eclipse (V − I = -0.17) because it could be contaminated by the accretion disc. By the way, outside eclipses we observe V − I ≈ -0.01. Here we notice that a color based on the OGLE mean magnitudes cannot be trusted because is based on an average of magnitudes including the orbital *and* long cycle. Disentangled fluxes are fundamental to get reliable colors for the stars. In addition, we assume synchronous rotation for the stellar components of this close binary and a mass ratio q = 0.2. We consider this parameter representative of DPVs, since previous studies of the DPV population show $\overline{q}$ = 0.23 ± 0.05 (std) for 8 cases including β Lyrae (Mennickent et al., 2016). With these approximations we expect to get qualitative insights on the nature of the system variations, rather than precise stellar and system parameters. All system parameters are determined by solving the inverse problem as described by Djurašević (1992a); they are summarized in Table 4.3. A direct comparison of our theoretical models and observations is given in Fig. 4.5.

4.5.1 The best fit to light curve

We find that the system contains a pair of stars of 7.26 $M_\odot$ and 1.45 $M_\odot$, radii 4.93 $R_\odot$ and 18.44 $R_\odot$, temperatures T_h = 18734 K and T_c = 6650 K, absolute magnitudes M_{bol} = -3.79 and -2.15, separated by 73.6 $R_\odot$. The above values are averages when variable in Table 4.3 These parameters must be taken with caution, since we have assumed a mass ratio for the system, and the donor temperature was obtained from the color during main eclipse. However, these assumption allows to study the changes occurring during the long-cycle with some confidence. We notice that these parameters should produce a long-cycle of about 33.13 times the orbital period, i.e. 821.6 days, according to the model proposed by Schleicher & Mennickent (2017), that is close to the average of the observed range, viz., 813.5 days.

The theoretical fit to our light curves for the different OGLE campaigns allows us to understand what phenomena are producing the observed photometry. This is how we noticed that the different morphologies of the light curves are due to major changes in the thickness of the disc.

We notice that the disc reaches its highest central thickness always when the system is at the

Table 4.3 Results of the analysis of OGLE II,III,IV light-curves obtained by solving the inverse problem for the Roche model with an accretion disc around the more-massive (hotter) component. Roman numbers refer to OGLE campaigns and arabic numbers to high stage (1), low stage (2), ascending branch (3) and descending branch (4). Last column gives average errors.

Quantity	II – 1	II – 2	II – 3	II – 4	III – 1	III – 2	III – 3	III – 4	IV – 1	IV – 2	IV – 3	IV – 4	error
n	92	56	132	70	147	298	148	206	150	336	462	521	
$\Sigma(O-C)^2$	0.0481	0.0464	0.1662	0.1692	0.0440	0.8196	0.1853	0.3120	0.0386	0.2875	0.2646	0.2313	
$\sigma_{\rm rms}$	0.0230	0.0290	0.0356	0.0249	0.0174	0.0525	0.0355	0.0390	0.0161	0.0293	0.0240	0.0211	
$i[^\circ]$	85.44	85.40	85.20	85.13	85.43	85.45	85.44	85.38	85.41	85.49	85.37	85.42	0.25
F_d	0.876	0.839	0.881	0.922	0.846	0.926	0.937	0.879	0.868	0.868	0.874	0.855	0.03
T_d[K]	4550	3670	3460	3675	4450	3980	3325	4380	4270	3954	3591	3550	100
$d_e[a_{\rm orb}]$	0.040	0.095	0.090	0.036	0.042	0.049	0.069	0.038	0.041	0.045	0.052	0.037	0.01
$d_c[a_{\rm orb}]$	0.030	0.141	0.046	0.070	0.004	0.082	0.006	0.041	0.004	0.041	0.015	0.017	0.01
a_T	5.2	6.9	6.3	6.5	5.2	6.3	6.1	6.3	3.5	6.8	5.0	3.5	0.5
F_h	0.138	0.137	0.138	0.137	0.138	0.137	0.137	0.138	0.139	0.136	0.137	0.138	0.002
T_h[K]	18750	18740	18630	18760	18760	18720	18820	18730	18740	18650	18760	18750	500
T_c[K]	6650	6650	6650	6650	6650	6650	6650	6550	6550	6650	6550	6650	100
$A_{hs} = T_{hs}/T_d$	1.67	1.81	1.78	1.20	1.63	1.78	1.66	1.66	1.59	1.78	1.65	1.80	0.1
$\theta_{hs}[^\circ]$	19.8	20.5	19.3	17.0	17.0	19.6	19.5	19.6	17.0	18.7	19.5	19.2	3.0
$\lambda_{hs}[^\circ]$	348.1	339.7	333.4	315.0	334.9	310.5	324.2	310.52	335.9	310.1	338.4	310.2	11.3
$\theta_{\rm rad}[^\circ]$	−15.8	−24.7	−25.7	−22.6	−29.4	−28.6	−22.8	−29.8	−29.4	−29.9	−30.0	−28.9	13
$A_{bs1} = T_{bs}/T_d$	1.52	1.58	1.51	1.81	1.57	1.58	1.43	1.61	1.68	1.51	1.39	1.73	0.1
$\theta_{bs}[^\circ]$	49.3	34.4	48.3	48.0	25.8	31.5	46.7	49.2	26.2	40.5	42.4	46.2	7.0
$\lambda_{bs}[^\circ]$	85.9	109.1	112.8	110.3	77.3	87.5	110.2	84.1	74.6	93.7	99.1	84.5	9.7
Ω_h	15.07	15.18	15.18	15.16	15.11	15.20	15.14	15.04	14.97	15.33	15.13	15.08	0.08
Ω_c	2.233	2.233	2.233	2.233	2.233	2.233	2.233	2.233	2.233	2.233	2.233	2.233	0.01
$\mathcal{M}_h[\mathcal{M}_\odot]$	7.26	7.26	7.26	7.26	7.26	7.26	7.26	7.26	7.26	7.26	7.26	7.26	0.1
$\mathcal{M}_c[\mathcal{M}_\odot]$	1.45	1.45	1.45	1.45	1.45	1.45	1.45	1.45	1.45	1.45	1.45	1.45	0.1
$\mathcal{R}_h[R_\odot]$	4.95	4.91	4.95	4.92	4.93	4.91	4.93	4.96	4.98	4.86	4.93	4.95	0.07
$\mathcal{R}_c[R_\odot]$	18.44	18.44	18.44	18.44	18.44	18.44	18.44	18.44	18.44	18.44	18.44	18.44	0.04
$\log g_h$	3.91	3.92	3.91	3.92	3.91	3.92	3.91	3.91	3.90	3.92	3.91	3.91	0.02
$\log g_c$	2.07	2.07	2.07	2.07	2.07	2.07	2.07	2.07	2.07	2.07	2.07	2.07	0.02
$M^h_{\rm bol}$	−3.80	−3.78	−3.77	−3.79	−3.79	−3.77	−3.80	−3.80	−3.81	−3.74	−3.79	−3.80	0.03
$M^c_{\rm bol}$	−2.15	−2.15	−2.15	−2.15	−2.15	−2.15	−2.15	−2.15	−2.15	−2.15	−2.15	−2.15	0.03
$a_{\rm orb}[R_\odot]$	73.57	73.57	73.57	73.57	73.57	73.57	73.57	73.57	73.57	73.57	73.57	73.57	0.9
$\mathcal{R}_d[R_\odot]$	34.14	32.69	34.34	35.94	32.99	36.08	36.52	34.26	33.82	33.83	34.05	33.32	0.6
$d_e[R_\odot]$	2.95	6.99	6.65	2.65	3.06	3.60	5.05	2.77	3.02	3.28	3.84	2.70	0.2
$d_c[R_\odot]$	2.22	10.40	3.38	5.15	0.32	6.07	0.42	3.00	0.29	3.03	1.11	1.21	0.3

FIXED PARAMETERS: $q = \mathcal{M}_c/\mathcal{M}_h = 0.20$ - mass ratio of the components, $T_c = 6550$K - temperature of the less-massive (cooler) donor,$F_c = 1.0$ - filling factor for the critical Roche lobe of the donor, $f_h = 1.0; f_c = 1.00$ - non-synchronous rotation coefficients of the gainer and donor respectively, $\beta_h = 0.25; \beta_c = 0.08$ - gravity-darkening coefficients of the gainer and donor, $A_h = 1.0; A_c = 0.5$ - albedo coefficients of the gainer and donor. Quantities: n - number of observations, $\Sigma(O-C)^2$ - final sum of squares of residuals between observed (LCO) and synthetic (LCC) light-curves, $\sigma_{\rm rms}$ - root-mean-square of the residuals, i - orbit inclination (in arc degrees), $F_d = R_d/R_{yc}$ - disc dimension factor (ratio of the disc radius to the critical Roche lobe radius along y-axis), T_d - disc-edge temperature, d_e, d_c, - disc thicknesses (at the edge and at the center of the disc, respectively) in the units of the distance between the components, a_T - disc temperature distribution coefficient, $F_h = R_h/R_{zc}$ - filling factor for the critical Roche lobe of the hotter, more-massive gainer (ratio of the stellar polar radius to the critical Roche lobe radius along z-axis), T_c - temperature of the less-massive (cooler) donor, $A_{hs,bs} = T_{hs,bs}/T_d$ - hot and bright spots' temperature coefficients, $\theta_{hs,bs}$ and $\lambda_{hs,bs}$ - spots' angular dimensions and longitudes (in arc degrees), $\theta_{\rm rad}$ - angle between the line perpendicular to the local disc edge surface and the direction of the hot-spot maximum radiation, $\Omega_{h,c}$ - dimensionless surface potentials of the hotter gainer and cooler donor, $\mathcal{M}_{h,c}[\mathcal{M}_\odot]$, $\mathcal{R}_{h,c}[R_\odot]$ - stellar masses and mean radii of stars in solar units, $\log g_{h,c}$ - logarithm (base 10) of the system components effective gravity, $M^{h,c}_{\rm bol}$ - absolute stellar bolometric magnitudes, $a_{\rm orb}$ $[R_\odot]$, $\mathcal{R}_d[R_\odot]$, $d_e[R_\odot]$, $d_c[R_\odot]$ - orbital semi-major axis, disc radius and disc thicknesses at its edge and center, respectively, given in the solar radius units.

minimum stage of the long-cycle, with a value of d_c 10.40, 6.07 and 3.03 $R_\odot$ in the OGLE-II-III-IV campaigns, respectively. We also notice that the lowest central thickness was always obtained in the maximum stage of the long-cycle, with a value of d_c 2.22, 0.32, 0.29 $R_\odot$ in the OGLE-II-III-IV campaigns, respectively. These changes in the thickness of the disc explain why the primary and secondary minimum are inverted during the first observational dates. During the minimum phase the disc would cover a large part of the gainer, thus hiding the brightest star and producing the minimum primary in the orbital phase $\Phi_o = 0.5$. During the high phase the accretion disc always has a smaller radius, returning to produce the minimum primary in the orbital phase $\Phi_o = 1$. As we saw, these changes in the disc diminish through the years of observation and for this reason we only see an inversion in the primary and secondary minimum during the first observational epochs.

We notice other changes in the accretion disc. The temperature of the disc varies from 4550 to 3325 K (variation of 1225 K), always reaching the highest temperature at the maximum stage of the long-cycle. The temperature coefficient of the hot-spot varies during the long-cycle from 1.20 to 1.81 in some cases and the temperature coefficient of the bright-spot presents a smaller variation of 1.39 to 1.81. Meanwhile, the angular size of the hot-spot θ_{hs} varies from 17°.0 to 20°.5, being located around the longitudes λ_{hs} 310°.1 - 348°.1. The angular size of the bright spot θ_{bs} varies from 25°.8 to 49°.3 and this spot moves between the longitudes λ_{bs} 77°.3 - 112°.8. The disc radius varies slightly during the long-cycle and through the years, changing between $\mathcal{R}_d$ 32.69-36.08 $R_\odot$ with an average of 34.3 ± 1.2 $R_\odot$. This means $R_d/a \approx 0.47$, i.e. the disc outer border is just below the tidal radius for the given mass ratio, in agreement with a non tidally perturbed disc (Paczynski, 1977; Warner, 1995).

Our model also provides the fractional light contribution at the *I*-band of donor, primary and disc through the orbital cycle (Fig. 4.5). The donor is the dominant source of light even when eclipsed, whereas only in occasions the disc flux is larger than the primary flux, especially when the primary becomes hidden by a thicker disc at the low stage covered by the OGLE I data.

4.5.2 Cyclic changes in mass transfer rates

In a semidetached binary ongoing Roche lobe overflow with mass transfer rate $\dot{M}_c$ the luminosity of the hotspot is (following Warner (1995), Eq. 2.21):

$$L_{hs} = \eta\tau G\frac{M_h\dot{M}_c}{R_d} \tag{4.5}$$

where the η factor (between 0 and 1) takes into account that since the stream impacts obliquely, only the velocity component perpendicular to the disc outer edge participates in the transformation to kinetic energy. τ is another factor that considers that the fall of material onto the disc is not from the infinity but from the inner Lagrangian point. G is the gravitational constant.

On the other hand, considering the hotspot radiating as a blackbody, its luminosity can be expressed as:

$$L_{hs} = \sigma T_{hs}^4 d_e l = \sigma [A_{hs} T_d]^4 d_e l \tag{4.6}$$

where l is a measure of the arc subtended by the hotspot along the outer disc edge:

$$l = R_d \theta_{hs} \tag{4.7}$$

Note that in absence of any measurement of the radial extension of the hotspot we have used its extension along the disc border. Hence, during two stages labeled as i (initial) and f (final), and considering constant η and τ, the mass transfer rate satisfies:

$$\frac{\dot{M}_{c,f}}{\dot{M}_{c,i}} = \frac{R_{d,f}^2 [A_{hs,f} T_{d,f}]^4 d_{e,f} \theta_{hs,f}}{R_{d,i}^2 [A_{hs,i} T_{d,i}]^4 d_{e,i} \theta_{hs,i}} \tag{4.8}$$

In Table 4.4 we give this ratio for the 12 epochs listed in Table 4.3. Due to error propagation, these ratios might be uncertain up to 45%, mainly due to the errors in d_e and θ_{hs}. We notice, however, that systematic errors should be canceled during the quotient and the true errors should be less than the aforementioned figure. In spite of these uncertainties, it is clear that changes in mass transfer rate are observed. The following two results are tentatively rised: (i) the maximum $\dot{M}$ occurs during the low stage of the long-cycle, this is seen independently with the OGLE II, III and IV data, although the net value seems to decrease during the whole observing window, and (ii) the system is less active in this sense during the epoch of OGLE IV and more active during the epoch of OGLE II. The eclipse depth reversal reported previously occurs when the disc is thicker, attaining a vertical thickness of 7 solar radii at the outer edge and 10.4 solar radii at the central border. In other words, during some epochs the eclipse occults a large fraction of the gainer reducing its contribution to the total system flux, hence decreasing the depth of the corresponding eclipse. In addition, the variability seems to follow a well-defined pattern; the luminosity of the

Table 4.4 The mass transfer rate $\dot{M}_c$ calculated from Eq. 4.8 at different long-cycle epochs normalized to the value at the descending branch of OGLE II data. We also show the data used in the process. The last two lines show the comparison with β Lyrae. In this case the mass transfer rates is normalized to the β Lyrae figure, which is indicated with asterisks.

$\mathcal{R}_d[R_\odot]$	A_{hs}	$T_d[K]$	$d_e[R_\odot]$	$\theta_{hs}[^\circ]$	$\dot{M}_c/\dot{M}_c*$	source	epoch
34.14	1.67	4550	2.95	19.8	10.83	OGLE II	high
35.94	1.20	3675	2.65	17.0	1.00	OGLE II	descending
32.69	1.81	3670	6.99	20.5	14.90	OGLE II	low
34.34	1.78	3460	6.65	19.3	10.32	OGLE II	ascending
32.99	1.63	4450	3.06	17.0	7.84	OGLE III	high
34.26	1.66	4380	2.77	19.6	8.57	OGLE III	descending
36.08	1.78	3980	3.60	19.6	10.49	OGLE III	low
36.52	1.66	3325	5.05	19.5	5.48	OGLE III	ascending
33.82	1.59	4270	3.03	17.0	6.02	OGLE IV	high
33.32	1.80	3550	2.70	19.2	4.74	OGLE IV	descending
33.83	1.78	3954	3.28	18.7	8.40	OGLE IV	low
34.05	1.65	3591	3.84	19.5	5.12	OGLE IV	ascending
34.3	1.67	3904	3.88	18.9	0.11*	OGLE	average
28.3	1.21	8200	11.2	16.2	1*	external	β Lyr

putative hotspot wind (labeled "high", "descending", "low", "ascending") follows the changes in mass transfer rate with certain delay. The system luminosity attains its maximum level ("high" state) after the maximum of the mass transfer rate (which occurs at "low" state) and when this has started to decrease. It is then possible that the long-cycle represents changes in hotspot-wind luminosity, following changes in mass transfer rate in this system.

The absolute value of the mass transfer rate can be estimated using Eq. 4.8 and the famous system β Lyrae as a reference, whose mass transfer rate has been calculated as 1.58×10^{-5} $M_\odot$/yr by Mennickent & Djurašević (2013) and 2.57×10^{-5} $M_\odot$/yr by De Greve & Linnell (1994). Using the model for the β Lyrae accretion disc by Mennickent & Djurašević (2013) we derive for OGLE-BLG-ECL-157529 1.75×10^{-6} $M_\odot$/yr or alternatively 2.84×10^{-6} $M_\odot$/yr.

4.5.3 On the evolutionary stage

To answer the question about the evolutionary stage of OGLE-BLG-ECL-157529 we follow Mennickent et al. (2012a). We compared the system parameters obtained with the light-curve fitting method, with those predicted by the binary evolution models by van Rensbergen et al. (2008) available at the Center de Données Stellaires (CDS). In total we inspected the 561 conservative and non-conservative evolutionary tracks. A fit was made with the synthetic ($S_{i,j,k}$) and observed (O_k) stellar parameters mass, temperature, luminosity and radii, and the orbital period, where i (from 1 to 561) indicates the synthetic model, j the time t_j and k (from 1 to 9) the stellar or orbital parameter. Non-adjusted parameters were Roche lobe radii, mass loss rate, age, chemical composition and fraction of accreted mass lost by the system. For every model i we calculated a $\chi^2_{i,j}$ parameter at every t_j defined by:

$$\chi^2_{i,j} \equiv (1/N)\Sigma_k w_k[(S_{i,j,k} - O_k)/O_k]^2 \tag{4.9}$$

where N is the number of observations (9) and w_k the statistical weight of the parameter O_k, calculated as:

$$w_k = \sqrt{O_k/\epsilon(O_k)} \tag{4.10}$$

where $\epsilon(O_k)$ is the error associated to the observable O_k. The model minimizing χ^2 represents the best evolutionary history of the system.

We find the absolute χ^2 minimum (viz. 0.0229) in the strong-tidal interaction model with initial masses of 5.0 and 4.5 $M_\odot$ and initial orbital period of 3.5 days; their parameters are shown in Table 4.5. Other models showed significantly larger χ^2 therefore they were discarded as possible solutions for the system. The corresponding evolutionary tracks for the gainer and donor stars are shown in Fig. 4.6, along with the position for the best model. We observe a relatively good match for the donor but a small mismatch with the gainer that results a bit under-luminous. We should keep in mind that the resolution of the grid of synthetic models imposes basic restrictions to this kind of analysis.

The best fit indicates that OGLE-BLG-ECL-157529 is found inside a burst of mass transfer. The donor is an inflated R_c = 18.39 $R_\odot$ and 1.455 $M_\odot$ giant with its core completely exhausted

Table 4.5 The parameters of the Van Rensbergen et al. (2008) model that best fit the system parameters. The hydrogen and helium core mass fractions (X_c and Y_c) are given for the cool and hot star.

age (yr)	1.13E8
M_c ($M_\odot$)	1.455
M_h ($M_\odot$)	8.045
$\dot{M}_c$ ($M_\odot$ yr^{-1})	-2.53E-6
log T_c (K)	3.793
log T_h (K)	4.312
log L_c ($L_\odot$)	2.658
log L_h ($L_\odot$)	3.626
R_c ($R_\odot$)	18.391
R_h ($R_\odot$)	5.155
X_{cc}	0.00
Y_{cc}	0.98
P_o (d)	24.827

of hydrogen. The gainer is a 8.045 $M_\odot$ dwarf so almost no mass has been lost from the system. According to the best model the system has now an age of 1.13×10^8 yr and $\dot{M} = 2.53 \times 10^{-6}$ $M_\odot$ yr^{-1}. This figure for $\dot{M}$ is very close to the value derived in Section 4.5.2.

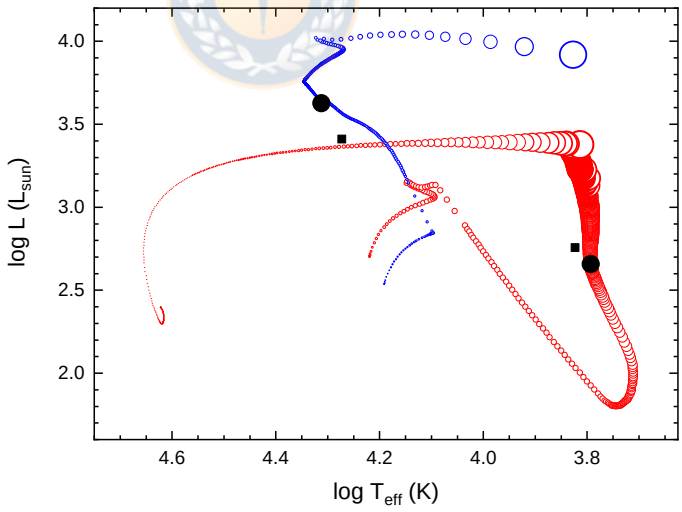

Figure 4.6 Evolutionary tracks for the binary star model from Rensbergen et al. (2008) that best fit the data. Donor (blue) and gainer (red) evolutionary paths are shown, along with the parameters derived from the light curve fit. The best fit is reached at the time corresponding to the data shown with big solid circles, that is model attached to the axis by dashed lines, that is characterized in Table 4.5. Stellar sizes are proportional to the circle diameters.

4.5.4 On the mass transfer rate and the disc

The error in the orbital period ϵ_P in ΔT =18.5 years implies a possible change in the orbital period of less than $2\epsilon_P/\Delta T$ = 1.30E-5 d/yr. For conservative mass transfer this imposes an upper limit for the mass transfer rate. The expected period change in the conservative case is (Huang, 1963):

$$\frac{\dot{P}_o}{P_o} = 3\dot{M}_c(\frac{1}{M_2} - \frac{1}{M_1}) \tag{4.11}$$

Using the aforementioned figures we determine $\dot{M}_c$ < 3.1E-7 $M_\odot$/yr. This is much lower than the value derived in the previous sections, indicating that: (i) the system is not conservative and Eq. 4.11 is therefore not valid or (ii) the value derived in the previous section is wrong (consider that in the case of models it is a parameter highly sensitive, i.e. changes rapidly during the mass transfer process).

We built the disc temperature profile with the average system parameters using Eq. 2.7, and compared with: (a) the disc temperature profile in case the disc is heated by radiation from the gainer at zero order approximation (Van Rensbergen & De Greve, 2016):

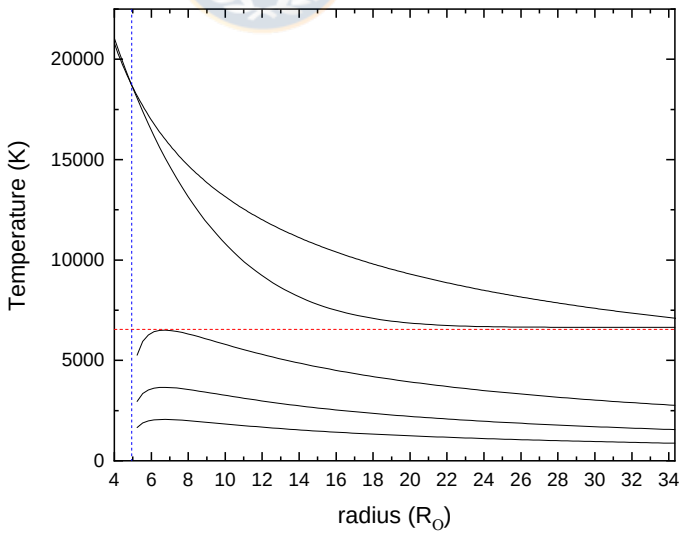

Figure 4.7 Disc temperature profiles. From top to down: profile given by Eq. 4.14, the profile obtained in this study with average parameters and the profiles given by Eq. 4.14 for $\dot{M}_c$ = 7.26E-5, 7.26E-6 and 7.26E-7, respectively. Vertical and horizontal dashed lines indicate gainer radius and donor temperature, respectively.

$$T_{disc,rad}(r) = T_h\Big(\frac{R_h}{r}\Big)^{0.5} \tag{4.12}$$

and (b) the disc temperature profile in case the disc in heated and radiates because of steady accretion of material onto the gainer (Bath & Pringle, 1981):

$$T_{disc,acc}(r)^4 = T^4_{disc*}\Big(\frac{R_h}{r}\Big)^3\Big(1 - \sqrt{\frac{R_h}{r}}\Big) \tag{4.13}$$

where the characteristic disc temperature is given by:

$$T_{disc*} = 478074\Big(\frac{M_h\dot{M}_c}{R^3_h}\Big)^{0.25} \tag{4.14}$$

and the masses and radii are in solar units and the mass transfer rate in $M_\odot$/yr. It is clear from Fig. 4.7 that the disc is mainly heated by radiation from the gainer and accretion plays a minor role in driving its luminosity, something noticed in other DPVs and algols with discs by Mennickent et al. (2016b) and Van Rensbergen & De Greve (2016).

4.6 Discussion

Recently a complete photometric analysis of the DPV OGLE-LMC-DPV-097 was presented by Garcés L. et al. (2018) who concluded that the differences in the orbital curves were due to changes mainly in the accretion disc structure and bright/hot spot temperatures. The accretion disc would be smaller (7.5 $R_\odot$) and hot at the minimum stage of the long-cycle and larger (15.3 $R_\odot$) and cold at the maximum stage of the long-cycle. Now we find a new DPV that also shows differences in its orbital light curve related to its long period and that are explained with changes mainly in the thickness of the disc. This would be thicker and colder during the minimum phase of the long-cycle, while thinner and hotter during the maximum phase of the long-cycle. Both objects show different light curves as they move through different stages of the long-cycle. According to our theoretical models for the light curves these would be linked to important changes in some

characteristics of the accretion disc and bring insights on the long-cycle driving mechanism.

As we know, all light sources in the orbital plane inside the binary orbit should be eclipsed. As the long-cycle light curve is not eclipsed in DPVs, its light source is probably located above or below the orbital plane. This was already noticed by different authors (e.g. Desmet et al., 2010; Mennickent et al., 2012b). On the other hand, it has been demonstrated that the hot-spot can drive a radiatively supported wind in some Algols (van Rensbergen et al., 2008, 2011). This idea, along with the Applegate's prediction of a change in quadrupole momentum in a magnetically active star (Applegate, 1992), yielded Schleicher & Mennickent (2017) to propose that the long-cycle is produced by the cyclic increase in mass transfer in DPVs. An increase in mass transfer rate should produce changes in hot-spot temperature and disc radius. Although the details of these changes should depend on the physics of the disc-stream interaction (i.e. disc/stream densities, angle of stream-disc impact), our findings are consistent with the predictions of the dynamo-model for DPVs. This conclusion is also applicable to OGLE-LMC-DPV-097 discussed by Garcés L. et al. (2018).

4.7 Conclusion

We find that the eclipsing binary OGLE-BLG-ECL-157529 present in the catalogue of Soszyński et al. (2016) is a Double Periodic Variable characterized by an orbital period of $24^{d}.7991558 \pm 0^{d}.0001203$ and a variable long cycle length decreasing from 918 to 709 days during 18.5 years of observations. In addition, the orbital light curve shows a complex behavior, changing its shape when the system moves at different phases of the long-cycle. These changes are more significant in the first epoch of observations, where even a reversal between the primary and secondary eclipse depth is observed. A theoretical model of the light curve including an accretion disc around the primary shows that the different orbital light curve shapes can be explained in terms of structural changes in the accretion disc. These changes are stable and repeat during at least eight long cycles and can be summarized as: the disc is thicker and colder in the minimum phase and thinner and hotter in the maximum phase of the long-cycle. Our model explains the reversal of the eclipse depths and the changes observed in the orbital light curve shape. The confirmation of a disc and hot and bright spots indicate a semidetached binary where the donor fills its Roche-lobe and transfer mass onto the primary through an accretion disc.

The source responsible for the long-cycle light curve is not identified in this study. However, the changes observed in the accretion disc and the spots are in principle consistent with the DPV hypothesis of a magnetic dynamo modulating the mass transfer through the inner Lagrangian point, as described by Schleicher & Mennickent (2017). In this model the light-source of the long-cycle is the wind emerging from the hot-spot created by the interaction of the gas stream and the disc. It is then plausible that variations in mass transfer rate produce changes in disc and hot/bright-spot properties as we observe in this interesting object. In this context is interesting to notice that β Lyrae also shows a long photometric cycle, a disc with hot spots and magnetic activity has been suggested (REF). Although no correlations between the light curve shape and the long-cycle have been reported for β Lyrae, is possible that the same driving mechanism is acting in both systems.

We have calculated the relative mass accretion rate at different epochs of the data and find significative cyclic variations. We find the absolute value of $\dot{M} \sim 10^{-6}$ M$\odot$/yr by comparing with the β Lyrae system, and the evolutive stage was determined finding the best match with the Van Rensbergen et al. models. Our results suggest that the system is ongoing a mass transfer event of considerable intensity and non-conservative process are present. In addition, the putative hotspot wind luminosity experiences a delay regarding the changes in mass transfer rate, since we observe the maximum of the long cycle when the mass accretion rate has started to decrease. The above results are compatible with the dynamo model proposed by Schleicher & Mennickent (2017).

5

An explanation for the reversal of the primary and secondary eclipses in the binary OGLE-BLG-ECL-253799

This chapter will be published with the contribution of Garcés, Mennickent, Djurašević.

5.1 Abstract

The OGLE database has allowed us to study in detail important changes in the morphology of the light curve of different binary systems. These unusual behaviors have not been widely studied and their analysis is essential to understand the physical mechanisms that produce them. We present a photometric analysis of the eclipsing binary OGLE-BLG-ECL-253799 based on OGLE-IV photometry spanning 5.5 years. We find significant changes in the morphology of the light curve, mainly in the depth and width of the secondary minimum, which becomes the deeper primary minimum at some epochs. We analyze this particular behavior by means of theoretical fits to the different observed light curves. The code used considers an optically and geometrically thick accretion disc around the primary star. We find that the observed changes in the light curve morphology might be due to changes in the physical structure of an accretion disc surrounding the hotter star. The larger variability can be explained in terms of changes of the vertical thickness and minor changes in the temperature and radius of the disc. Our model suggests that the system consists of a A-type dwarf orbiting an evolved M-type star every 37.6 days in a circular orbit, and

a disc of extension about 33 $R_{\odot}$. The reported changes can be explained by disc changes eventually produced by variable mass transfer in a semidetached binary. This unique system might be relevant in the study of dynamos in binaries with magnetically active components.

5.2 Introduction

Recently, analyses of light curves of binary systems with remarkably unique behaviors have been published. At Djurašević et al. (2012) a complete analysis of the V455 Cygni binary system is shown, that shows considerable variations in the shape of its light curve. The changes occur mainly in the primary and secondary minima, changing depth at different times of observation. By the morphology of the light curves it was believed that the components had a contact or overcontact configuration. However, the best theoretical fit is achieved including an optically and geometrically thick accretion disc. The variations observed in the shape of the light curve are mainly due to physical changes in the accretion disc, mainly in the radius and the characteristics of the active areas, located on the outer edge of the disc and considered in the model. At Zasche et al. (2017) inquire about the nature of depth changes in the primary minimum of the OGLE-SMC-ECL-0277 system, which, in addition to an orbital period of 60.37 days, shows an additional periodicity of 1500 days. In spite of checking hypotheses of pulsations, spots evolution or changes in the inclination angle, their results are, however, inconclusive to explain such unusual behaviour. They propose using a more sophisticated model that includes an accretion disc to explain what happens in this system. On the other hand, (Garcés L. et al., 2018) report changes in the orbital light curve of the OGLE-LMC-DPV-097 binary, which are directly related to the long cycle present in this Double Periodic Variable (DPV, Mennickent et al., 2003; Poleski et al., 2010; Pawlak et al., 2013; Mennickent et al., 2016; Mennickent, 2017). Similarly, a theoretical model that includes an accretion disc is applied to the light curves. The main cause of the morphology changes in the orbital light curve would be due to important changes in the accretion disc, mainly in its radius and temperature, in addition to the variations in the location, size and temperature characteristics of the Hot/Bright spot.

These systems seem to show a phenomenon associated with variable or transient mass transfer rates, which could produce variations in the characteristics of the accretion disc surrounding the donor star and also in the morphology of the light curves. To test this hypothesis you need to

Table 5.1 Summary of photometric observations. The number of measurements, starting and ending times, and average magnitude are given. HJD zero-point is 2450 000. Single point uncertainties are between 4 and 6 mmag

Database	N	HJD_{start}	HJD_{end}	mag	band
OGLE-IV	4881	5260.87825	7332.51343	16.145	I
OGLE-IV	121	5266.85770	7269.53203	19.314	V

investigate in more detail system like these. In this studio, we present a photometric analysis to the eclipsing binary OGLE-BLG-ECL-253799 (α_{j2000} = 18:01:23.91, δ_{j2000} = -27:11:28.6). This interesting system was presented for the first time by Soszyński et al. (2016), who drew attention to its unusual light curve. Our main motivation is to investigate the physical phenomena that could be the cause of its photometric variability, in particular the notable eclipse inversion, in order to contribute to the understanding of its physical and evolutionary stage.

5.3 Photometric analysis

For our analysis we have 4881 observing epochs from the OGLE-IV I-band database, which is described by Udalski et al. (2015). As summarized in Table 5.1, there are about 5.5 years of observation. In this chapter we use the ephemeris for the light curve minimum published by Soszyński et al. (2016), which is given by the following equation:

$$\mathrm{HJD_{min}} = 245\,5321.77827 + 37^{\mathrm{d}}.6445530 \tag{5.1}$$

The I-band light curve is almost typical of an eclipsing binary star, but it shows the peculiarity of having deeper minima between HJD 245 5800 and HJD 245 6200 (Fig. 5.1). We separately identified the data in this time range and phased the light curve with the orbital period, finding that these data-points follow an entirely different light curve morphology (Fig. 5.2). Surprisingly, when the star get the deeper minima the secondary eclipse turns to be the primary one. Evidently, between HJD 245 5800 and HJD 245 6200 something occurred in the system that changed their light curve deeply.

We measured the color indexes for the primary and secondary minimum in both datasets. For the larger dataset we get $V-I$ = 3.983 ± 0.125 and 3.249 ± 0.034 mag, while for the smaller dataset

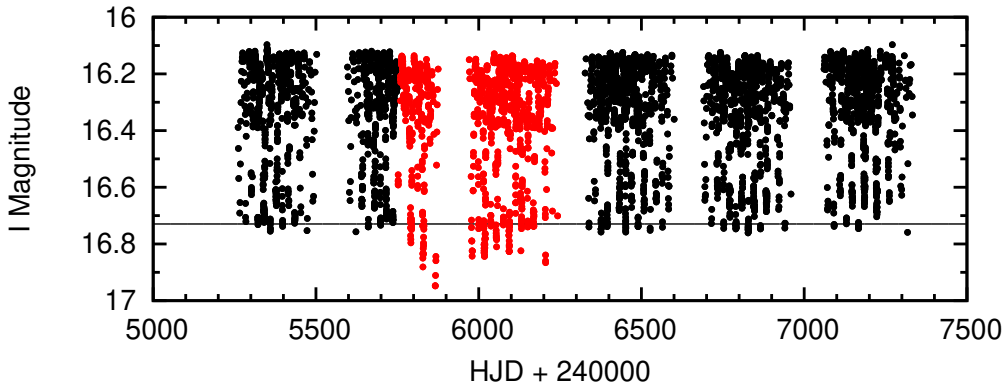

Figure 5.1 The solid black line represents the mean of the primary minimum (16.7295 mag). The black dots represent the data where the minimum is similar to this value and the red dots represent the data where the magnitude is lower to this value. Black and red dots constitute the *large* and *small* datasets in this study, respectively.

we get $V - I$ =3.998 ± 0.125 and 3.140 ± 0.033 mag. Assuming a secondary star dominating the light of the system at secondary eclipse, and using the empirical data tabulated by Cox (2000a), we estimated an effective temperature of 3200 K for the secondary star, i.e. a M-type spectral type.

We have carried out a photometric analysis with PERIOD04[1] (Lenz & Breger, 2005), in order to find additional periodicities. For that we searched additional frequencies in the residual light curve, after removing the main frequency with the disentangled method presented by Mennickent et al. (2015). As shown in the periodogram of Fig. 5.3, no additional periodicity was found.

5.4 The best light curve model

We modeled the light curve with a code developed by Gojko Djurašević (Djurašević, 1992a,b) which uses the inverse-problem solving method to obtain the best fit. This program has been used in several binary systems and is described in detail in many places (e.g. Djurašević et al., 2010; Mennickent et al., 2015; Garcés L. et al., 2018), hence only a brief description is given here.

The code considers the system as consistent of a secondary star and a primary surrounded by an accretion disc, that is both optically as geometrically thick. The geometrical properties of the disc are determined by its radius ($\mathcal{R}_d$), its thickness at the edge (d_e), and the thickness at the centre (d_c). The cylindrical edge of the disc is characterized by its temperature (T_d), and the

[1] https://www.univie.ac.at/tops/Period04/

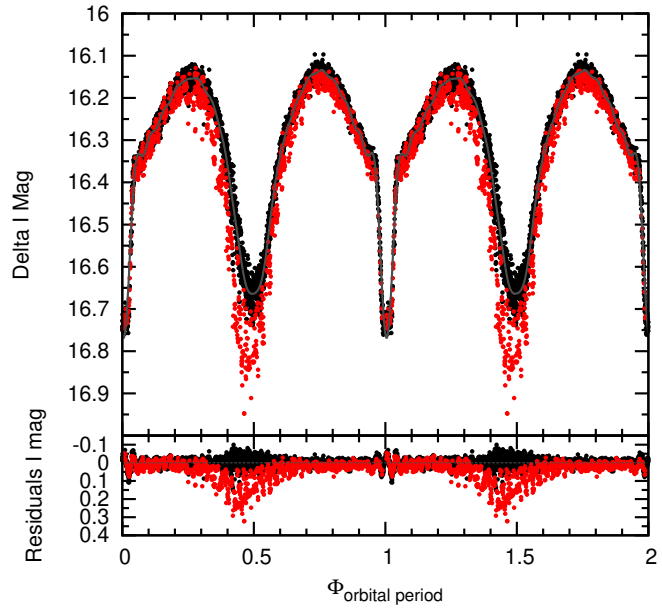

Figure 5.2 Upper panel shows red and black dots that follow the division made in the Fig. 5.1. The solid gray line represents a fit to the data represented with black dots. The bottom panel shows the residuals of the fit, indicating that the larger variability occurs close to the secondary minimum.

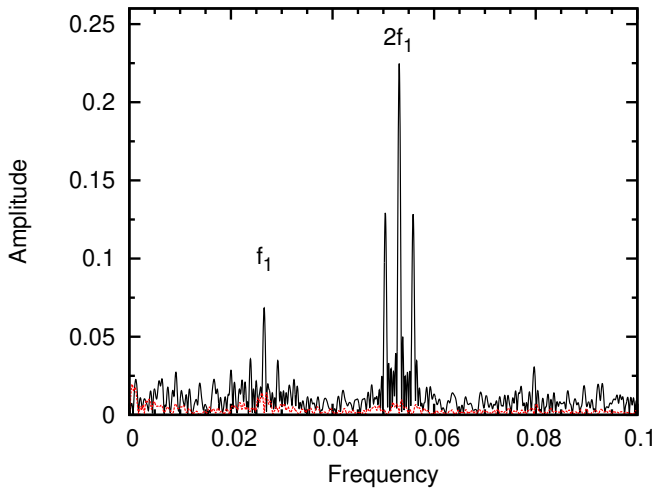

Figure 5.3 Periodogram spectrum of the OGLE-IV *I*-band photometry. Black lines indicates the main frequency corresponding to the orbital period (f_1). Red lines indicates the spectrum once the orbital period has been removed. No more frequencies are observed.

conical surface of the disc by a radial temperature profile that follows a modified version of the temperature distribution proposed by Zola (1991):

$$T(r) = T_d + (T_h + T_d)\left[1 - \left(\frac{r - \mathcal{R}_h}{\mathcal{R}_d - \mathcal{R}_h}\right)\right]^{a_T} \tag{5.2}$$

We assume that the disc is in physical and thermal contact with the gainer, so the inner radius and temperature of the disc are equal to the temperature (T_h) and radius ($\mathcal{R}_h$) of the star. The temperature of the disc at the edge (T_d) and the temperature exponent (a_T), as well as the radii of the star ($\mathcal{R}_h$) and of the disc ($\mathcal{R}_d$) are free parameters, determined by solving the inverse problem. Based on previous experience with semidetached close binaries and in order to improve the fit during eclipse ingress and egress, our model includes two hot active regions: a hotspot (h_s) and a bright-spot (b_s). These regions are characterized by their temperatures, angular dimensions, and longitudes. These parameters are also determined by solving the inverse problem and along with all other adjustable parameters, for the small and large datasets, are given in Table 5.2 for the best fits. The light curve models are compared with the observations in Fig. 5.4

Since no additional system information is available and we are looking at this first stage only a qualitative interpretation of the phenomenon, we assumed a mass ratio of $q = M_2/M_1 = 0.22$ during our analysis. Further analyses showed that our results are not particularly sensitive to the election of this parameter. In any case, the absolute parameters obtained in this study must be considered as first approximations, whereas the qualitative result of explaining the changes in light curve morphology in terms of disc parameters variability is a more robust result.

We arrive to the following results (Table 5.2): The binary consists of a A-type dwarf of temperature 10 kK, mass 3.3 $M_\odot$ and radius 1.8 $R_\odot$ and a M-type evolved star of temperature 3.2 kK, mass 0.7 $M_\odot$ and radius 19.4 $R_\odot$. The binary period is $37.^d64$ and the orbital separation 75 $R_\odot$. The primary is surrounded by a disc of radius about 33 $R_\odot$ and outer temperature 2104 K (large dataset) and 2140 K (small dataset). The disc vertical thickness at the outer edge changes from 3.87 $R_\odot$ (large dataset) to 6.26 $R_\odot$ (small dataset). The disc has a very bright hotspot 31% hotter than the surrounding disc area in the large dataset and 45% in the small dataset, located at about 50 degree apart from the lines joining the stellar centers in the direction of the orbital motion. A second bright spot is located about 116 degrees (70 degrees for the small dataset) from the lines joining the stellar centers in the direction opposite to the orbital motion. This bright spot is 13%

hotter than the surrounding disc area for the large dataset and 26% hotter for the small dataset.

The excellent fit to the light curves in both datasets suggests that the observed variability is caused by the changes in disc properties, in particular its vertical thickness, hot and bright spot temperatures and minor changes in the temperature and radius. We especially notice that for the large dataset the disc does not fully cover the hot star, producing the minimum primary in the expected orbital phase. For the smaller dataset however, an increase in the vertical size of the accretion disc occurs, covering the brightest star, producing the primary minimum near orbital phase $\Phi_o = 0.5$. At these epochs the hot and bright spots turn to be hotter. Our model also naturally explains the O-C diagram in Fig. 5.3, especially the increase in the dispersion close to $\Phi_o = 0.5$.

Using PARSEC stellar evolutionary tracks (Bressan et al., 2012) it is clear that the less massive donor is much more evolved than the more massive gainer, as occurs in Algol semidetached binaries. This dubbed "Algol-paradox" occurs because the donor was once the more massive star of the system, evolved first until filling its Roche-lobe and started a process of mass transfer into the gainer. At present, the donor turns to be the less massive and more evolved star of the system, and the gainer has acquired part of its transferred mass, being part of this transferred mass still stored in the accretion disc.

We observe the donor evolved and close to a low mass star path, specifically the track of a 1 $M_\odot$ star. On the contrary, the gainer is practically on the main sequence, and its position corresponds to a not evolved more massive star. We observe a small discrepancy for the gainer, between the mass corresponding to the model of the closer track (about 2.5 $M_\odot$) and the mass we found, viz. 3.3 $M_\odot$. This difference can be attributed to its occultation by the accretion disc, which might affect our model, and also to the assumptions done in this study.

5.5 Discussion

It is interesting that the event described by the small dataset can be interpreted in terms of a thicker disc. This naturally should occur if the mass transfer from the donor to the disc *increases* during this epoch, producing such a change. This is consistent with the hotter shock regions observed at this stage. A semidetached system in a mass transfer stage should naturally explain the existence of the disc.

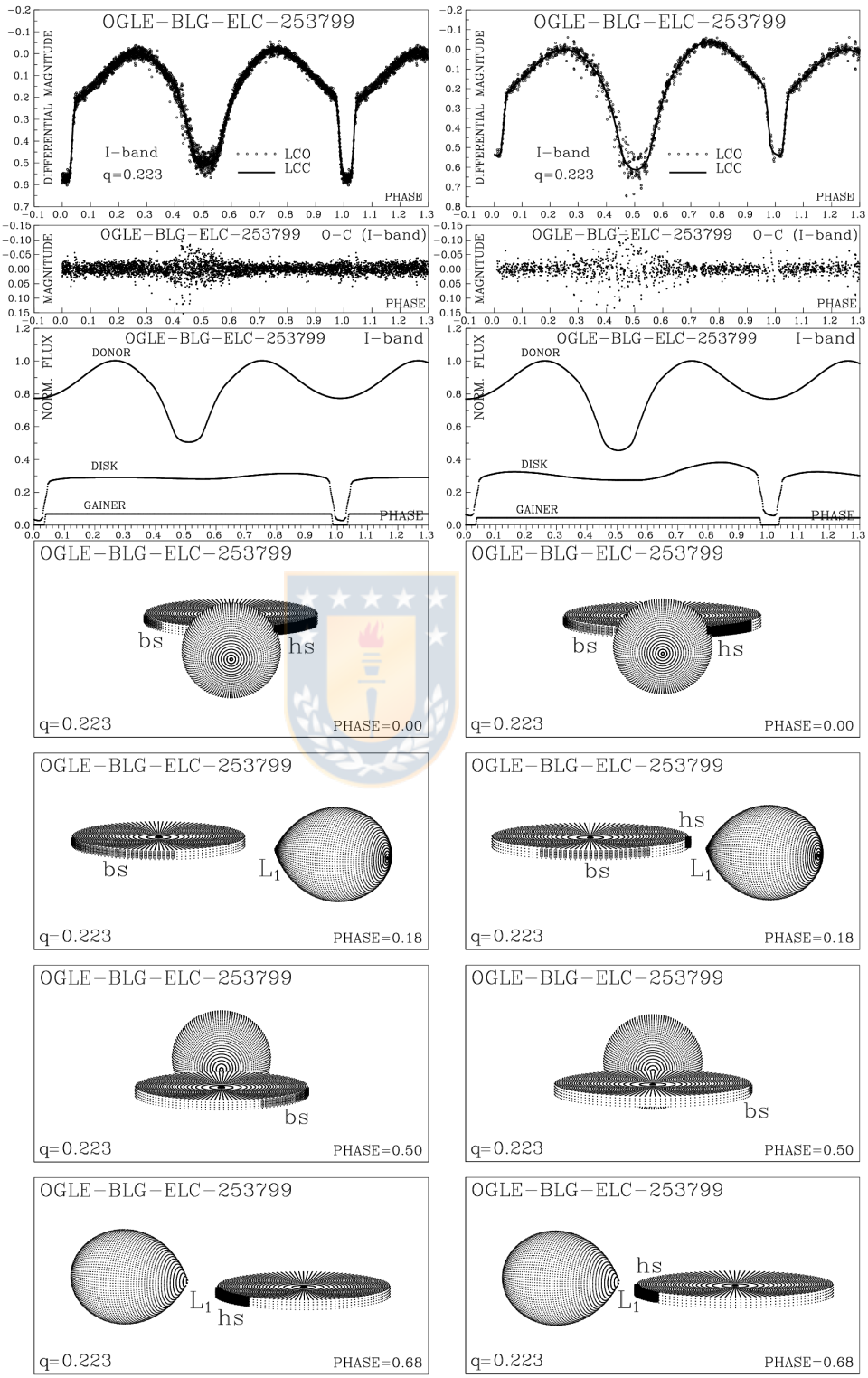

Figure 5.4 Left: Theoretical model applied to the black data set in Fig. 5.2. Right: Theoretical model applied to the red data set in Fig. 5.2. Observed (LCO), synthetic (LCC) light-curves and the final fluxes of donor, gainer and of the accretion disc of OGLE-BLG-ELC-253799, normalized to the donor flux at phase 0.25. The views of the model at orbital phases 0.00, 0.18, 0.50 and 0.68 are shown, where the parameters estimated are obtained by the light curve analysis for both data sets.

Since the donor is a M-type evolved star with an interior dominated by convective motions it is possible that it is a magnetically active star. This means that a magnetic dynamo could exist and potentially explain epochs of larger mass transfer. This connection between a dynamo and mass transfer is possible if the donor changes its quadrupole momentum and passes through epochs of larger equatorial radius, increasing the mass transfer through the inner Lagrangian point, something already postulated for the Algol-related DPVs (Schleicher & Mennickent, 2017; Mennickent et al., 2018) in the framework of the Applegate's mechanism (Applegate, 1992). In this context it should be interesting to look for new epochs of eclipse inversion in the future, to investigate if the phenomenon is periodic, recurrent or quasi-cyclical.

5.6 Conclusion

We have explained the unusual behavior of the eclipsing binary OGLE-BLG-ECL-253799 reported by Soszyński et al. (2016) in terms of structural changes of an accretion disc. In particular, the reversal of the primary and secondary eclipses can be explained by a change in the vertical thickness and minor changes in the temperature and radius of the disc, which also contributes to the change of the light-curve shape. This can be understood in terms of a variable mass transfer flow in a semidetached system, being the disc thicker and with hotter shock regions when more mass is injected from the donor star.

We notice that objects with double photometric periodicity have shown similar behaviors, for instance the DPVs. However, our case is different, since these changes do not obey to extra periodicities present in the photometry and are limited to a rather restricted period of time, about 400 days in the studied time baseline of 5.5 years. This makes hitherto OGLE-BLG-ECL-253799 a truly unique object possibly showing transient episodes of mass transfer. The object can be further studied with the aid of high-resolution spectroscopy with 8-meter class telescopes. This is especially important to determine precise stellar parameters and evolutionary stages for the components.

Since this unique system contains a M-type evolved star and shows evidence for variable mass transfer, it might be relevant in the study of the magnetic dynamo in semi-detached binaries with chromospherically active components and its effect on the mass exchange efficiency.

Table 5.2 Results of the analysis of OGLE-BLG-ELC-253799 light curves.

Quantity	large dataset	small dataset	Quantity	large dataset	small dataset
n	7331	2433	$\theta_{bs}[^\circ]$	48.6 ± 3.2	35.7 ± 6.1
$\Sigma(O-C)^2$	2.523	1.709	$\lambda_{bs}[^\circ]$	103.6 ± 6.1	61.8 ± 8.8
σ_{rms}	0.0186	0.0268	Ω_h	42.306 ± 0.006	42.755 ± 0.007
$i[^\circ]$	80.5 ± 0.5	82.3 ± 0.6	Ω_c	2.289 ± 0.004	2.289 ± 0.004
F_d	0.843 ± 0.02	0.961 ± 0.03	$\mathcal{M}_h[\mathcal{M}_\odot]$	3.31 ± 0.1	3.31 ± 0.1
T_d[K]	2110 ± 100	2140 ± 100	$\mathcal{M}_c[\mathcal{M}_\odot]$	0.74 ± 0.07	0.74 ± 0.07
$d_e[a_{orb}]$	0.050 ± 0.01	0.055 ± 0.02	$\mathcal{R}_h[R_\odot]$	1.78 ± 0.1	1.77 ± 0.1
$d_c[a_{orb}]$	0.032 ± 0.005	0.036 ± 0.008	$\mathcal{R}_c[R_\odot]$	19.44 ± 0.1	19.44 ± 0.1
a_T	7.4 ± 0.3	7.9 ± 0.4	$\log g_h$	4.45 ± 0.03	4.46 ± 0.03
F_h	0.050 ± 0.006	0.049 ± 0.008	$\log g_c$	1.73 ± 0.03	1.73 ± 0.03
T_h[K]	10200 ± 600	10500 ± 700	M^h_{bol}	1.08 ± 0.05	0.93 ± 0.06
T_c[K]	3240	3240	M^c_{bol}	0.86 ± 0.05	0.86 ± 0.06
$A_{hs} = T_{hs}/T_d$	1.31 ± 0.1	1.46 ± 0.1	$a_{orb}[R_\odot]$	75.23 ± 0.4	75.23 ± 0.5
$\theta_{hs}[^\circ]$	21.5 ± 2.1	21.6 ± 2.5	$\mathcal{R}_d[R_\odot]$	32.91 ± 0.3	37.52 ± 0.4
$\lambda_{hs}[^\circ]$	307.6 ± 6.1	319.4 ± 7.4	$d_e[R_\odot]$	3.77 ± 0.1	4.12 ± 0.2
$\theta_{rad}[^\circ]$	−13.6 ± 5.3	−20.2 ± 6.1	$d_c[R_\odot]$	2.40 ± 0.1	2.68 ± 0.2
$A_{bs1} = T_{bs}/T_d$	1.11 ± 0.1	1.26 ± 0.15			

FIXED PARAMETERS: $q = \mathcal{M}_c/\mathcal{M}_h = 0.223$ - mass ratio of the components, T_c = 3240K - temperature of the less-massive (cooler) donor, $F_c = 1.0$ - filling factor for the critical Roche lobe of the donor, $f_h = 1.0; f_c = 1.00$ - non-synchronous rotation coefficients of the gainer and donor respectively, $\beta_h = 0.25; \beta_c = 0.08$ - gravity-darkening coefficients of the gainer and donor, $A_h = 1.0; A_c = 0.5; A_d = 1.0$ - albedo coefficients of the gainer, donor and disc.

Quantities: n - number of observations, $\Sigma(O-C)^2$ - final sum of squares of residuals between observed (LCO) and synthetic (LCC) light-curves, σ_{rms} - root-mean-square of the residuals, i - orbit inclination (in arc degrees), $F_d = R_d/R_{yc}$ - disc dimension factor (ratio of the disc radius to the critical Roche lobe radius along y-axis), T_d - disc-edge temperature, d_e, d_c, - disc thicknesses (at the edge and at the center of the disc, respectively) in the units of the distance between the components, a_T - disc temperature distribution coefficient, $F_h = R_h/R_{zc}$ - filling factor for the critical Roche lobe of the hotter, more-massive gainer (ratio of the stellar polar radius to the critical Roche lobe radius along z-axis), T_h - temperature of the more-massive (hotter) gainer, $A_{hs,bs} = T_{hs,bs}/T_d$ - hot and bright spots' temperature coefficients, $\theta_{hs,bs}$ and $\lambda_{hs,bs}$ - spots' angular dimensions and longitudes (in arc degrees), θ_{rad} - angle between the line perpendicular to the local disc edge surface and the direction of the hot-spot maximum radiation, $\Omega_{h,c}$ - dimensionless surface potentials of the hotter gainer and cooler donor, $\mathcal{M}_{h,c}[\mathcal{M}_\odot]$, $\mathcal{R}_{h,c}[R_\odot]$ - stellar masses and mean radii of stars in solar units, $\log g_{h,c}$ - logarithm (base 10) of the system components effective gravity, $M^{h,c}_{bol}$ - absolute stellar bolometric magnitudes, a_{orb} [$R_\odot$], $\mathcal{R}_d[R_\odot]$, $d_e[R_\odot]$, $d_c[R_\odot]$ - orbital semi-major axis, disc radius and disc thicknesses at its edge and center, respectively, given in the solar radius units.

6

Study of the long and orbital cycle in LCM and SMC DPVs

6.1 Abstract

The good photometric coverage of DPVs in the LMC and SMC made by the databases OGLE (Udalski et al., 1997; Udalski, 2003; Udalski et al., 2015), have allowed us to study this phenomenon in detail as never before. We performed a mathematical analysis to study the dispersion of the photometric data in the eclipsing (ECL) and ellipsoidal (ELL) DPVs. This allows us to investigate the dependency that the long cycle presents with the inclination of the system. We found that the ELLs DPVs presents a smaller photometric dispersion compared to the ECLs. On the other hand, considering the changes in the morphologies of the light curves shown in the previous sections, we have carried out a complete analysis of the light curves of all the LMC and SMC DPVs, available in the OGLE database. This is how we found 11 new DPVs with considerable changes in the depths of the primary and secondary minimum, directly related to the long cycle. In 10 of them we found combinations of frequencies in the residuals of the light curves, whose origin we still cannot understand. However, we eliminate the additional frequencies present in some DPVs considering a long period change in 25 systems. Our study will allow the selection of objects for more detailed studies that use longer time bases in the future, such as OGLE V and LSST.

6.2 Introduction

DPV systems show a long cycle ($\sim 33\ P_o$) of uncertain origin (Mennickent et al., 2003; Mennickent, 2017). Since its discovery it has been speculated about its origin, being the bipolar wind of the hotspot, modulated by the mass transfer between the components, one of the most convincing explanations (Mennickent et al., 2012a, 2016b). While this has not been observed in all DPVs studied spectroscopically, the inclination of the system would play an important role. A low inclination of the orbital plane would favor bipolar wind observation (Mennickent et al., 2016b). Recently the magnetic dynamo theory for DPVs has been proposed (Schleicher & Mennickent, 2017). The strong magnetic activity on the donor would produce changes in its radius, modulating the rate of mass transfer to the gainer (Applegate, 1992).

As we have seen Chapters 3 and 4, two DPV systems present changes in their orbital light curves directly related to the long cycle, which could be a key piece in understanding the DPV phenomenon since the changes observed could be evidence of a cyclic mass transfer rate in these systems.

In this chapter, we present a photometric study conducted in the LMC and SMC DPVs. Unlike the catalogs presented by Poleski et al. (2010) and Pawlak et al. (2013), we consider a longer time series including the OGLE IV data. In Section 6.3 we show a mathematical analysis of the dispersion of the long cycle in the ellipsoidal and eclipsing DPVs. Our objective is to inquire about the role of the inclination of the orbtial plane in the observation of the long cycle in DPV systems. In addition, in Section 6.4 we show 11 (10 DPV LMC and 1 SMC) new systems that present changes in their light curves directly related to long cycle stages. Finally, we analyze the residuals of the disentangled of the light curves in search of frequency combinations. Our goal is to investigate its origin.

6.3 Long cycle dispersion in eclipsing and ellipsoidal DPVs

In this study we found 38 ECL and 84 ELL DPVs in LMC (Poleski et al., 2010). Using the Pawlak et al. (2013) catalog, we found 20 as ECL DPVs in SMC. We do not register ELL in the catalog. We noticed that within the ECL group some curves of light of the long cycle were not sinusoidal, but have a double hump (DH), which 7 belong to LMC and 4 to SMC. In LMC some of them had

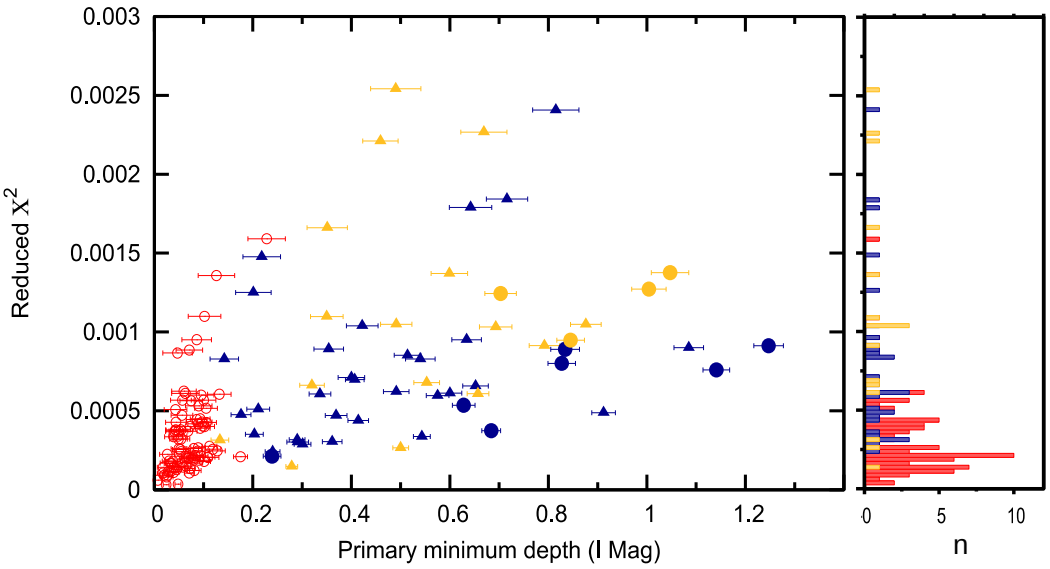

Figure 6.1 Reduced χ^2 vs. primary minimum depth of the orbital light curve. In red, the DPVs cataloged as ELL in the LMC. In blue, the DPVs cataloged as ECL in the LMC. In yellow, the DPVs cataloged as ECL in SMC.

already been cataloged with this nature (Mennickent et al., 2008; Poleski et al., 2010; Mennickent et al., 2019).

For this analysis it is necessary to make a good disentangle of both light curves. For these reasons, we exclude 1 DPV from the Pawlak et al. (2013) catalog in SMC (OGLE-SMC-ECL-2049), since it does not have a defined long cycle morphology and its long period is increasing dramatically. Similarly, we excluded 14 DPVs from LMC (Poleski et al., 2010) from our study either because their photometry is very faint or because one of the two cycles was not well defined. Some of them are listed as uncertain in the catalog of Poleski et al. (2010).

In all the DPVs analyzed in this study, the orbital period remains constant. On the other hand, in some DPVs the long period is changing significantly (e.g. Mennickent et al., 2008, 2019; Poleski et al., 2010). For our analysis, it is essential that the periods used in the disentangle are representative of the photometric data set. In this way, we will avoid a bad disentangle, as well as an additional dispersion of the long cycle light curve. For these reasons, we carefully analyze the periodicity of this cycle using the time of the maximum observed (O) minus the calculated (C) one. Thereby, we managed to identify 25 DPVs with variable long period, of which 17 are ELL and 8 are ECL (See Fig. A.17, A.18, A.19). Two of them were studied by Poleski et al. (2010) and none

in SMC by Pawlak et al. (2013). All of them maintain a constant long cycle morphology as the long period varies, allowing us to analyze the photometric dispersion using all the data available for these objects.

From our analysis we find the following. The amplitudes of the long cycle in the ELL DPVs vary between 0.004 to 0.26 I-mag, while in the ECL studied between 0.01 to 0.20 I-mag. It is striking that OGLE-DPV-LMC-097 is the only system with a considerably longer cycle amplitude compared to the rest of the sample (~0.4 I-mag).

In order to obtain a measure of the dispersion of the long cycle, we perform a mathematical adjustment using Eq. 2.6 Thus we obtain the reduced χ^2 through the following equation:

$$\chi^2 = \sum_i (O - C)^2 / \nu \tag{6.1}$$

with $\nu = N - n$, where N is the number of observations and n the number of fitted parameters ($n = 9$ in all the curves analyzed). The mathematical fit allows us to also obtain the amplitude of the long cycle curve. Although both show similar amplitude distributions, it is evident that the ELL group shows a much smaller photometric dispersion (See Fig. 6.1).

Now, it is valid to ask why the photometric dispersion of the long cycle varies between DPVs ELL and ECL. Poleski et al. (2010) showed the variation of amplitude of the long cycle in the OGLE-LMC-DPV-074 system. It clearly shows an increase in amplitude during the orbital phase $\Phi_o = 0.5$ and a decrease in the amplitude during the primary minimum of the orbital phase ($\Phi_o = 1$). We performed the same analysis noting a similar behavior between OGLE-LMC-DPV-074 and OGLE-BLG-ECL-157529 (See Fig. A.4). Meanwhile, OGLE-LMC-DPV-097 also shows a decrease in amplitude in the orbital phases $\Phi_o = 0.5$ and $\Phi_o = 1$ (See Fig. A.4). In the same way, we performed a visual inspection of the rest of the DPVs considered in this study, noting that the ECLs show variations in the amplitude of the long cycle (very small in some cases), while in the ELLs these variations are imperceptible. We restrict ourselves to showing only some representative cases of the observed ones (See Fig. A.5). This behavior in some ECL DPVs could explain the greater photometric dispersion of the long cycle, considering that in the ELL DPVs the amplitude does not vary considerably.

On the other hand, we analyze if there is any correlation between the estimated dispersion (χ^2) and the magnitude of the system (I-Band OGLE average), to see if the brightest objects have less

dispersion. We found a correlation coefficient (CC) of 0.40 for the entire sample (CC = 0.48 for ELL and CC = 0.31 for ECL). In this way, we rule out that the brightest DPVs have a less noisy long cycle photometry.

Finally, in this analysis we do not have the inclination of the systems studied, so we assume that a greater depth of the primary minimum is associated with a greater inclination (and vice versa). Assuming this, we could say that at a lower inclination of the orbital plane, we observe a less dispersed photometry of the long cycle. On the contrary, at a greater inclination, we observe a noisy cycle, which in some cases could be explained by changes in the amplitude of the long cycle through the orbital phase.

6.4 Changes in the orbital light curves related to the long cycle

In Chapter 3 and 4, two cases of DPVs with changes in their light curves directly related to the stage of the long cycle in which they are found, were shown. We analyze in detail the DPVs catalogs OGLE I-band, LMC (Poleski et al., 2010) and SMC (Pawlak et al., 2013), in search of DPVs with this phenomenon. The orbital curves were obtained from the photometric disentangle using a Fourier decomposition algorithm (Section 2) described by Mennickent et al. (2012a). In addition, using the methodology described in Sections 2.1, 2.2, 2.3 we were able to identify this phenomenon in 9 ECL (2 DH). We only identify 2 ELLs DPV with these changes. Since the photometric changes we are looking for occur principally in the primary and secondary minimums of the light curves, is that the largest number of DPVs with this phenomenon are ECL. We restrict the cases shown only to those in which the phenomenon is totally evident. We will briefly describe these objects below.

OGLE-LMC-DPV-006: Its orbital period is 8.278144 d. The long cycle has a constant period of 252.74 d. and a sinusoidal morphology. We clearly notice changes in the depth of the primary and secondary minimum. Both are deeper during the maximum phase of the long cycle and less deep in the minimum phase (See Fig. A.6).

OGLE-LMC-DPV-014: It has an orbital period of 6.196641 d and a sinusoidal long cycle of 179.86 d. Clearly, the primary and secondary minimums change depth. Both reach the greatest depth during the maximum phase of the long cycle and its lowest depth during the minimum phase (See Fig. A.7).

OGLE-LMC-DPV-026: Its orbital period is 5.179857 d and its long cycle of 154.044 d. The morphology of the long cycle is sinusoidal. We notice changes mainly in the secondary minimum through the different stages of the long cycle. It is deeper during the maximum and less deep during the minimum phase. We do not notice considerable changes in the primary minimum (See Fig. A.8).

OGLE-LMC-DPV-056: Its orbital period is 7.284285 d. It has a DH long cycle whose variability is limited to half a cycle and its period decreases from 185-178 days (Mennickent et al., 2008). Although the long period is changing considerably, the morphology of the light curve remains constant. We notice changes in the secondary minimum at the different stages of the long cycle. It is deeper during the maximum and less deep during the descending phase. We do not notice considerable changes in the primary minimum (See Fig. A.9).

OGLE-LMC-DPV-058: It has an orbital period of 8.307366 d. Its long period decreases slightly from 315 to 309 d. The long cycle morphology is DH with a secondary maximum much smaller than the main maximum. In addition, as this changes, its morphology of long cycle remains constant. We notice changes in the secondary minimum through the different stages of the long cycle. It is deeper during the maximum and less deep during the minimum phase. We do not notice considerable changes in the primary minimum (See Fig. A.10).

OGLE-LMC-DPV-062: Its orbital period is 6.904830 d and it has a long constant cycle of 229.080 d and sinusoidal morphology. The secondary minimum has its greatest depth during the maximum of the long cycle, while it reaches its lowest depth during the minimum. We notice slight changes in the primary minimum, which reaches a lower depth during the descending phase and its greater depth during the maximum and ascending phase of the long cycle (See Fig. A.11).

OGLE-LMC-DPV-074: Its orbital period is 38.159229 d. We consider an increase in the long period from 754 to 806 d, during the 17.2 years of observation. Its long cycle is quite noisy. The primary minimum of the orbital cycle reaches its greatest depth during the maximum of the long cycle, while it has a lower depth during the minimum of the long cycle. The opposite is the case with the secondary minimum of the orbital cycle, which has a greater depth during the minimum of the long cycle and a lower depth during the maximum. It is the only LMC DPV that we encounter a behavior similar to that shown by OGLE-BLG-ECL-157529 (Chapter 4), reversing the primary and secondary minimum throughout the long cycle (See Fig. A.12).

OGLE-LMC-DPV-121: It has an orbital period of 7.626962 d and a constant long cycle period of 272.313 d and a DH morphology. The primary and secondary minimum change depth during the different stages of the long cycle. Both reach their greatest depth during the maximum of the long cycle, while they are less deep during the minimum of the long cycle (See Fig. A.13).

OGLE-SMC-ECL-5637: It is the only DPV in the SMC catalog that shows evident variations in the orbital light curve (5.6021 d) related to the long cycle. It shows an orbital light curve with similar primary and secondary minimum. Its long cycle is noisy with a constant period of 149.01 d. Both minimums of the orbital cycle change through the different stages of the long cycle. Both the primary and secondary minimum are deeper during the long cycle maximum, while they become less deep during the minimum (See Fig. A.14).

Below we briefly describe what was observed in the orbital light curves of the 2 ELL DPVs.

OGLE-LMC-DPV-022: It is one of the DPV with the longest orbital period in LMC (45.188161 d). Its long cycle is quite noisy and the photometry used does not cover it completely, due to its great period of 1778.726 d. The morphology of the light curve is unusual, it shows a large maximum in the second quadrant (around the $\Phi_o = 0.75$), which is clearly higher than the maximum of the first quadrant ($\Phi_o = 0.25$). We note that during the minimum and ascending phase of the long cycle, the orbital cycle reaches a maximum in the second quadrant. While in the maximum and descending phases this maximum decreases and resembles that observed in the first quadrant. We note that the first and second quadrants have the same maximum during the descending phase of the long cycle. We do not observe drastic changes in the primary and secondary minimums (See Fig. A.15).

OGLE-LMC-DPV-035: It has an orbital period of 7.697490 and a sinusoidal long cycle of 228.995 d. We notice that the secondary minimum is deeper during the maximum of the long cycle, while it is less deep during the minimum. Similarly, we observed differences in the morphologies of the light curves around the secondary minimum. Also, we notice differences in the first and second quadrants. During the maximum of the long cycle, the first quadrant has a slightly higher maximum than the second quadrant. This is reversed in the descending phase (See Fig. A.16).

As we have noticed, the main changes in the orbital light curves are related to variations in the depth of the primary and secondary minimum. The latter varies in 11 of the 12 DPVs studied in this secction and we notice a pattern in their behavior. In 10 DPVs, it is observed that the secondary minimum is deeper in the maximum stage of the long cycle, reaching its lowest depth in the low stage of the long cycle. Only OGLE-LMC-DPV-074 shows the opposite phenomenon. With respect to the primary minimum, some follow the same pattern as the secondary minimum and in others there are no variations. Only in the 2 ELLs we notice changes in the maximum of the first and second quadrant, related to the long cycle. Both present different behaviors.

6.5 Combination and additional frequencies

Poleski et al. (2010) presents a complete photometric analysis of 137 DPV in the LMC. In their study, the residuals of the light curves are analyzed, after whitening the orbital and long period (P_o (f_o^{-1}) and P_l (f_l^{-1}) repectively). In the residuals, combinations of frequencies with peak in $f_c = f_o + f_l$ were found, in most cases (30 DPVs). Other combinations of frequencies $f_c = 2(f_o - f_l)$ have been found in 11 DPVs (Buchler et al., 2009).

In this sense, we decided to analyze the residuals of the OGLE-BLG-ECL-157529 binary system, recently discovered and analyzed for the first time in this study. As we saw in Chapter 4, this DPV also presents the changes in its light curve mentioned above. In addition, its long period is decreasing, and as it decays, the changes in depth of the primary and secondary minima become less drastic. For this system it was necessary to divide the photometry into 3 sets, due to the change of period of the long cycle (Chapter 4). We analyze the residuals of the disentangled for the 3 sets, finding a peak in the frequency combination $f_c = f_o + f_l$, where f_o is the frequency associated to the orbital period, and f_l to the long period in each of the set. This presents a peak with greater GLS power in the first set and a lower one in the third set (see Table 6.1, and Fig. 6.2). Similarly, OGLE-LMC-DPV-097 is one of the systems analyzed in Poleski et al. (2010) that presents a combination of frequencies in the residuals. As we have seen in Chapter 3, this DPV is the one that shows the most radical changes in its light curve morphology related to the long cycle. Using the GLS periodgram we corroborate the frequency combination $f_c = f_o + f_l = 0.132310 \pm 0.000012$ (c/d) (7.558013 ± 0.000700 d). In addition, we found another peak with combinations $f_c' = 2f_o + f_l$ and one at $f_c'' = 3f_o + 2f_l$ (See Fig. 6.2).

Table 6.1 Summary of the GLS periodogram analysis for DPV-Bulge. Data set, data number, frequency combination, associated period to f_c and maximum peak power GLS are shown.

Data Base	n	frequency f_c (c/d)	P_c (d)	Peak GLS
OGLEII	346	0.041605 ± 0.000069	24.035509 ± 0.040051	0.132
OGLEIII	795	0.041466 ± 0.000037	24.116054 ± 0.021787	0.081
OGLEIV	1465	0.041650 ± 0.000041	23.994560 ± 0.023709	0.062

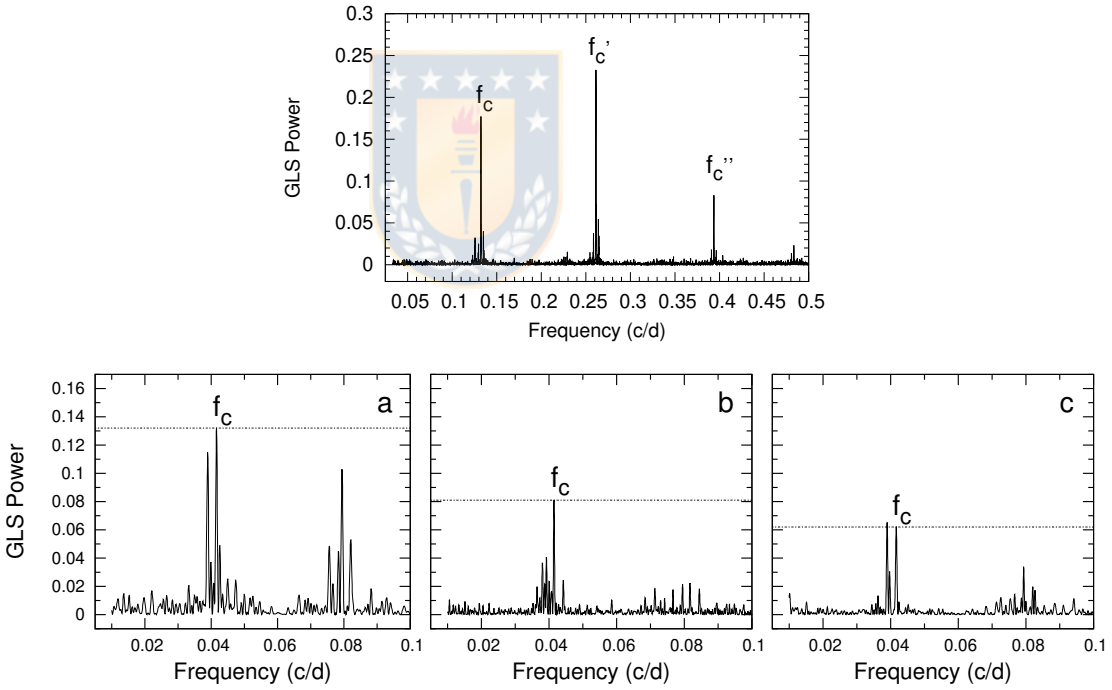

Figure 6.2 Top: GLS periodiogram of the residual data of OGLE-LMC-DPV-097. Different frequency combinations are shown $f_c = f_o + f_l$, $f_c' = 2f_o + f_l$ and one at $f_c'' = 3f_o + 2f_l$. Bottom: a) GLS periodiogram of the residuals of DPV-Bulge, using the first data set. b) using the second set. c) using the third set.

In this way, two of the objects that present changes in their light curves related to the long cycle, show clear peaks with a combination of frequency f_l and f_o. For this reason, we decided to study in detail the residuals of the objects presented in the previous section, in search of these frequency combinations. 10 of the 11 DPVs show clear peak in the residuals of the disentangled of the light curves. Of these, 6 have combinations $2f_o + f_l$ and 4 show combinations $f_o + f_l$ (See Fig. A.1). This last combination was found in the residuals of approximately 22% of the DPVs in LMC (Poleski et al., 2010). We analyzed the 30 DPVs ($\sim$ 22%) and found only 2 objects with clear changes in the orbital light curve. These had already been included in our analysis (DPV-035 and DPV-097). We did not find any object with drastic changes in the DPVs analyzed by Buchler et al. (2009).

Although 12 of the 13 DPVs analyzed in this study show combinations of frequencies, not all DPVs that present this phenomenon in the residuals of the disentangle show photometric changes related to the long cycle. As we do not know the nature of these periodicities with combinations of frequencies f_l and f_o, we have decided not to remove it from the photometry of the long and orbital cycle, so as not to over whitening the light curves.

In addition to frequency combinations, additional frequencies have been reported in the LMC DPVs. In Poleski et al. (2010), 23 objects with additional frequencies in the residuals are shown. These frequencies may appear when a real period in the disentangle of light curves are not considered. In Poleski et al. (2010), only long period variable in 2 objects are considered. As we saw in the previous section, we considered 25 objects with slight changes in the long period. When analyzing the residuals in search of the additional frequencies mentioned, we noted that these did not observe the GLS peridogram (See Fig. A.2, example DPV-080).

6.6 Discussion

We know that the long cycle is not hidden through the orbital phase (e.g. Desmet et al., 2010; Mennickent et al., 2012a). However, we noticed interesting behaviors in some ECL DPVs. For example, OGLE-LMC-DPV-097 shows a clear decrease in the amplitude of the long cycle in the 0.5 orbital phase. In this phase, the donor star is being eclipsed by the disc and the gainer star (Garcés L. et al., 2018). If we associate the decrease in amplitude with a concealment of the long cycle, we could say that its origin is in the donor star or in an area between it and the accretion disc

(e. G. Hot-spot). Other ECLs systems show a similar behavior in the 0.5 orbital phase, however the amplitude in the orbital phase 1 also decreases (examples in Fig A.4). This would indicate that the source of the long cycle would be hiding slightly twice during the orbital phase, or that there are two different sources. Totally opposite is what happens in the case of the OGLE-BLG-ECL-157529. We notice a considerable increase in amplitude in the 0.5 orbital phase, where the accretion disc is fully visible and a considerable decrease (almost an eclipse) during the primary minimum. This behavior is observed in the OGLE-LMC-DPV-074 system (Poleski et al., 2010) and just both have the same orbital cycle behavior during the long cycle stages (see Chapter 4). Perhaps in these systems the origin of the long cycle is different from that of the other DPVs. Analyzing the behavior of the long cycle through the orbital phase allows us to speculate the possible origin and nature of it. In this sense, an interesting result is the fact that cataract DPVs such as ELLs have longer cycles with less photometric dispersion compared to ECLs.

The OGLE-LMC-DPV-097 system presents the most drastic changes in the morphology of the orbital light curve, in addition to the greater amplitude of the long cycle in I-band (greater than 0.3 mag). In another 11 systems that we notice variations in the orbtial cycle, the amplitude of the long cycle ranges from 0.05 to 0.19 mag I-band. A large part of the DPVs considered in this study have similar amplitudes to these, however in the vast majority of the DPVs the orbital light curves remain constant ($\sim$ 92% of the sample) at different stages of the long cycle.

We also note that the changes observed in orbital light curves follow a common pattern. During the minimum stage of the long cycle the secondary minimum is of less depth. As the theoretical models indicate, in this orbital phase we directly observe the accretion disc. It could be structural changes of the disc, in addition to its temperature or luminosity that are producing this phenomenon, or changes in luminosity of the eclipsed stars (donor). We cannot confirm or rule out one of the possibilities, because we do not have theoretical models for these 12 systems.

An interesting result is the confirmation and having found new combinations of frequencies in the residuals of the disentangling of the light curves. With our analysis we failed to understand its nature, but it could be due to a system intrinsic phenomenon that mixes the frequency of the orbital cycle and long, or a effect of the disentangle. Mainly, it would be important to analyze the amplitude of the curve present in the residuals and compare them with the DPVs that show important changes in their orbital light curves and those in which no changes are observed.

6.7 Conclusion

In our study we classified 84 DPV ELL and 58 DPV ECL. Although the vast majority have sinusoidal long cycles, we report 11 with double hump cycles. Of the DPVs studied, 25 present changes in their long periods, maintaining the same morphology of the light curve as it changes. In this sense, we observe that both, ELL and ECL DPVs, have long cycles with similar I-band amplitudes. However ELLs have a much smaller photometric dispersion than ECLs. This could be due to changes in amplitude of the long cycle through the orbital cycle, which is observed with greater variation in the ECLs.

Regarding the orbital cycle, we show 11 new cases of DPVs that show changes in the orbital light curve directly related to the long cycle. 10 of them have an obvious pattern, the secondary minima become less deep during the maximum stage of the long cycle. Meanwhile, in only two DPV ELL we notice changes mainly in the first and second quadrants. The fact that the great majority of the DPVs with changes in the minimum of the orbtial cycle are ECL, would indicate that the inclination of the system would favor the observation of this phenomenon.

Finally, we found combinations of frequencies in 12 of the 13 DPVs (in total) that present changes in their orbital light curves related to the long cycle. However, we analyzed all previously studied DPVs that show this behavior in their residuals and we do not found these changes in their orbital cycles. To understand the nature of these frequency combinations, more studies will be necessary. On the other hand, we managed to eliminate the additional frequencies present in some DPVs considering a long period change in them.

7

Discussion and Conclusions

In our study, we considered a temporary coverage of up to 18.5 years of observation for DPVs in LMC and SMC. This has allowed us to perform a complete photometric analysis of the behavior of the orbital light and long cycle light curves. We only have photometric data for our study, so our goal is to qualitatively analyze the morphology changes that we observe in some light curves. We summarize our main results below.

i) For the OGLE-LMC-DPV-097 system, the accretion disc would be larger and cooler during the maximum phase of the long cycle, and smaller and hotter during the minimum phase. Then, the observed changes in photometry orbital should be mainly due to drastic changes in the diameter of the accretion disc. Changes in Brigth / Hot Spot temperature are also observed, in addition to the angular size and location of these active zones. The contribution of the luminosity of the disc would be greater than that of the donor and gainer during the maximum of the long cycle. This does not occur in any other DPV system modeled so far (Chapter 3).

ii) We explain the changes in the orbital light curve of the OGLE-BLG-ECL-157529 system mainly with a change in the thickness of the accretion disc, which would always be thicker in the minimum of the long cycle and thin the maximum of the long cycle. In addition, the angular size, location and temperature of the active zones would be changing throughout the long cycle. During the early stages of observation, the disc would cover the brightest star (gainer), producing a reversal of the primary minimum during the maximum phase of the long cycle (Chapter 4). This

result explains the depth changes observed in the OGLE-LMC-DPV-074 system by Poleski et al. (2010).

iii) In the same way, we explain the inversion of the primary and secondary minimums in the OGLE-BLG-ECL-253799 system, through changes in the accretion disc, mainly in the thickness Due to the characteristics of the components and considering that it does not have a long cycle, we rule out that it is a DPV system. The system would be in a transitory stage of mass transfer (Chapter 5).

The structural changes of the accretion disc have been fundamental to explain the different light curves observed throughout the long cycle stages. The donor's magnetic activity would play an important role as a possible explanation, since variations of the equatorial radius product of the Applegate mechanism would modulate the mass transfer rate (Schleicher & Mennickent, 2017) and probably the physical characteristics of the accretion disc (e.g. Garcés L. et al., 2018). This would also explain the evidence of bipolar wind found in some DPV systems (Harmanec et al., 1996; Mennickent et al., 2012a; Barría et al., 2014), in addition to the increase in hot spot brightness during the maximum phase of the long cycle in the HD170582 system (Mennickent et al., 2016b). In other systems, changes in an accretion disc have been considered as the possible explanation for the variation in depth of the minima of the orbital light curves, due to a transitory mass transfer process (Djurašević et al., 2012; Zasche et al., 2017). In this sense, the DPVs would be unique objects, considering that the observed changes occur periodically.

We inspect the DPVs in LMC and SMC available in the OGLE database. We found 11 new systems with changes in depth of the secondary and primary minimum directly related to the long cycle stages. In them a common pattern is observed, the secondary minimum is less deep during the low phase of the long cycle. We analyzed the residuals of the disentangled of the light curves of these systems and found 10 with evident combinations of frequencies in the periodgram.

We use the available photometry to analyze the relationship between dispersion of the long cycle and inclination of the orbital cycle. For this, we classify 84 as ELLs and 58 as ECLs, out of a total of 142 DPVs considered in this analysis. We note that ELL DPVs show long cycles with

less photometric dispersion than ECLs. Some ECLs show decreases in the amplitude of the long cycle in orbital phases 0 and 0.5, resulting in an increase in the total dispersion of the long cycle (Chapter 6).

In this study we explain for the first time the changes in the orbital light curves related to the long cycle of two DPVs, through a theoretical analysis. We note that the changes are mainly due to variations in the structure of the accretion disc, mainly in the thickness, diameter, temperature and characteristics of the active zones present at the outer edge of the disc. Understand the nature of the objects that we analyze in this study will be essential to test the Applegate mechanism in DPV systems. In addition, we believe it is important to consider in the future, what role bipolar jets have in the long cycle luminosity, the changes in luminosity of the accretion disc and the possible change in brightness of the donor star due to variations in the equatorial radius. Equally important will be to continue observing these objects in photometric campaigns. This will allow to study phenomena such as drastic changes of long period, as well as to detect possible variations of the orbtial period. Increase the number of DPVs cataloged in the Milky Way (Thesis Gonzalo Rojas) will be important too, in order to find variations of the orbital cycle, such as we found in DPVs of LMC and SMC.

Appendices

A

Additional figures

A.1 Complementary figures chapter 6

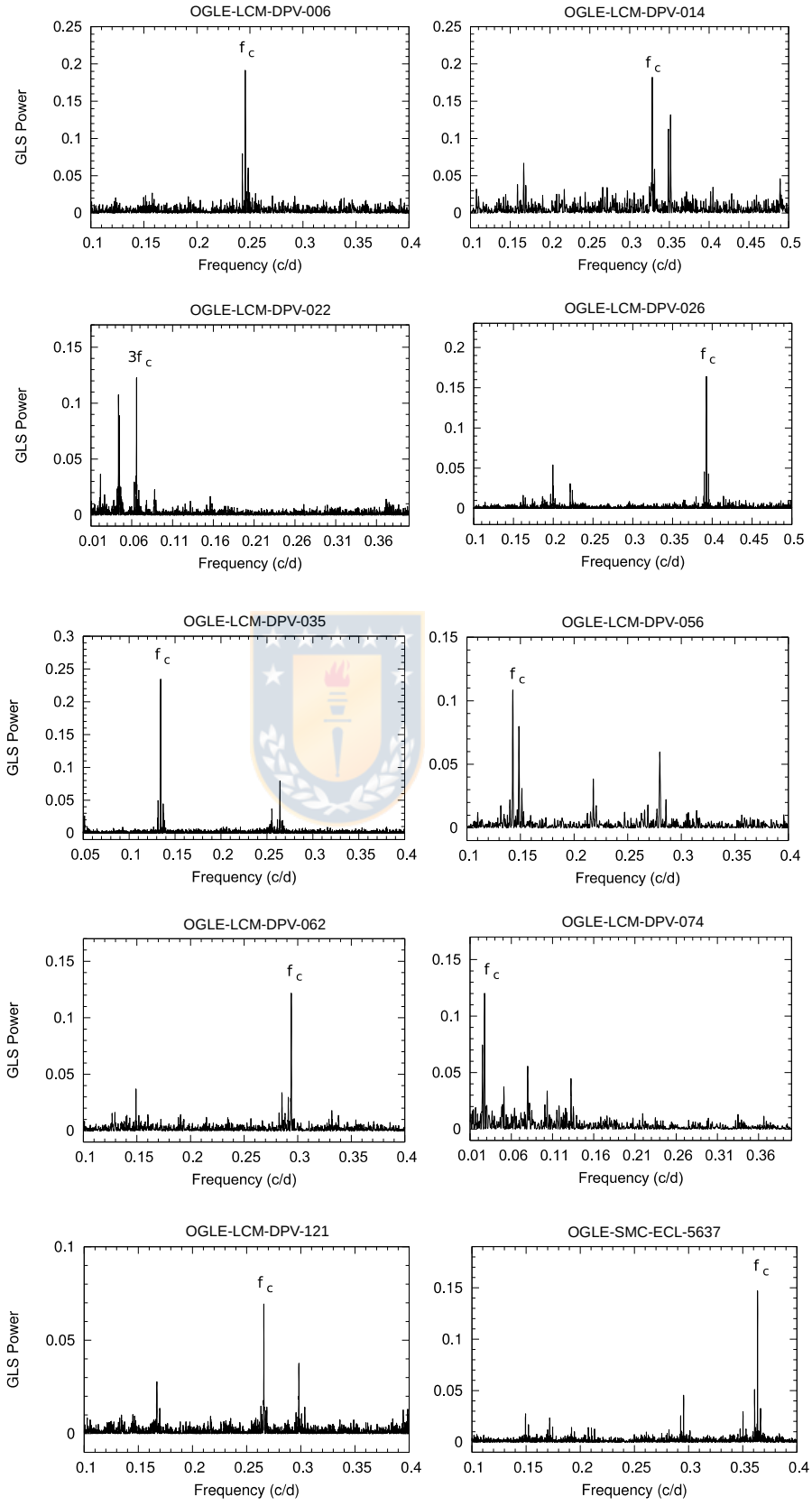

Figure A.1 GLS periodogram of 10 objects that present combinations of frequencies in their residuals. 6 present the combination $f_c = 2f_o + f_l$ (DPV-006, DPV-014, DPV-026, DPV-062, DPV-121, ECL-5637). The other 4 have the combination $f_c = f_o + f_l$ (DPV-22, DPV-35, DPV-056, DPV-74).

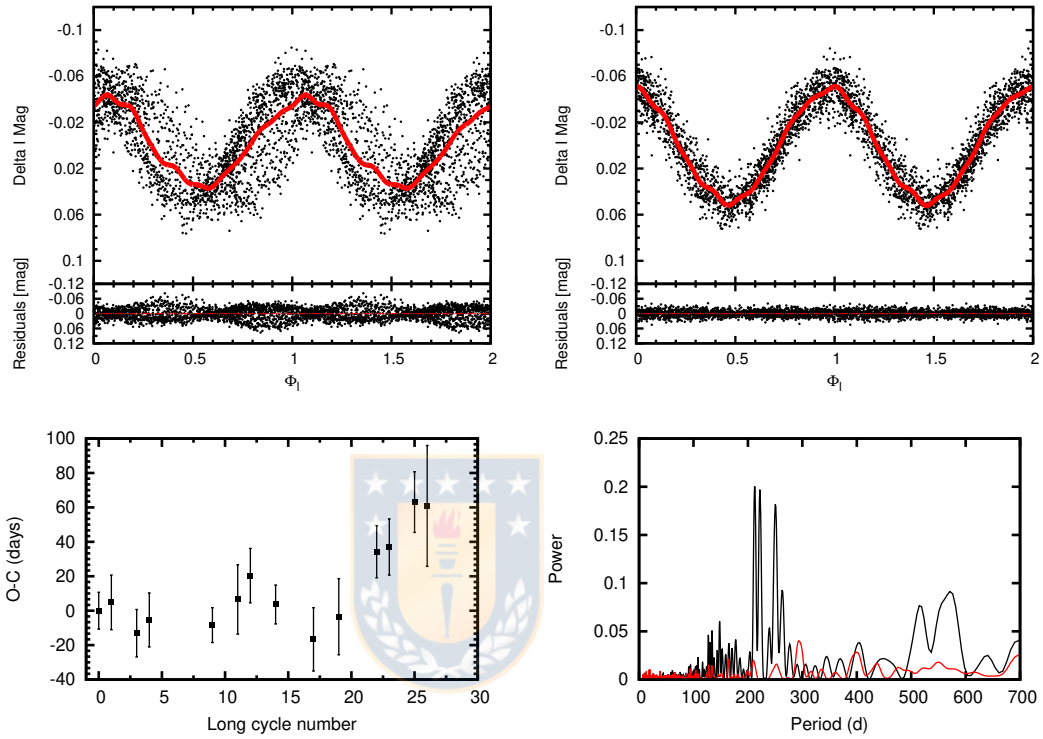

Figure A.2 DPV-080. Top-Left: Long cycle light curve considering a constant long period of 227 days. In red, an adjustment by Fourier series, to obtain the residuals of the lower panel. Top-Right: Long cycle light curve considering a variable long period. The light curves of all the data sets were put together in a single curve. In red, an adjustment by Fourier series, to obtain the residuals of the lower panel. Bottom-Left: O-C of the periods of the maximum of the long cycle. We notice a long period of 227 days almost constant until the cycle number 20. Then there is a slight increase of approximately 10 days. Bottom-Right: black line shows the periodogram of the residues when doing the disentangle of the orbital light curves and constant long cycle. Red line shows the periodogram of the residuals when doing the disentangle of the orbital light curves considering a variable long cycle. This clearly shows that some additional frequencies might apear when not properly removing a variable long cycle in the analysis.

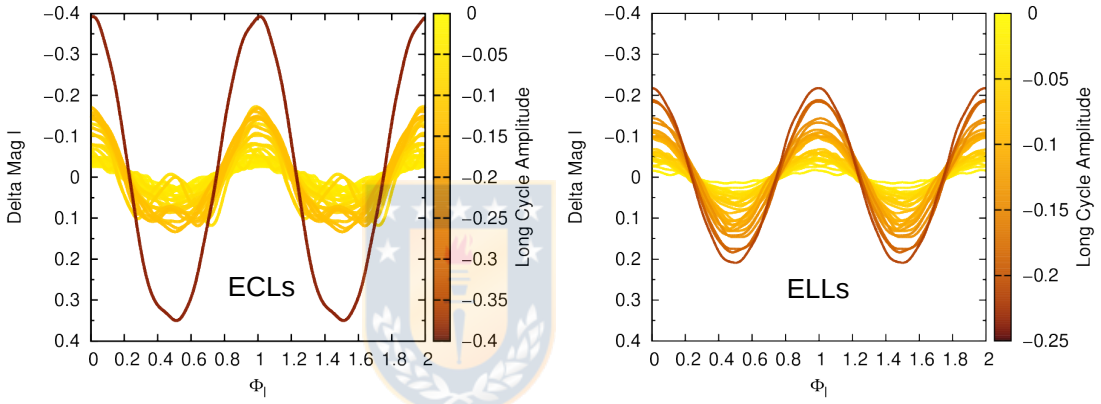

Figure A.3 Mathematical fit to the long cycle of some ELLs and ECLs DPVs, using Eq. 2.6. We note that both groups show a similar distribution of long-cycle amplitudes, with the exception of OGLE-LMC-DPV-097, which has the greatest amplitude in the OGLE I-band compared to the rest of the DPVs of the OGLE catalog (Poleski et al., 2010). We also note that only Double-Hump curves are observed in ECL DPVs.

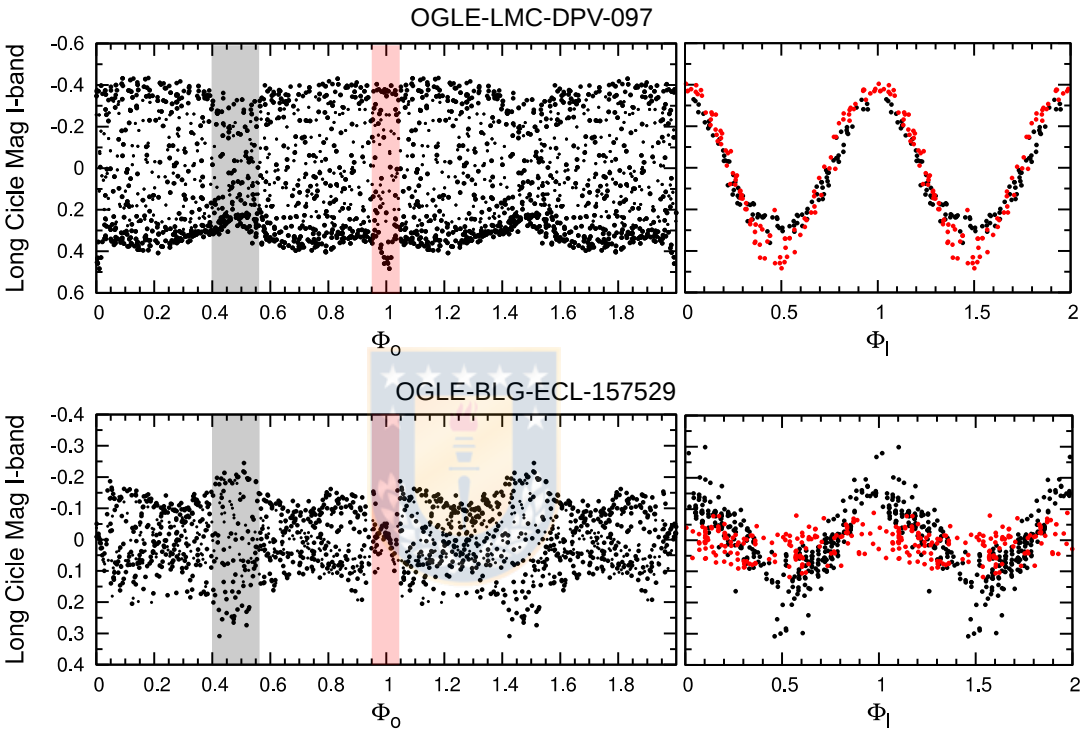

Figure A.4 Up: Top-Left: OGLE *I*-band magnitude for the long cycle of the DPV-097 vs the orbital phase (Φ_o). Top-right: OGLE *I*-band magnitude for the long cycle of the DPV-097 vs. the long cycle phase (Φ_l). The black dots correspond to the 0.4 to 0.55 orbital phase (obscured in gray in the left figure) and the red dots correspond to the orbital phase 0.95 to 1.05 (obscured in red in the left figure). Below, the same but for the OGLE-BLG-ECL-157529 system.

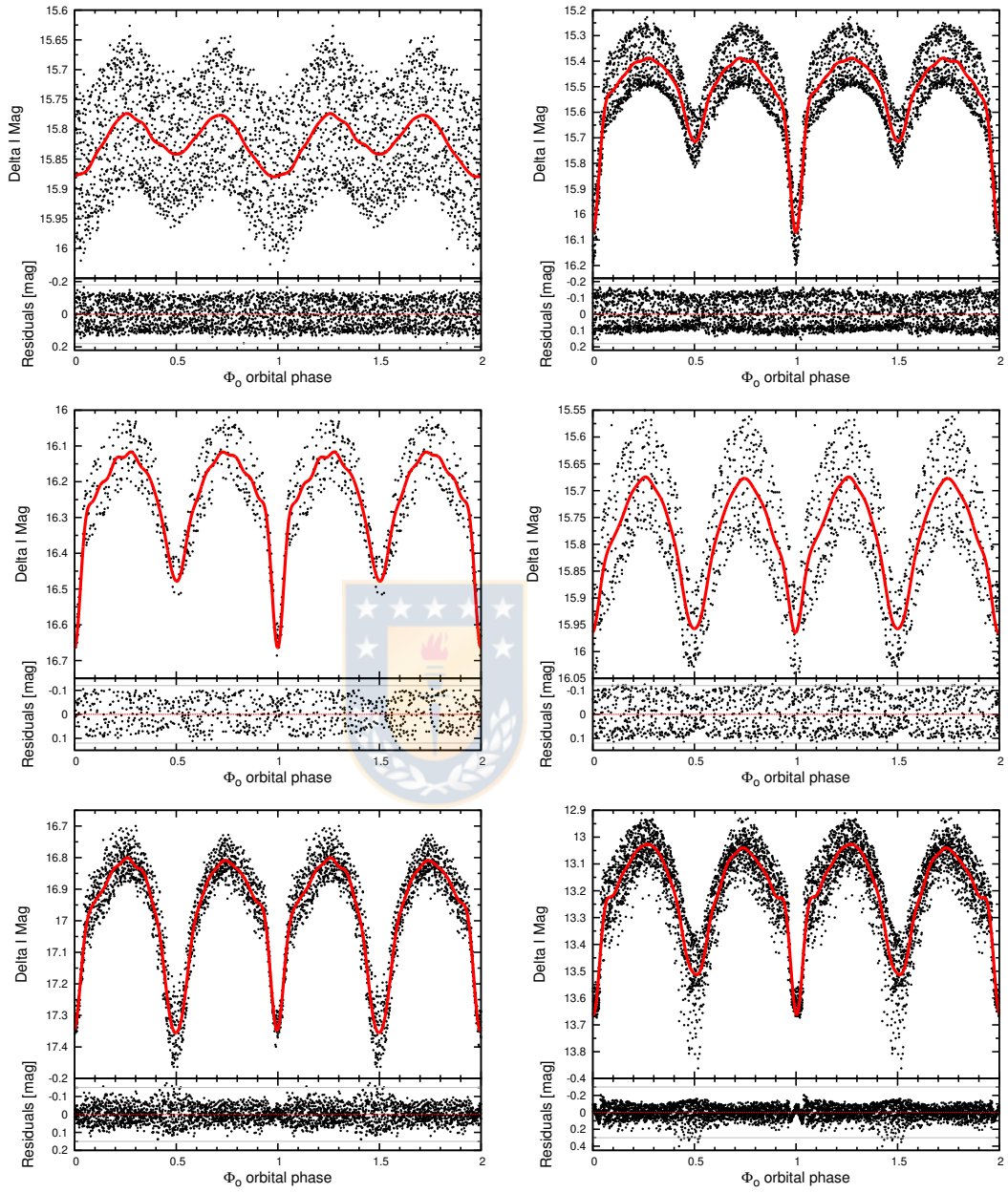

Figure A.5 Left: Light curve without disentangle. Red line corresponds to a fit by fourier series. Below are the residuals according to the orbital phase. OGLE-LMC-DPV-033, OGLE-LMC-DPV-006, OGLE-LMC-DPV-074, From top to bottom respectively. Right: The same but OGLE-LMC-DPV-056, OGLE-LMC-DPV-014, OGLE-BLG-ECL-157529, From top to bottom respectively. In the DPV-033 binary (ELL) we do not observe a decrease in the amplitude of the long cycle.

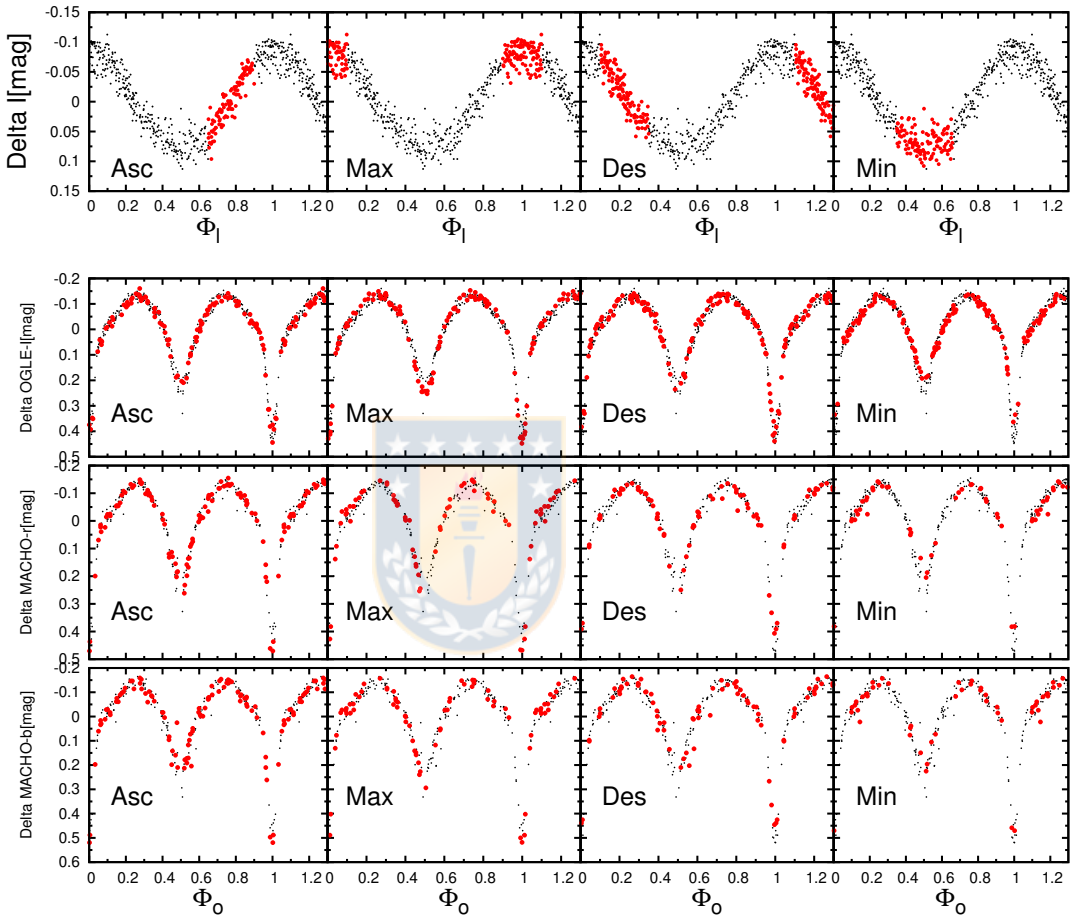

Figure A.6 Light curves of OGLE-LMC-DPV-006. Up: Long cycle light curve. The red dots indicate the stages of the long cycle (Asc, Max, Des, Min). Down. Orbital light curve. The red dots correspond to the same observation periods as those of the long cycle shown in the upper panel. OGLE-III campaign, MACHO-r and MACHO-b, from up to bottom, respectively.

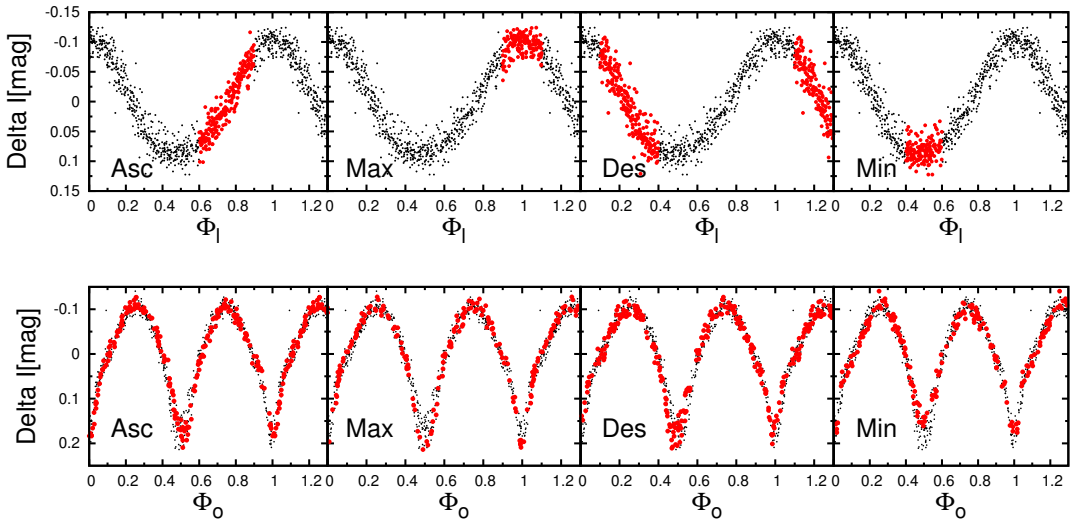

Figure A.7 Light curves of OGLE-LMC-DPV-014. Up: Long cycle light curve. The red dots indicate the stages of the long cycle (Asc, Max, Des, Min). Down. Orbital light curve. The red dots correspond to the same observation periods as those of the long cycle shown in the upper panel. Data from OGLE-II-III-IV campaign.

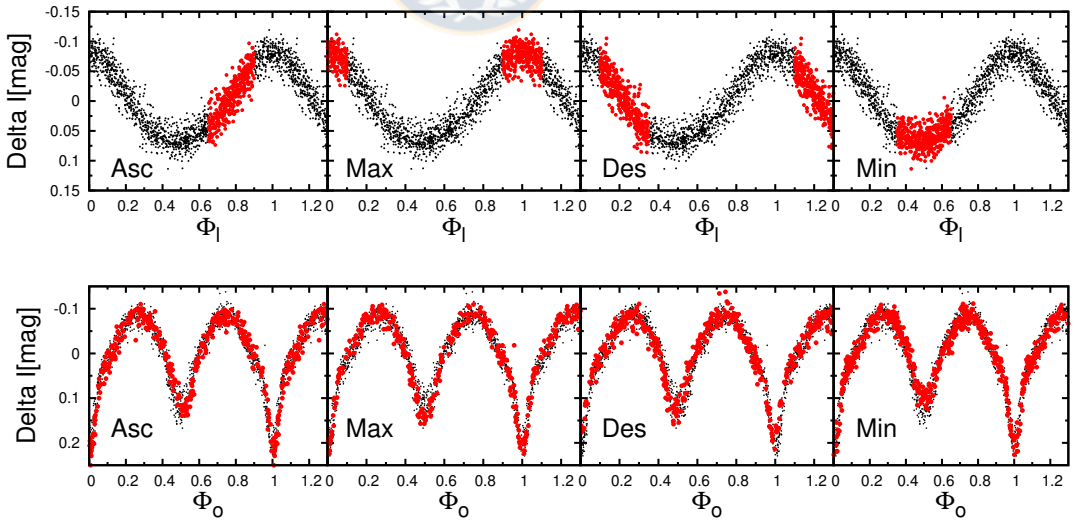

Figure A.8 Up: Light curves of OGLE-LMC-DPV-026. Up: Long cycle light curve. The red dots indicate the stages of the long cycle (Asc, Max, Des, Min). Down. Orbital light curve. The red dots correspond to the same observation periods as those of the long cycle shown in the upper panel. Data from OGLE-II-III-IV campaign.

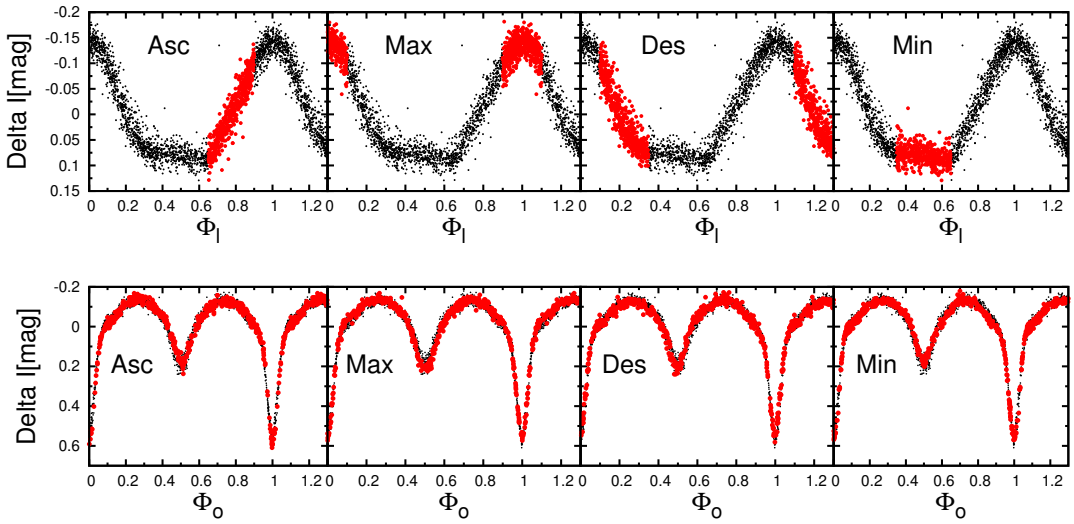

Figure A.9 Light curves of OGLE-LMC-DPV-056. Up: Long cycle light curve. The red dots indicate the stages of the long cycle (Asc, Max, Des, Min). Down. Orbital light curve. The red dots correspond to the same observation periods as those of the long cycle shown in the upper panel. Data from OGLE-II-III-IV campaign.

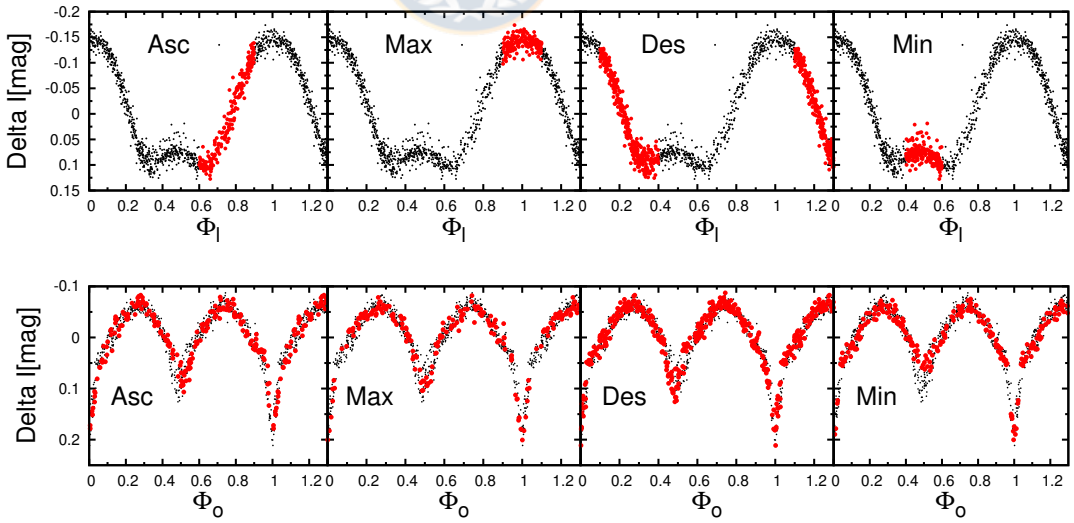

Figure A.10 Light curves of OGLE-LMC-DPV-058. Up: Long cycle light curve. The red dots indicate the stages of the long cycle (Asc, Max, Des, Min). Down. Orbital light curve. The red dots correspond to the same observation periods as those of the long cycle shown in the upper panel. Data from OGLE-II-III-IV campaign.

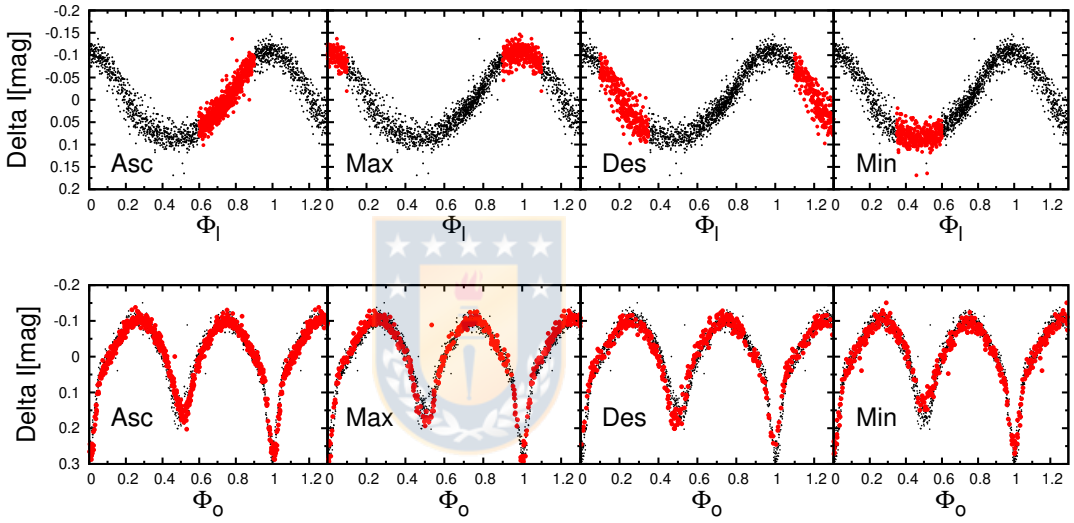

Figure A.11 Light curves of OGLE-LMC-DPV-062. Up: Long cycle light curve. The red dots indicate the stages of the long cycle (Asc, Max, Des, Min). Down. Orbital light curve. The red dots correspond to the same observation periods as those of the long cycle shown in the upper panel. Data from OGLE-II-III-IV campaign.

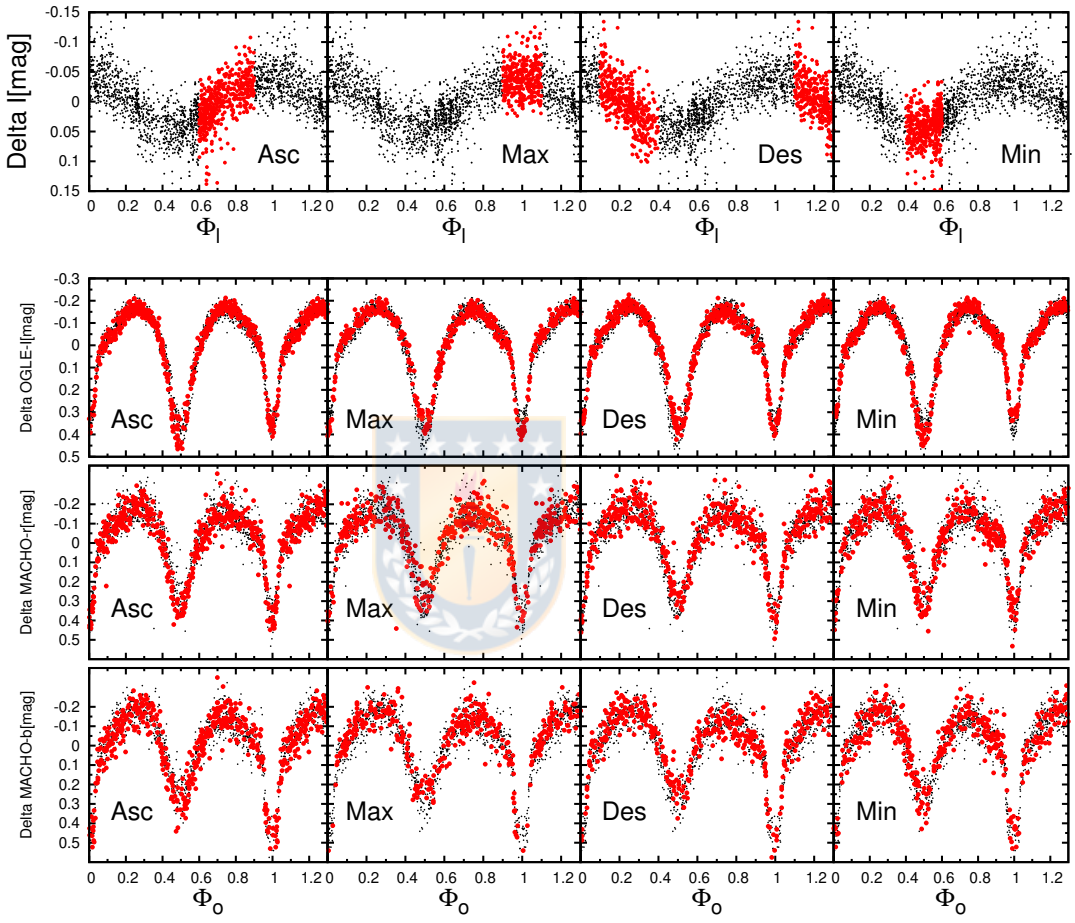

Figure A.12 Light curves of OGLE-LMC-DPV-074. Up: Long cycle light curve. The red dots indicate the stages of the long cycle (Asc, Max, Des, Min). Down. Orbital light curve. The red dots correspond to the same observation periods as those of the long cycle shown in the upper panel. OGLE-III campaign, MACHO-r and MACHO-b, from up to bottom, respectively.

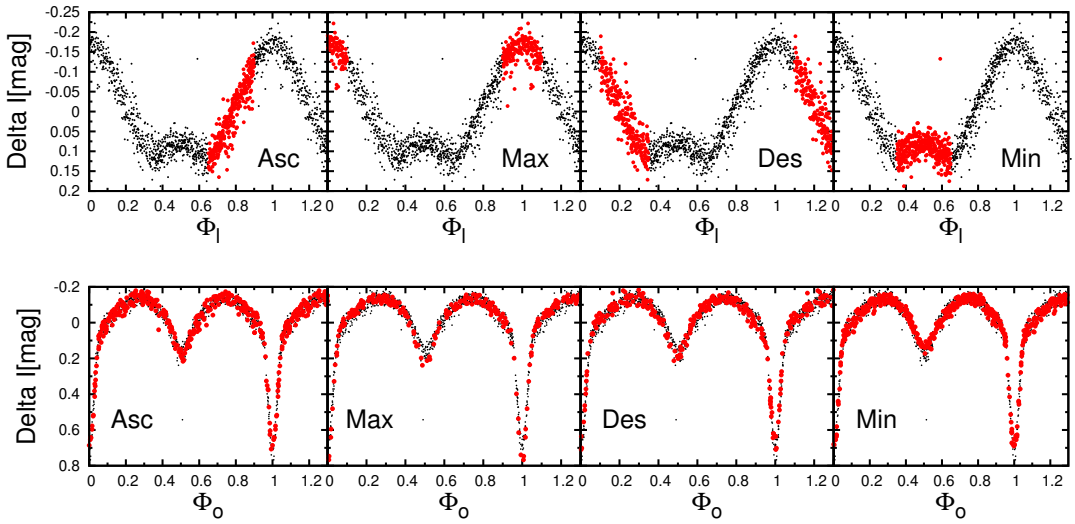

Figure A.13 Light curves of OGLE-LMC-DPV-121. Up: Long cycle light curve. The red dots indicate the stages of the long cycle (Asc, Max, Des, Min). Down. Orbital light curve. The red dots correspond to the same observation periods as those of the long cycle shown in the upper panel. Data from OGLE-II-III-IV campaign.

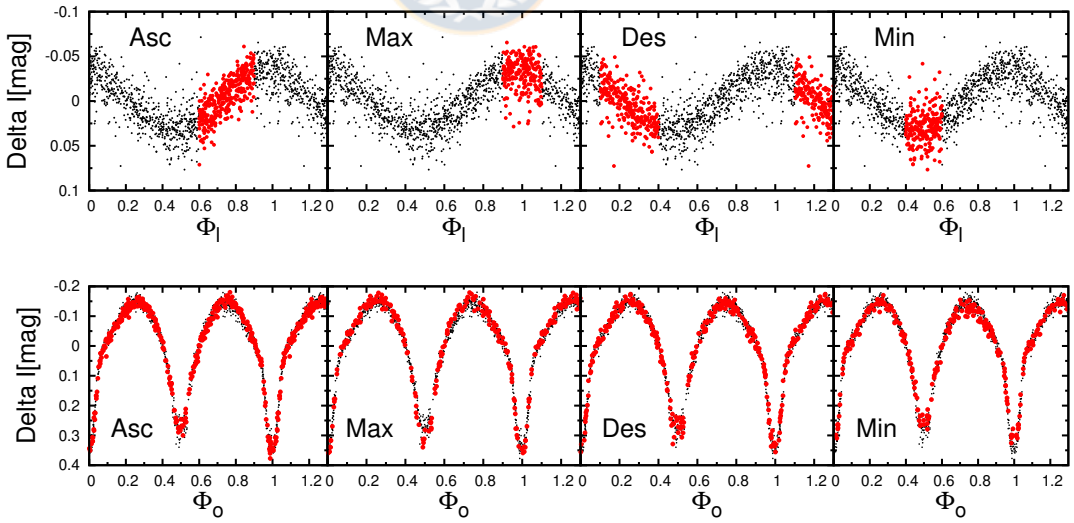

Figure A.14 Light curves of OGLE-SMC-ECL-5637. Up: Long cycle light curve. The red dots indicate the stages of the long cycle (Asc, Max, Des, Min). Down. Orbital light curve. The red dots correspond to the same observation periods as those of the long cycle shown in the upper panel. Data from OGLE-II-III-IV campaign.

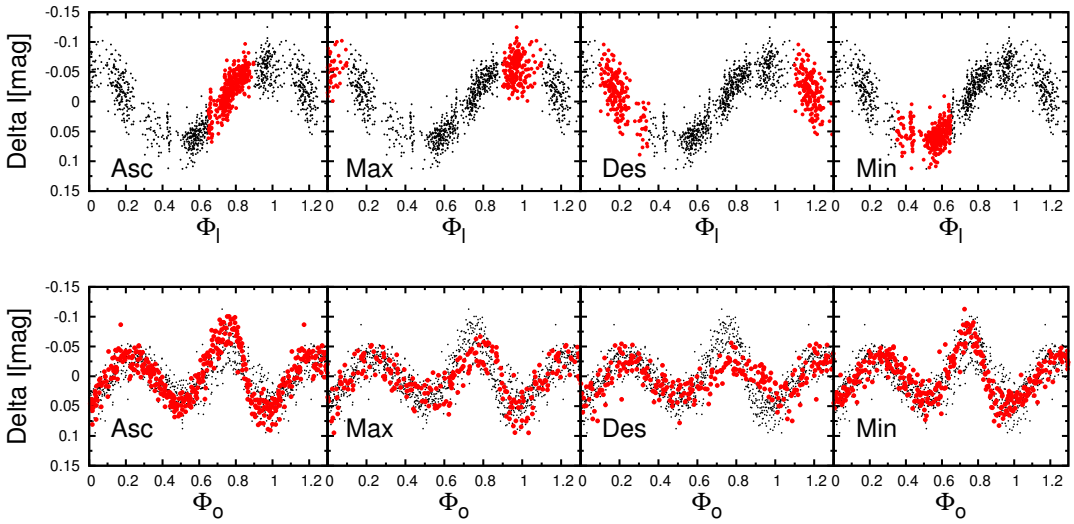

Figure A.15 Light curves of OGLE-LMC-DPV-022 (ELL). Up: Long cycle light curve. The red dots indicate the stages of the long cycle (Asc, Max, Des, Min). Down. Orbital light curve. The red dots correspond to the same observation periods as those of the long cycle shown in the upper panel. Data from OGLE-II-III-IV campaign.

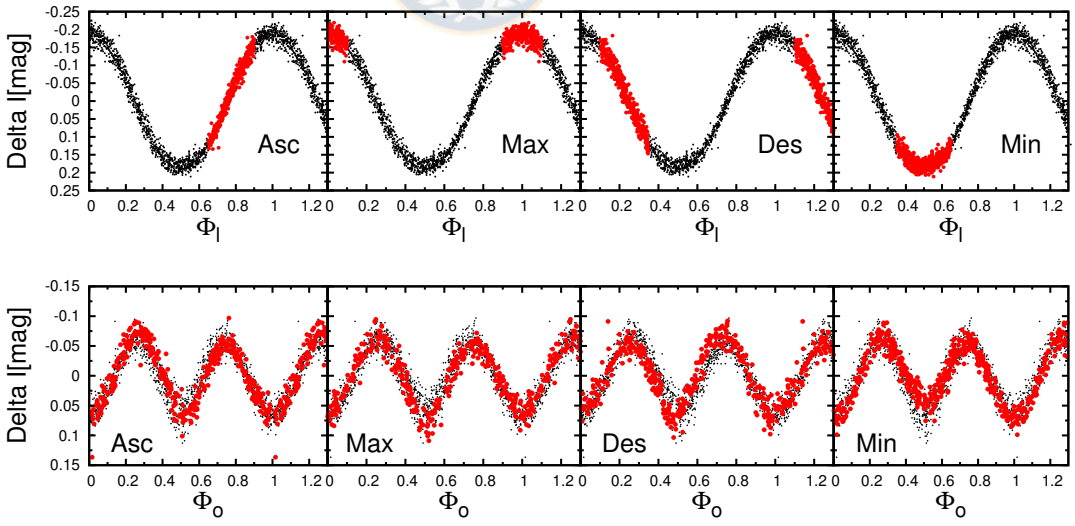

Figure A.16 Light curves of OGLE-LMC-DPV-035 (ELL). Up: Long cycle light curve. The red dots indicate the stages of the long cycle (Asc, Max, Des, Min). Down. Orbital light curve. The red dots correspond to the same observation periods as those of the long cycle shown in the upper panel. Data from OGLE-II-III-IV campaign.

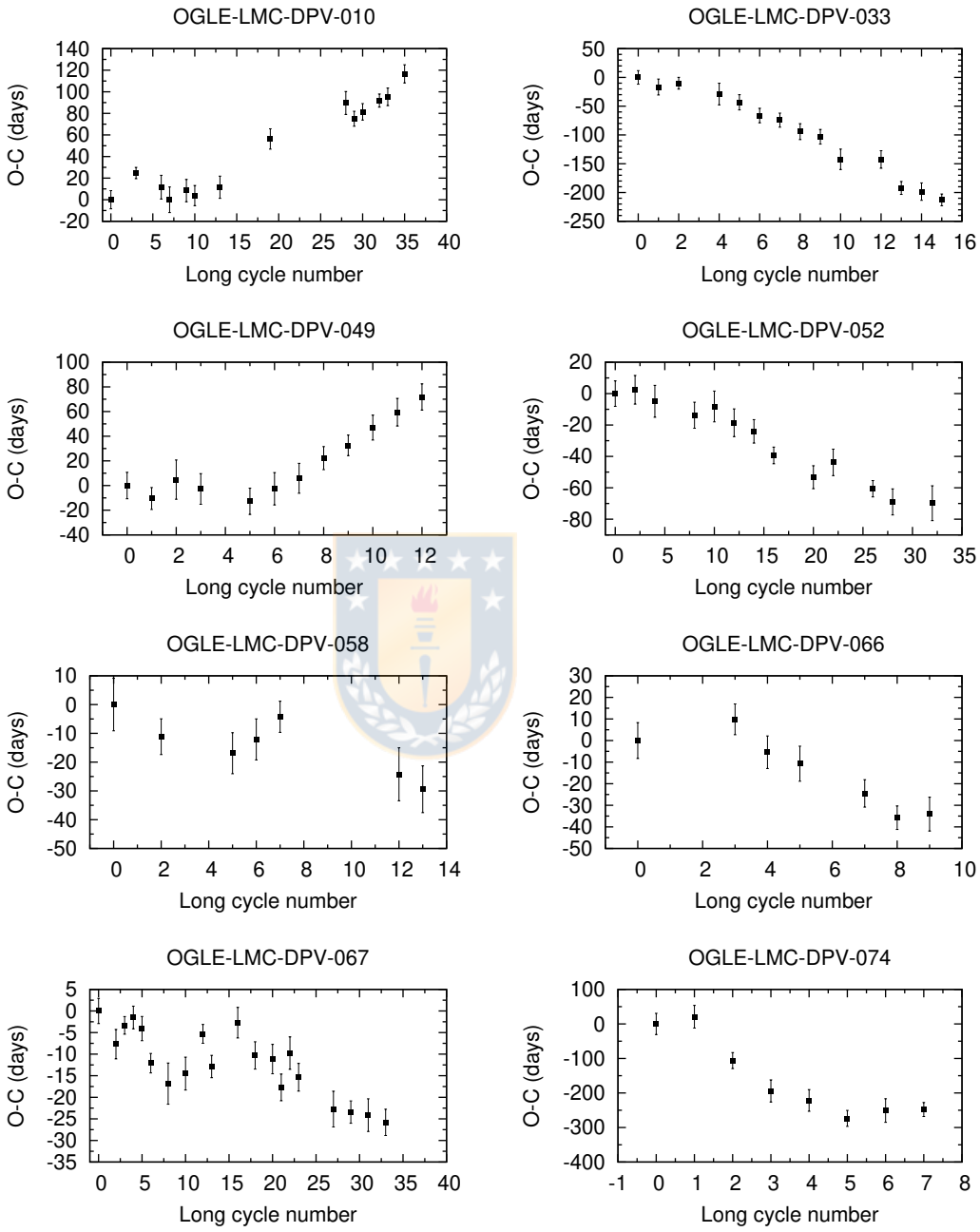

Figure A.17 Observed minus calculated epochs of the long cycle maximum versus long cycle number.

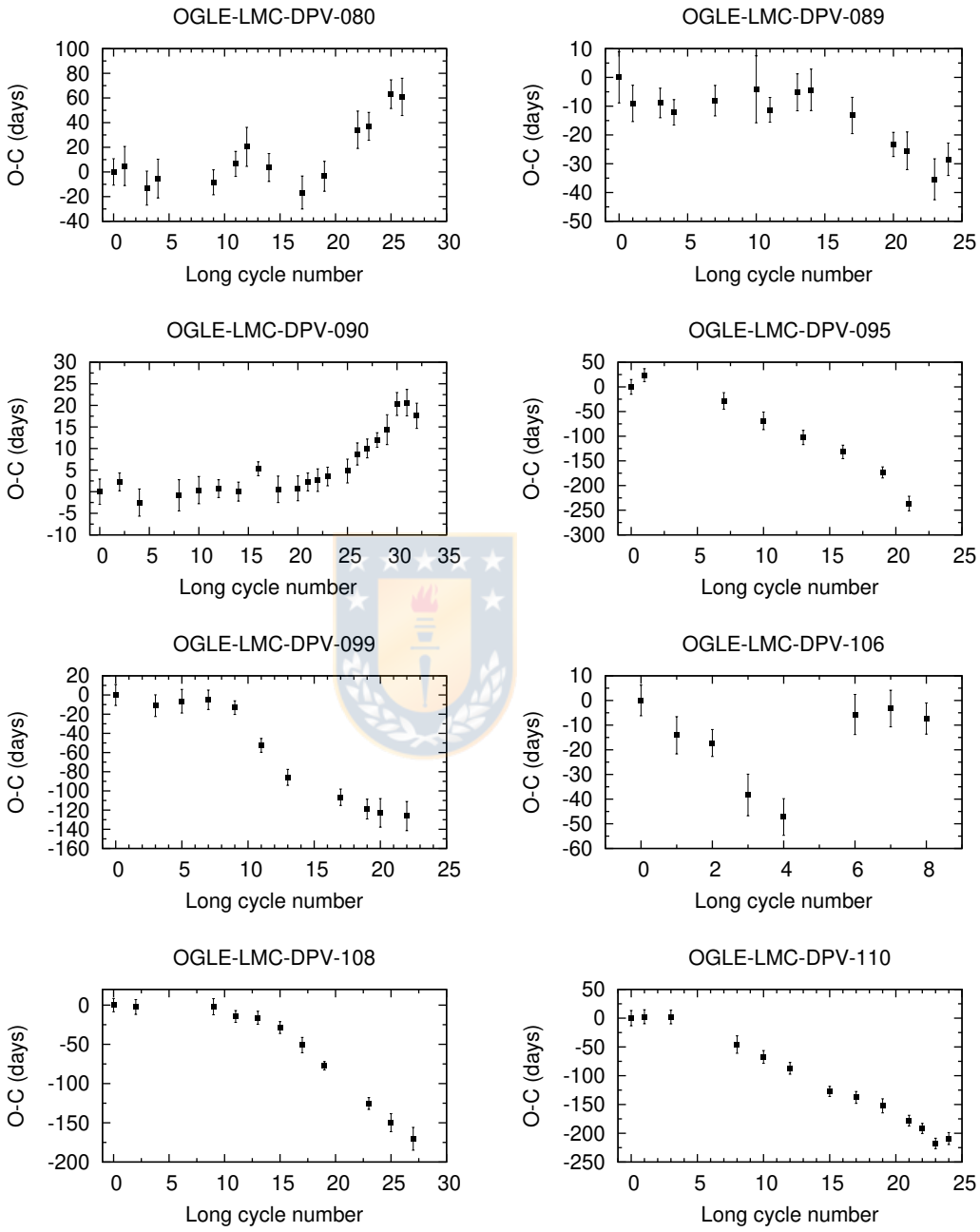

Figure A.18 Observed minus calculated epochs of the long cycle maximum versus long cycle number.

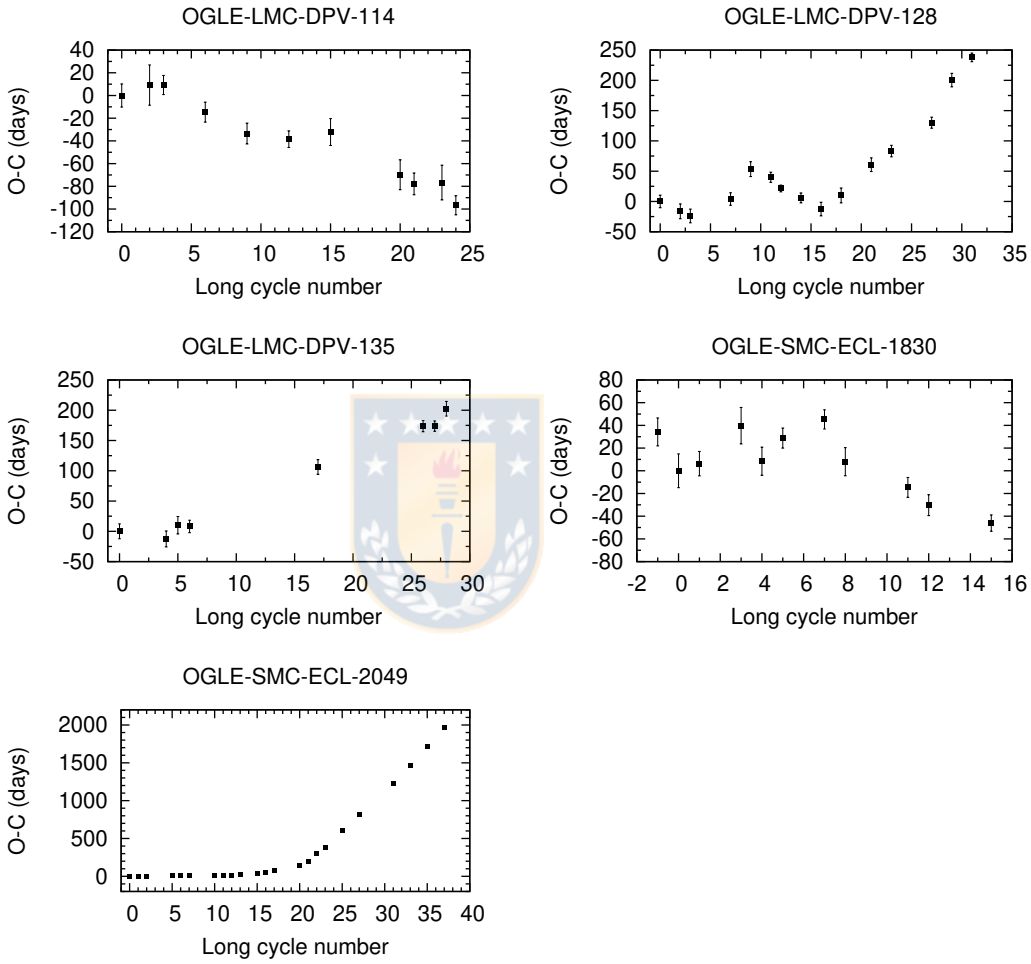

Figure A.19 Observed minus calculated epochs of the long cycle maximum versus long cycle number.

B

Additional tables

B.1 Complementary tables chapter 6

Table B.1 Summary of photometric observations of DPVs with changes in orbital light curves related to the long cycle. The number of measurements, starting and ending times, and average magnitude are given. HJD zero-point is 2400000.

Object	Data Base	N	HJD_{star}	HJD_{end}	Mag	Band
OGLE-LMC-DPV-006	OGLE-III	446	52171.9007	54951.4940	16.111	I
	MACHO	250	48927.7411	51541.5396	—	R
	MACHO	254	48927.7411	51541.5396	—	B
OGLE-LMC-DPV-014	OGLE-III	446	52166.81545	56721.61691	15.678	I
OGLE-LMC-DPV-026	OGLE-III	758	50726.80861	54954.46984	15.678	I
	OGLE-IV	703	55260.62701	56736.61145	15.678	I
OGLE-LMC-DPV-056	OGLE-II	394	50457.64919	51873.81250	15.374	I
	OGLE-III	973	52115.93631	54953.51680	15.374	I
	OGLE-IV	631	55260.61208	56736.61575	15.374	I
OGLE-LMC-DPV-058	OGLE-II	395	50457.64810	51873.81141	15.374	I
	OGLE-III	499	52123.93450	54953.52682	15.374	I
OGLE-LMC-DPV-062	OGLE-II	498	50455.68268	51873.76603	15.823	I
	OGLE-III	487	52115.93631	54953.51680	15.823	I
	OGLE-IV	630	5260.61208	6736.61575	15.830	I
OGLE-LMC-DPV-074	OGLE-II	496	50446.72314	51873.78102	16.817	I
	OGLE-III	543	52167.86807	54955.51356	16.817	I
	OGLE-IV	631	55260.61208	56736.61575	16.817	I
	MACHO	1510	48825.63430	51541.49770	16.817	R
	MACHO	1315	48825.63430	51541.49770	16.817	B
OGLE-LMC-DPV-121	OGLE-III	435	52187.79538	54947.53151	16.819	I
	OGLE-IV	649	5261.66360	6772.47204	16.853	I
OGLE-SMC-ECL-5637	OGLE-III	435	52104.89882	54873.55943	15.790	I
	OGLE-IV	407	5346.93180	6689.52706	15.790	I
OGLE-LMC-DPV-022	OGLE-III	458	52166.84886	54947.50748	16.396	I
	OGLE-IV	572	5261.55978	6736.60505	16.492	I
OGLE-LMC-DPV-035	OGLE-II	286	50726.80077	51874.76855	15.380	I
	OGLE-III	443	52166.84886	54954.46621	15.380	I
	OGLE-IV	706	5261.55978	6736.61145	15.343	I

Table B.2 Summary of all ECL DPVs in LMC considered in our analysis. The amplitude of the long cycle, primary minimum depth of the orbital cycle , reduced χ^2 and type of DPVs are given. The latter is made according to our criteria. Changes in the depth of the primary minimum related to the long cycle are not considered.

Objects	Long cycle aplitude [Mag]	Primary minimum depth [Mag]	Reduced χ^2	Type
OGLE-LMC-DPV-005	0.0588 ± 0.0012	0.491 ± 0.026	0.000621	ECL
OGLE-LMC-DPV-006	0.0797 ± 0.0009	0.543 ± 0.017	0.000337	ECL
OGLE-LMC-DPV-014	0.0953 ± 0.0006	0.290 ± 0.016	0.000317	ECL
OGLE-LMC-DPV-018	0.0468 ± 0.0016	0.815 ± 0.047	0.002406	ECL
OGLE-LMC-DPV-021	0.1328 ± 0.0010	0.369 ± 0.022	0.000471	ECL
OGLE-LMC-DPV-024	0.0369 ± 0.0009	0.354 ± 0.030	0.000891	ECL
OGLE-LMC-DPV-026	0.0728 ± 0.0005	0.291 ± 0.022	0.000302	ECL
OGLE-LMC-DPV-030	0.0479 ± 0.0009	0.336 ± 0.022	0.000606	ECL
OGLE-LMC-DPV-032	0.1151 ± 0.0008	0.514 ± 0.027	0.000852	ECL
OGLE-LMC-DPV-034	0.0539 ± 0.0008	0.634 ± 0.030	0.000951	ECL
OGLE-LMC-DPV-040	0.0298 ± 0.0008	0.301 ± 0.017	0.000288	ECL
OGLE-LMC-DPV-049	0.1952 ± 0.0018	0.834 ± 0.029	0.000890	ECL-DH
OGLE-LMC-DPV-051	0.1366 ± 0.0008	0.422 ± 0.032	0.001039	ECL
OGLE-LMC-DPV-053	0.0313 ± 0.0009	0.600 ± 0.024	0.000612	ECL
OGLE-LMC-DPV-056	0.1110 ± 0.0004	0.684 ± 0.019	0.000374	ECL-DH
OGLE-LMC-DPV-058	0.1246 ± 0.0005	0.239 ± 0.018	0.000212	ECL-DH
OGLE-LMC-DPV-060	0.0292 ± 0.0004	0.240 ± 0.015	0.000241	ECL
OGLE-LMC-DPV-061	0.0244 ± 0.0008	0.407 ± 0.019	0.000698	ECL
OGLE-LMC-DPV-062	0.0952 ± 0.0005	0.361 ± 0.020	0.000305	ECL
OGLE-LMC-DPV-063	0.0576 ± 0.0014	0.642 ± 0.043	0.001789	ECL
OGLE-LMC-DPV-065	0.0924 ± 0.0008	1.141 ± 0.027	0.000759	ECL-DH
OGLE-LMC-DPV-070	0.0527 ± 0.0008	0.201 ± 0.036	0.001250	ECL
OGLE-LMC-DPV-073	0.0701 ± 0.0014	0.716 ± 0.042	0.001842	ECL
OGLE-LMC-DPV-074	0.0443 ± 0.0007	0.540 ± 0.030	0.000829	ECL
OGLE-LMC-DPV-091	0.0281 ± 0.0009	0.142 ± 0.029	0.000829	ECL
OGLE-LMC-DPV-097	0.3780 ± 0.0013	0.218 ± 0.038	0.001476	ECL
OGLE-LMC-DPV-098	0.0915 ± 0.0006	0.211 ± 0.023	0.000510	ECL
OGLE-LMC-DPV-101	0.0528 ± 0.0007	1.085 ± 0.030	0.000900	ECL
OGLE-LMC-DPV-106	0.1878 ± 0.0007	0.176 ± 0.020	0.000475	ECL
OGLE-LMC-DPV-108	0.0877 ± 0.0005	0.203 ± 0.018	0.000351	ECL
OGLE-LMC-DPV-109	0.0612 ± 0.0008	0.628 ± 0.023	0.000535	ECL-DH
OGLE-LMC-DPV-112	0.0675 ± 0.0011	1.247 ± 0.030	0.000913	ECL-DH
OGLE-LMC-DPV-121	0.1334 ± 0.0009	0.827 ± 0.028	0.000801	ECL-DH
OGLE-LMC-DPV-124	0.0336 ± 0.0009	0.400 ± 0.027	0.000711	ECL
OGLE-LMC-DPV-129	0.0154 ± 0.0006	0.912 ± 0.024	0.000488	ECL
OGLE-LMC-DPV-131	0.0112 ± 0.0006	0.652 ± 0.026	0.000657	ECL
OGLE-LMC-DPV-134	0.0330 ± 0.0006	0.575 ± 0.023	0.000597	ECL
OGLE-LMC-DPV-137	0.0139 ± 0.0005	0.414 ± 0.021	0.000438	ECL

Table B.3 Summary of all ECL DPVs in SMC considered in our analysis. The amplitude of the long cycle, primary minimum depth of the orbital cycle , reduced χ^2 and type of DPVs are given. The latter is made according to our criteria. Changes in the depth of the primary minimum related to the long cycle are not considered.

Objects	Long cycle aplitude [Mag]	Primary minimum depth [Mag]	Reduced χ^2	Type
OGLE-SMC-ECL-1003	0.0345 ± 0.0016	0.490 ± 0.051	0.002542	ECL
OGLE-SMC-ECL-1005	0.0324 ± 0.0014	0.669 ± 0.047	0.002267	ECL
OGLE-SMC-ECL-1028	0.0264 ± 0.0009	0.553 ± 0.026	0.000679	ECL
OGLE-SMC-ECL-1144	0.0312 ± 0.0008	0.320 ± 0.025	0.000662	ECL
OGLE-SMC-ECL-1402	0.0415 ± 0.0010	0.876 ± 0.031	0.001048	ECL
OGLE-SMC-ECL-1799	0.0377 ± 0.0011	0.459 ± 0.036	0.002210	ECL
OGLE-SMC-ECL-1807	0.0639 ± 0.0010	0.491 ± 0.032	0.001049	ECL
OGLE-SMC-ECL-1830	0.1319 ± 0.0010	0.703 ± 0.032	0.001244	ECL-DH
OGLE-SMC-ECL-1983	0.0219 ± 0.0009	0.792 ± 0.031	0.000913	ECL
OGLE-SMC-ECL-2090	0.0499 ± 0.0012	0.351 ± 0.041	0.001660	ECL
OGLE-SMC-ECL-2331	0.0539 ± 0.0011	1.047 ± 0.038	0.001376	ECL-DH
OGLE-SMC-ECL-2597	0.0189 ± 0.0004	0.279 ± 0.012	0.000147	ECL
OGLE-SMC-ECL-3248	0.0220 ± 0.0009	0.350 ± 0.033	0.001097	ECL
OGLE-SMC-ECL-3604	0.0369 ± 0.0007	0.657 ± 0.022	0.000608	ECL
OGLE-SMC-ECL-4181	0.0285 ± 0.0008	0.845 ± 0.028	0.000948	ECL-DH
OGLE-SMC-ECL-4756	0.0237 ± 0.0005	0.133 ± 0.018	0.000315	ECL
OGLE-SMC-ECL-4933	0.0260 ± 0.0011	1.004 ± 0.035	0.001271	ECL-DH
OGLE-SMC-ECL-5046	0.0438 ± 0.0013	0.599 ± 0.037	0.001371	ECL
OGLE-SMC-ECL-5062	0.0468 ± 0.0010	0.693 ± 0.033	0.001032	ECL
OGLE-SMC-ECL-5637	0.0313 ± 0.0005	0.500 ± 0.016	0.000266	ECL

Table B.4 Summary of all ELL DPVs in LMC considered in our analysis. The amplitude of the long cycle, primary minimum depth of the orbital cycle , reduced χ^2 and type of DPVs are given. The latter is made according to our criteria.

Objects	Long cycle aplitude [Mag]	Primary minimum depth [Mag]	Reduced χ^2	Type
OGLE-LMC-DPV-001	0.2571 ± 0.0032	0.228 ± 0.038	0.001591	ELL
OGLE-LMC-DPV-002	0.0973 ± 0.0010	0.089 ± 0.021	0.000417	ELL
OGLE-LMC-DPV-003	0.0292 ± 0.0010	0.044 ± 0.020	0.000377	ELL
OGLE-LMC-DPV-004	0.0924 ± 0.0005	0.088 ± 0.015	0.000244	ELL
OGLE-LMC-DPV-007	0.0834 ± 0.0008	0.093 ± 0.020	0.000449	ELL
OGLE-LMC-DPV-009	0.0448 ± 0.0008	0.043 ± 0.023	0.000508	ELL
OGLE-LMC-DPV-010	0.0385 ± 0.0006	0.098 ± 0.015	0.000403	ELL
OGLE-LMC-DPV-011	0.0494 ± 0.0007	0.072 ± 0.021	0.000401	ELL
OGLE-LMC-DPV-013	0.0582 ± 0.0006	0.054 ± 0.019	0.000380	ELL
OGLE-LMC-DPV-015	0.0678 ± 0.0005	0.064 ± 0.012	0.000149	ELL
OGLE-LMC-DPV-016	0.0587 ± 0.0005	0.050 ± 0.016	0.000260	ELL
OGLE-LMC-DPV-017	0.0514 ± 0.0012	0.095 ± 0.026	0.000600	ELL
OGLE-LMC-DPV-019	0.1241 ± 0.0004	0.079 ± 0.013	0.000205	ELL
OGLE-LMC-DPV-020	0.1049 ± 0.0005	0.041 ± 0.018	0.000368	ELL
OGLE-LMC-DPV-022	0.0630 ± 0.0009	0.109 ± 0.022	0.000205	ELL
OGLE-LMC-DPV-023	0.0286 ± 0.0007	0.068 ± 0.019	0.000370	ELL
OGLE-LMC-DPV-025	0.1844 ± 0.0004	0.102 ± 0.020	0.000400	ELL
OGLE-LMC-DPV-027	0.1127 ± 0.0005	0.090 ± 0.022	0.000187	ELL
OGLE-LMC-DPV-028	0.0068 ± 0.0002	0.024 ± 0.006	0.000032	ELL
OGLE-LMC-DPV-029	0.0443 ± 0.0003	0.045 ± 0.010	0.000128	ELL
OGLE-LMC-DPV-031	0.1465 ± 0.0005	0.054 ± 0.016	0.000241	ELL
OGLE-LMC-DPV-033	0.1189 ± 0.0004	0.101 ± 0.013	0.000179	ELL
OGLE-LMC-DPV-035	0.1896 ± 0.0004	0.128 ± 0.016	0.000247	ELL
OGLE-LMC-DPV-038	0.1026 ± 0.0004	0.064 ± 0.022	0.000211	ELL
OGLE-LMC-DPV-039	0.0418 ± 0.0003	0.072 ± 0.011	0.000134	ELL
OGLE-LMC-DPV-041	0.0142 ± 0.0004	0.079 ± 0.014	0.000193	ELL
OGLE-LMC-DPV-042	0.0080 ± 0.0003	0.020 ± 0.009	0.000092	ELL
OGLE-LMC-DPV-043	0.0262 ± 0.0003	0.039 ± 0.011	0.000109	ELL
OGLE-LMC-DPV-044	0.0347 ± 0.0003	0.071 ± 0.010	0.000105	ELL
OGLE-LMC-DPV-045	0.0597 ± 0.0007	0.049 ± 0.018	0.000320	ELL
OGLE-LMC-DPV-047	0.0263 ± 0.0003	0.027 ± 0.010	0.000093	ELL
OGLE-LMC-DPV-048	0.1029 ± 0.0003	0.033 ± 0.011	0.000115	ELL
OGLE-LMC-DPV-050	0.0230 ± 0.0003	0.033 ± 0.013	0.000167	ELL
OGLE-LMC-DPV-052	0.1453 ± 0.0006	0.090 ± 0.027	0.000531	ELL
OGLE-LMC-DPV-055	0.0385 ± 0.0004	0.029 ± 0.011	0.000115	ELL
OGLE-LMC-DPV-057	0.0699 ± 0.0008	0.060 ± 0.025	0.000624	ELL
OGLE-LMC-DPV-059	0.0344 ± 0.0009	0.047 ± 0.030	0.000866	ELL
OGLE-LMC-DPV-064	0.0496 ± 0.0004	0.080 ± 0.016	0.000261	ELL
OGLE-LMC-DPV-066	0.2150 ± 0.0006	0.112 ± 0.015	0.000275	ELL
OGLE-LMC-DPV-067	0.0526 ± 0.0003	0.038 ± 0.015	0.000180	ELL
OGLE-LMC-DPV-068	0.0192 ± 0.0005	0.056 ± 0.022	0.000472	ELL
OGLE-LMC-DPV-069	0.0640 ± 0.0007	0.055 ± 0.043	0.000169	ELL

Table B.5 Continued

Objects	Long cycle aplitude [Mag]	Primary minimum depth [Mag]	Reduced χ^2	Type
OGLE-LMC-DPV-072	0.0157 ± 0.0007	0.030 ± 0.014	0.000181	ELL
OGLE-LMC-DPV-076	0.0197 ± 0.0002	0.007 ± 0.008	0.000061	ELL
OGLE-LMC-DPV-077	0.0438 ± 0.0005	0.053 ± 0.016	0.000254	ELL
OGLE-LMC-DPV-078	0.0727 ± 0.0005	0.069 ± 0.014	0.000204	ELL
OGLE-LMC-DPV-079	0.1623 ± 0.0009	0.086 ± 0.021	0.000445	ELL
OGLE-LMC-DPV-080	0.0481 ± 0.0003	0.035 ± 0.013	0.000166	ELL
OGLE-LMC-DPV-081	0.2179 ± 0.0008	0.132 ± 0.024	0.000605	ELL
OGLE-LMC-DPV-082	0.0357 ± 0.0004	0.094 ± 0.015	0.000215	ELL
OGLE-LMC-DPV-083	0.0845 ± 0.0004	0.081 ± 0.014	0.000122	ELL
OGLE-LMC-DPV-084	0.0683 ± 0.0004	0.089 ± 0.015	0.000266	ELL
OGLE-LMC-DPV-086	0.0408 ± 0.0005	0.040 ± 0.012	0.000142	ELL
OGLE-LMC-DPV-087	0.0377 ± 0.0006	0.093 ± 0.020	0.000389	ELL
OGLE-LMC-DPV-088	0.0314 ± 0.0003	0.017 ± 0.011	0.000105	ELL
OGLE-LMC-DPV-089	0.1058 ± 0.0004	0.070 ± 0.014	0.000200	ELL
OGLE-LMC-DPV-090	0.1651 ± 0.0005	0.105 ± 0.023	0.000516	ELL
OGLE-LMC-DPV-092	0.0411 ± 0.0003	0.025 ± 0.013	0.000081	ELL
OGLE-LMC-DPV-093	0.0135 ± 0.0005	0.048 ± 0.018	0.000340	ELL
OGLE-LMC-DPV-094	0.0235 ± 0.0005	0.175 ± 0.014	0.000209	ELL
OGLE-LMC-DPV-095	0.0320 ± 0.0003	0.018 ± 0.012	0.000142	ELL
OGLE-LMC-DPV-099	0.0392 ± 0.0003	0.058 ± 0.012	0.000143	ELL
OGLE-LMC-DPV-100	0.0569 ± 0.0007	0.063 ± 0.028	0.000610	ELL
OGLE-LMC-DPV-102	0.0332 ± 0.0005	0.043 ± 0.020	0.000379	ELL
OGLE-LMC-DPV-104	0.1114 ± 0.0006	0.044 ± 0.021	0.000427	ELL
OGLE-LMC-DPV-105	0.0875 ± 0.0005	0.049 ± 0.019	0.000372	ELL
OGLE-LMC-DPV-107	0.0952 ± 0.0006	0.097 ± 0.020	0.000429	ELL
OGLE-LMC-DPV-110	0.0674 ± 0.0004	0.026 ± 0.015	0.000224	ELL
OGLE-LMC-DPV-111	0.0818 ± 0.0005	0.119 ± 0.016	0.000256	ELL
OGLE-LMC-DPV-113	0.1190 ± 0.0006	0.106 ± 0.020	0.000426	ELL
OGLE-LMC-DPV-114	0.1264 ± 0.0010	0.102 ± 0.033	0.001099	ELL
OGLE-LMC-DPV-115	0.2126 ± 0.0005	0.083 ± 0.015	0.000216	ELL
OGLE-LMC-DPV-116	0.0575 ± 0.0005	0.065 ± 0.014	0.000199	ELL
OGLE-LMC-DPV-117	0.0635 ± 0.0005	0.054 ± 0.018	0.000321	ELL
OGLE-LMC-DPV-118	0.0235 ± 0.0004	0.049 ± 0.012	0.000147	ELL
OGLE-LMC-DPV-119	0.1248 ± 0.0006	0.075 ± 0.023	0.000563	ELL
OGLE-LMC-DPV-120	0.0705 ± 0.0012	0.126 ± 0.037	0.001357	ELL
OGLE-LMC-DPV-122	0.0962 ± 0.0011	0.100 ± 0.025	0.000567	ELL
OGLE-LMC-DPV-123	0.1373 ± 0.0011	0.086 ± 0.030	0.000951	ELL
OGLE-LMC-DPV-125	0.0507 ± 0.0007	0.108 ± 0.015	0.000206	ELL
OGLE-LMC-DPV-128	0.0333 ± 0.0005	0.039 ± 0.018	0.000336	ELL
OGLE-LMC-DPV-130	0.0145 ± 0.0009	0.057 ± 0.024	0.000567	ELL
OGLE-LMC-DPV-132	0.0036 ± 0.0002	0.048 ± 0.006	0.000035	ELL
OGLE-LMC-DPV-135	0.0461 ± 0.0007	0.071 ± 0.027	0.000885	ELL

Bibliography

Alard, C., *A&AS*, 144:363–370, Jun 2000.

Alard, C. & Lupton, R. H., *ApJ*, 503(1):325–331, Aug 1998.

Alcock, C., Allsman, R. A., Alves, D., Axelrod, T. S., Becker, A. C., Bennett, D. P., Cook, K. H., Freeman, K. C., Griest, K., Lacy, C. H. S., Lehner, M. J., Marshall, S. L., Minniti, D., Peterson, B. A., Pratt, M. R., Quinn, P. J., Rodgers, A. W., Stubbs, C. W., Sutherland, W., & Welch, D. L., *AJ*, 114:326, Jul 1997.

Allsman, R. A., Axelrod, T. S., & for the Macho Collaboration, *arXiv e-prints*, art. astro-ph/0108444, Aug 2001.

Andersen, J., *A&A Rev.*, 3(2):91–126, Jan 1991.

Applegate, J. H., *ApJ*, 385:621–629, February 1992.

Atwood-Stone, C., Miller, B. P., Richards, M. T., Budaj, J., & Peters, G. J., *ApJ*, 760(2):134, Dec 2012.

Barning, F. J. M., *Bull. Astron. Inst. Netherlands*, 17:22, Aug 1963.

Barría, D., Mennickent, R. E., Graczyk, D., & Kołaczkowski, Z., *A&A*, 567:A140, Jul 2014.

Bath, G. T. & Pringle, J. E., *MNRAS*, 194:967–986, Mar 1981.

Bisikalo, D. V., Boyarchuk, A. A., Kuznetsov, O. V., & Chechyotkin, V. M., *Astronomy Reports*, 41(6):786–793, Nov 1997.

Bisikalo, D. V., Boyarchuk, A. A., Chechetkin, V. M., Kuznetsov, O. A., & Molteni, D., *MNRAS*, 300(1):39–48, Oct 1998.

Bisikalo, D. V., Harmanec, P., Boyarchuk, A. A., Kuznetsov, O. A., & Hadrava, P., *A&A*, 353: 1009–1015, Jan 2000.

Bressan, A., Marigo, P., Girardi, L., Salasnich, B., Dal Cero, C., Rubele, S., & Nanni, A., *MNRAS*, 427:127–145, November 2012.

Buchler, J. R., Wood, P. R., & Wilson, R. E., *ApJ*, 703(2):1565–1568, Oct 2009.

Cox, A. N. *Allen's astrophysical quantities*. 2000a.

Cox, A. N. *Allen's astrophysical quantities*. 2000b.

De Greve, J. P. & Linnell, A. P., *A&A*, 291:786–794, Nov 1994.

de Mink, S. E., Sana, H., Langer, N., Izzard, R. G., & Schneider, F. R. N., *ApJ*, 782(1):7, Feb 2014.

Derekas, A., Kiss, L. L., & Bedding, T. R., *ApJ*, 663(1):249–257, Jul 2007.

Desmet, M., Frémat, Y., Baudin, F., Harmanec, P., Lampens, P., Pacheco, E. J., Briquet, M., Degroote, P., Neiner, C., & Mathias, P., *MNRAS*, 401(1):418–432, Jan 2010.

Djurašević, G., *Ap&SS*, 196:267–282, October 1992a.

Djurašević, G., *Ap&SS*, 197:17–34, November 1992b.

Djurašević, G., Latković, O., Vince, I., & Cséki, A., *MNRAS*, 409:329–336, November 2010.

Djurašević, G., Vince, I., & Atanacković, O., *AJ*, 136(2):767–772, Aug 2008.

Djurašević, G., Vince, I., Antokhin, I. I., Shatsky, N. I., Cséki, A., Zakirov, M., & Eshankulova, M., *MNRAS*, 420(4):3081–3090, Mar 2012.

Eggleton, P. P., *ApJ*, 268:368–369, May 1983.

Flannery, B. P., *MNRAS*, 170:325–331, Feb 1975.

Frank, J., King, A. R., & Raine, D. J., *Astronomische Nachrichten*, 316(6):414, Sep 1995.

Gaia Collaboration et al., *A&A*, 595:A1, Nov 2016.

Gaia Collaboration et al., *A&A*, 616:A1, Aug 2018.

Garcés L., J., Mennickent, R. E., Djurašević, G., Poleski, R., & Soszyński, I., *MNRAS*, 477:L11–L15, June 2018.

Habing, H. J. & Olofsson, H. *Asymptotic Giant Branch Stars*. 2004.

Harmanec, P., Morand, F., Bonneau, D., Jiang, Y., Yang, S., Guinan, E. F., Hall, D. S., Mourard, D., Hadrava, P., Bozic, H., Sterken, C., Tallon-Bosc, I., Walker, G. A. H., McCook, G. P., Vakili, F., Stee, P., & Le Contel, J. M., *A&A*, 312:879–896, Aug 1996.

Harmanec, P., Bisikalo, D. V., Boyarchuk, A. A., & Kuznetsov, O. A., *A&A*, 396:937–948, Dec 2002.

Heemskerk, M. H. M., *A&A*, 288:807–818, Aug 1994.

Hessman, F. V. & Hopp, U., *A&A*, 228:387–398, Feb 1990.

Hilditch, R. W. *An Introduction to Close Binary Stars*. 2001.

Hoffman, J. L., Nordsieck, K. H., & Fox, G. K., *AJ*, 115(4):1576–1591, Apr 1998.

Huang, S.-S., *ApJ*, 138:342, Aug 1963.

Kim, D.-W., Protopapas, P., Bailer-Jones, C. A. L., Byun, Y.-I., Chang, S.-W., Marquette, J.-B., & Shin, M.-S., *A&A*, 566:A43, Jun 2014.

Kippenhahn, R. & Weigert, A., *Zeitschrift fur Astrophysik*, 65:251, Jan 1967.

Kononov, D. A., Bisikalo, D. V., Puzin, V. B., Zhilkin, A. G., & Sytov, A. Y., *Astronomy Reports*, 59(3):191–198, Mar 2015.

Lenz, P. & Breger, M., *Communications in Asteroseismology*, 146:53–136, June 2005.

Lomb, N. R., *Ap&SS*, 39(2):447–462, Feb 1976.

Lubow, S. H. & Shu, F. H., *ApJ*, 198:383–405, Jun 1975.

Marsh, T. R. & Horne, K., *MNRAS*, 299(3):921–928, Sep 1998.

Mennickent, R. E., *Serbian Astronomical Journal*, 194:1–21, June 2017.

Mennickent, R. E. & Djurašević, G., *MNRAS*, 432(1):799–809, Jun 2013.

Mennickent, R. E., Pietrzyński, G., Diaz, M., & Gieren, W., *A&A*, 399:L47–L50, March 2003.

Mennickent, R. E., Cidale, L., Díaz, M., Pietrzyński, G., Gieren, W., & Sabogal, B., *MNRAS*, 357 (4):1219–1230, Mar 2005.

Mennickent, R. E., Kołaczkowski, Z., Michalska, G., Pietrzyński, G., Gallardo, R., Cidale, L., Granada, A., & Gieren, W., *MNRAS*, 389(4):1605–1618, Oct 2008.

Mennickent, R. E., Djurašević, G., Kołaczkowski, Z., & Michalska, G., *MNRAS*, 421(1):862–871, Mar 2012a.

Mennickent, R. E., Kołaczkowski, Z., Djurasevic, G., Niemczura, E., Diaz, M., Curé, M., Araya, I., & Peters, G. J., *MNRAS*, 427(1):607–624, Nov 2012b.

Mennickent, R. E., Djurašević, G., Cabezas, M., Cséki, A., Rosales, J. G., Niemczura, E., Araya, I., & Curé, M., *MNRAS*, 448:1137–1152, April 2015.

Mennickent, R. E., Otero, S., & Kołaczkowski, Z., *MNRAS*, 455:1728–1745, January 2016.

Mennickent, R. E., Zharikov, S., Cabezas, M., & Djurašević, G., *MNRAS*, 461(2):1674–1683, Sep 2016b.

Mennickent, R. E., Schleicher, D. R. G., & San Martin-Perez, R., *PASP*, 130(9):094203, September 2018.

Mennickent, R. E., Cabezas, M., Djurašević, , G., Rivinius, T., Hadrava, P., Poleski, R., Soszyński, I., Celedón, L., & Astudillo-Defru, N., *MNRAS*, page 1290, May 2019.

Muraveva, T., Clementini, G., Maceroni, C., Evans, C. J., Moretti, M. I., Cioni, M. R. L., Marquette, J. B., Ripepi, V., de Grijs, R., Groenewegen, M. A. T., Piatti, A. E., & van Loon, J. T., *MNRAS*, 443(1):432–445, Sep 2014.

Navarrete, F. H., Schleicher, D. R. G., Zamponi Fuentealba, J., & Völschow, M., *A&A*, 615:A81, Jul 2018.

Nazarenko, V. V. & Glazunova, L. V., *Astronomy Reports*, 47(12):1013–1026, Dec 2003.

Nazarenko, V. V. & Glazunova, L. V., *Astronomy Reports*, 50(5):369–379, May 2006a.

Nazarenko, V. V. & Glazunova, L. V., *Astronomy Reports*, 50(5):380–386, May 2006b.

Paczynski, B., *ApJ*, 216:822–826, Sep 1977.

Pawlak, M., Graczyk, D., Soszyński, I., Pietrukowicz, P., Poleski, R., Udalski, A., Szymański, M. K., Kubiak, M., Pietrzyński, G., Wyrzykowski, Ł., Ulaczyk, K., Kozłowski, S., & Skowron, J., *Serbian Astronomical JournalActa Astron.*, 63:323–338, September 2013.

Pawlak, M., Soszyński, I., Udalski, A., Szymański, M. K., Wyrzykowski, Ł., Ulaczyk, K., Poleski, R., Pietrukowicz, P., Kozłowski, S., Skowron, D. M., Skowron, J., Mróz, P., & Hamanowicz, A., *Acta Astron.*, 66(4):421–432, Dec 2016.

Peters, G. J. *The Algol-Type Binaries*. In Vanbeveren, D., editor, *The Influence of Binaries on Stellar Population Studies*, volume 264 of *Astrophysics and Space Science Library*, page 79, Jan 2001. doi: 10.1007/978-94-015-9723-4_6.

Pietrzyński, G., Graczyk, D., Gieren, W., Thompson, I. B., Pilecki, B., Udalski, A., Soszyński, I., Kozłowski, S., Konorski, P., Suchomska, K., Bono, G., Moroni, P. G. P., Villanova, S., Nardetto, N., Bresolin, F., Kudritzki, R. P., Storm, J., Gallenne, A., Smolec, R., Minniti, D., Kubiak, M., Szymański, M. K., Poleski, R., Wyrzykowski, Ł., Ulaczyk, K., Pietrukowicz, P., Górski, M., & Karczmarek, P., *Nature*, 495(7439):76–79, Mar 2013.

Poleski, R., Soszyński, I., Udalski, A., Szymański, M. K., Kubiak, M., Pietrzyński, G., Wyrzykowski, Ł., & Ulaczyk, K., *Acta Astron.*, 60:179–196, September 2010.

Richards, M. T., *Astronomische Nachrichten*, 325(3):229–232, Mar 2004.

Richards, M. T., Cocking, A. S., Fisher, J. G., & Conover, M. J., *ApJ*, 795(2):160, Nov 2014.

Sana, H., de Mink, S. E., de Koter, A., Langer, N., Evans, C. J., Gieles, M., Gosset, E., Izzard, R. G., Le Bouquin, J. B., & Schneider, F. R. N., *Science*, 337(6093):444, Jul 2012.

Scargle, J. D., *ApJ*, 263:835–853, Dec 1982.

Schleicher, D. R. G. & Mennickent, R. E., *A&A*, 602:A109, June 2017.

Smak, J., *Acta Astron.*, 20:311, Jan 1970.

Soszynski, I., Udalski, A., Kubiak, M., Szymanski, M. K., Pietrzynski, G., Zebrun, K., Szewczyk, O., Wyrzykowski, L., & Dziembowski, W. A., *Acta Astron.*, 54:347–362, Dec 2004.

Soszyński, I., Pawlak, M., Pietrukowicz, P., Udalski, A., Szymański, M. K., Wyrzykowski, Ł., Ulaczyk, K., Poleski, R., Kozłowski, S., Skowron, D. M., Skowron, J., Mróz, P., & Hamanowicz, A., *Acta Astron.*, 66:405–420, December 2016.

Stellingwerf, R. F., *ApJ*, 224:953–960, Sep 1978.

Szymanski, M. K., *Acta Astron.*, 55:43–57, Mar 2005.

Tout, C. A. & Hall, D. S., *MNRAS*, 253:9–18, Nov 1991.

Udalski, A., *Acta Astron.*, 53:291–305, Dec 2003.

Udalski, A., Kubiak, M., & Szymanski, M., *Acta Astron.*, 47:319–344, Jul 1997.

Udalski, A., Szymański, M. K., & Szymański, G., *Acta Astron.*, 65:1–38, March 2015.

Van Rensbergen, W. & De Greve, J. P., *A&A*, 592:A151, Aug 2016.

van Rensbergen, W., De Greve, J. P., De Loore, C., & Mennekens, N., *A&A*, 487(3):1129–1138, Sep 2008.

van Rensbergen, W., de Greve, J. P., Mennekens, N., Jansen, K., & de Loore, C., *A&A*, 528:A16, Apr 2011.

Warner, B., *Cambridge Astrophysics Series*, 28, Jan 1995.

Wozniak, P. R., *Acta Astron.*, 50:421–450, Dec 2000.

Zasche, P., Wolf, M., Vraštil, J., Fatka, P., Galád, A., Hornoch, K., Janák, Z., Janík, J., Kortusová, E., Kurfürst, P., Kušnirák, P., Paunzen, E., Řezba, L., Votruba, V., Zejda, M., & Zieliński, P., *Acta Astron.*, 67:243–255, September 2017.

Zechmeister, M. & Kürster, M., *A&A*, 496(2):577–584, Mar 2009.

Zola, S., *Acta Astron.*, 41:213–230, 1991.

Zoła, S. & Ogłoza, W., *A&A*, 368:932–938, Mar 2001.